Development of a Kr magneto-optical trap for efficient loading and collision studies

By

Surendra Singh

PHYS03200804007

Raja Ramanna Centre for Advanced Technology

A thesis submitted to the

Board of Studies in Physical Sciences

In partial fulfillment of requirements

For the degree of

DOCTOR OF PHILOSOPHY

of

HOMI BHABHA NATIONAL INSTITUTE

February 2016

Homi Bhabha National Institute

Recommendations of the Viva-Voce Board

As members of the Viva Voce Board, we certify that we have read the dissertation prepared by **Surendra Singh** entitled **"Development of a Kr magneto-optical trap for efficient loading and collision studies"** and recommend that it may be accepted as fulfilling the dissertation requirement for the Degree of Doctor of Philosophy.

Chairman – Prof. S. B. Roy	Date:12-01-2017

Guide – Prof. H. S. Rawat	Date:12-01-2017

12/1/17
Member 1 – Prof. P. A. Naik	Date:12-01-2017

Member 2 – Prof. S. K. Dixit	Date:12-01-2017

External Examiner – Dr. Umakant D. Rapol	Date:12-01-2017

Final approval and acceptance of this dissertation is contingent upon the candidate's submission of the final copies of the dissertation to HBNI.

I hereby certify that I have read this dissertation prepared under my direction and recommend that it may be accepted as fulfilling the dissertation requirement.

Date:12-01-2017	Guide:

Place: RRCAT, Indore	(Prof. H. S. Rawat)

STATEMENT BY THE AUTHOR

This dissertation has been submitted in partial fulfillment of requirements for an advanced degree at Homi Bhabha National Institute (HBNI) and is deposited in the Library to be made available to borrowers under rules of the HBNI.

Brief quotations from this dissertation are allowable without special permission, provided that accurate acknowledgment of source is made. Requests for permission for extended quotation from or reproduction of this manuscript in whole or in part may be granted by the Competent Authority of HBNI when in his or her judgment the proposed use of the material is in the interest of scholarship. In all other instances, however, permission must be obtained from the author.

(Surendra Singh)

DECLARATION

I, hereby declare that the investigation presented in the thesis has been carried out by me. The work is original and has not been submitted earlier as a whole or in part for a degree / diploma at this or any other Institution / University.

(Surendra Singh)

List of publications arising from the thesis

A. **Publications in refereed Journals: (4)**

1. **S. Singh**, Vivek Singh, V. B. Tiwari, S. R. Mishra and H. S. Rawat, "Magnetic field assisted enhancement in number density of metastable Krypton (Kr*) atoms in a Krypton atomic beam", Indian Journal of Pure and Applied Physics **51**, 230 (2013).
2. **S. Singh**, V. B. Tiwari, S. R. Mishra and H. S. Rawat, "An atomic beam fluorescence locked magneto-optical trap for Krypton atoms", Laser physics **24**, 25501 (2014).
3. **S. Singh**, V. B. Tiwari, S. R. Mishra and H. S. Rawat, "Loading of a Krypton magneto-optical trap with two hollow laser beams in Zeeman slower", J. Exp. Theo. Phys. **119**, 406 (2014).
4. **S. Singh**, V. B. Tiwari, Y. B. Kale, S. R. Mishra and H. S. Rawat, "Investigation of cold collision in a two-isotope Krypton magneto-optical trap", J. Phys. B: At. Mol. Opt. Phys. **48**, 175302 (2015).

B. **Publications in National / International Conferences/ Symposia: (6)**

1. **S. Singh**, V. B. Tiwari and H. S. Rawat, "High resolution spectroscopy of metastable Kr atoms for laser frequency stabilization", Abstract book of DAE-BRNS National Laser Symposium, RRCAT, Indore, Dec. 1-4, (2010).
2. **S. Singh**, V. Singh, V. B. Tiwari, S. R. Mishra, H. S. Rawat, "Effect on metastable Kr atom number density due to magnetic field near extraction region

of a RF-driven discharge source", 3rd International conference on current developments in atomic, molecular, optical and nano physics, Delhi University, Dec. 14-16, (2011).

3. **S. Singh**, V. B. Tiwari, S. R. Mishra and H. S. Rawat, "Characterization of RF discharge produced metastable Kr atoms", Abstract book of DAE-BRNS National Laser Symposium, BARC, Mumbai, Feb. 6-9, (2013).

4. **S. Singh**, V. B. Tiwari, S. R. Mishra and H. S. Rawat, "Development of a magneto-optical trap for metastable Krypton atoms", Abstract book of DAE-BRNS National Laser Symposium, Manipal university, Manipal, Jan. 8-11, (2014).

5. **S. Singh**, V. B. Tiwari, Y. B. Kale, S. R. Mishra and H. S. Rawat, "Temperature measurement of cold atomic cloud in metastable Krypton MOT by transient probe absorption", Abstract book of DAE-BRNS National Laser Symposium, Sri Venkateswara University, Tirupati, Dec. 3-6, (2014).

6. **S. Singh**, V. B. Tiwari, S. R. Mishra and H. S. Rawat, "Zeeman slower beam modulated background collisions in a Krypton magneto-optical trap", Abstract book of DAE-BRNS National Laser Symposium, RRCAT, Indore, Dec. 2-5, (2015).

Surendra Singh

Dedicated to

My daughter Sandhya and son Himanshu whose love and affection act as a source of energy for me

Acknowledgments

The work presented in this thesis could not have been possible without the support of many people. It is my pleasure to acknowledge the help they have provided me from time to time throughout the thesis work.

First and foremost, I wish to express my deep sense of gratitude to my thesis guide Dr. H. S. Rawat for his trust and confidence in me. I am thankful for his valuable guidance and critical suggestions on the thesis. I am extremely grateful to him for his keen interest in my professional growth.

I sincerely thank to Dr. S. R. Mishra for enlightening discussions on the physics of the results. His critical comments on the research problems, enlightening discussions on the results has greatly contributed to the work presented here. I am also thankful to him for critically reading the thesis and various suggestions given for its improvement.

I am extremely grateful and indebted to my colleague Dr. V. B. Tiwari for his insightful guidance and continued supervision of various experiments and elaborate discussions on the results. The day to day discussion on the scientific and technical problems with him has greatly contributed to the research work and my professional growth.

I sincerely thank to Dr. P. D. Gupta, Director, RRCAT for providing all possible help for fulfilling this goal.

I am thankful to Dr. Y. B. Kale for illuminating discussion and technical help during his stay in RRCAT.

I am also grateful to Dr. S. P. Ram for day to day scientific and technical discussions on various aspect. Thanks are also due to S. K. Tiwari, Vivek Singh, Arijit Chakraborty, Amrita Shrivastva, and Amit Choudhary for technical discussions and help during the experiments.

I thank to Hari Prasad Mishra, Ajay Damke, Ankit Soni, K. R. Sethuraj and Pragya Tiwari for their contribution during the experiments.

Thanks are also due to the Doctoral Committee members Dr. S. C. Mahendale, Dr. L. M. Kukreja, Dr. S. B. Roy, Dr. K. G. Manohar and Dr. P. A. Naik for their valuable suggestions and constructive comments during doctoral committee meetings, which proved to be extremely useful in improving overall scientific quality of the work presented in the thesis.

Many of my colleagues at RRCAT from different laboratories have provided valuable help during this work. Among them, I am particularly grateful to A. Kak for fabrication of glass tube for RF discharge, H. S. Vora for developing image capturing and processing software and S. Krishnan, L. Jain and J. Khanwalkar for various electronics and instrumentation.

I also thank to the colleagues of Laser Physics Applications Section, RRCAT for providing a healthy research environment. Thanks are also due to office staff members Sapna Rege, Kailash Parmer and Jairam for their help whenever it required.

Many thanks are due to my wife Manisha, daughter Sandhya and son Himanshu for providing cheerful atmosphere at home and sacrificing their valuable time of our togetherness for accomplishing this cherished goal.

Last but not the least, I express my deepest regards to my late parents for their love, care and effort without which I wouldn't be here. I would also like to thank my brothers and sisters for their unconditional love and support.

Surendra Singh

CONTENTS

Homi Bhabha National Institute

Ph. D. Programme

1. Name of the Student	: Surendra Singh
2. Name of the Constituent Institution	: Raja Ramanna Centre for Advanced Technology
3. Enrolment No.	: PHYS03200804007
4. Title of the Thesis	:Development of a Kr magneto-optical trap for efficient loading and collision studies
5. Board of Studies	: Physical Sciences

SYNOPSIS

The laser atom cooling technique has made it possible to manipulate the external degree of motion (position and velocity) of atoms. This has become possible in the magneto-optical trap which uses light scattering force in the presence of a magnetic field to cool and trap atoms [1]. The applications of cold atoms in the experiments related to high resolution spectroscopy, precision atomic clock [2], atom lithography, cold atomic collisions [3, 4], and atom interferometry [5] are now widely known. Apart from these applications, there are several other research areas which are proving promising for the understanding of basic physics using cold atoms. These include the Bose Einstein Condensation (BEC) [5], atom-laser, cooling of fermionic atoms, quantum information [6] with cold atoms etc.

Although alkali metal atoms were the first to be cooled and still very popular, noble gas atoms present an interesting alternative class of atoms to be cooled and trapped. Laser cooling of noble gas atoms (He, Ne, Ar, Kr, Xe) [7] in the metastable state is of great importance to many research fields including cold atom collision and ionization physics in the excited state, nanolithography and atom trap trace analysis (ATTA) [8, 9]. The technique of ATTA is useful to detect rare (or low abundant) isotopes for applications in geophysics, archaeology and monitoring low level nuclear fission activities.

This thesis discusses the work carried out for the development of a magneto-optical trap (MOT) setup for laser cooling and trapping of even isotopes (^{84}Kr*, ^{86}Kr*) of Krypton atom in the excited state, its optimization and its use for the study of cold atom collisions. As the Kr atoms are cooled and trapped in the metastable excited state with a lifetime of nearly 40 s, the state preparation is the first step for laser cooling and trapping of these atoms. After the atoms are prepared in the excited state, they are transported to a chamber having appropriate pressure for the MOT formation. The Radio-frequency (RF) discharge has been employed to excite the Kr atoms in the metastable state. The laser cooling of even isotope of Kr atoms such as ^{82}Kr, ^{84}Kr and ^{86}Kr requires a wavelength of ~ 811.5 nm to drive the cooling transition between two excited states $5s[3/2]_2$ and $5p[5/2]_3$ which are without hyperfine structures. Therefore, no repumping laser is required for cooling of these isotopes. Atoms trapped in the MOT are typically cooled to a temperature of few hundreds of micro-Kelvin.

During this thesis work, various new ideas and techniques were developed for the upgradation of the MOT setup. One of them is the demonstration of a new method of generating Doppler-free signals using atomic beam fluorescence (ABF) for laser frequency stabilization. This technique is useful to increase the locking range of the cooling laser frequency and also to simplify the setup. During the production of metastable Krypton (Kr*) atoms, the Kr* atom flux transferred to MOT chamber was optimized by applying a moderate external magnetic field (~1G) in the path of Kr* atomic beam. In this optimization, the RF power and pressure in the chambers were found to play an important role. The Kr* atoms generated in a RF discharge tube in the setup were slowed down in the Zeeman slower before being cooled and trapped in the MOT. In our setup, a new concept of using two hollow laser beams for the Zeeman slower beam instead of using a conventional Gaussian beam was implemented. This significantly enhanced the loading of atoms in the MOT. Further, two isotope of Kr atoms (^{84}Kr* and ^{86}Kr*) in the excited state were simultaneously cooled and trapped in the MOT. These cold clouds of different isotopes of Kr atoms were used to study the homonuclear and the heteronuclear cold collisions.

An overview of the work carried out during this thesis work along with its organization is given below.

Chapter 1 introduces the basic principles of laser atom cooling such as Doppler and sub-Doppler cooling. The chapter includes discussion on working principle of the magneto-optical trap. Finally, the method of laser cooling and trapping of noble gas atoms and its applications are presented.

Chapter 2 discusses the energy levels of Kr atoms, RF excitation mechanism, Zeeman slower, generation and transfer of atoms through the various vacuum chambers of the MOT setup. The setup consists of a gas inlet chamber (GIC), a RF discharge glass tube (RFDT), analysis chamber (AC), pumping chamber (PC), Zeeman slower (ZS), an extraction coil and finally a cooling and trapping (MOT) chamber. The vacuum chambers of the setup are evacuated to different pressure values to maintain the flow of atoms from gas inlet chamber to the MOT chamber. The Kr* atoms are produced in a glass tube by RF-driven discharge at frequency ~ 30 MHz. The RF power is inductively coupled to Kr gas through a copper coil surrounding the glass tube. We observed that the number density increases from 2.2×10^{9} cm^{-3} to 2.0×10^{11} cm^{-3} when RF power applied on RFDT was increased from 1.5 W to 4.0 W at a pressure of ~12 mTorr. Also, we observed that there exists an optimum value of the pressure for which number density is maximum for a given RF power. The details of this work is described in this chapter.

Magnetic field assisted enhancement in the number density of the metastable Krypton (Kr*) atoms in an atomic beam generated from RF discharge plasma of Krypton gas is studied. We observed that by applying a low external magnetic field perpendicular to the beam path after the discharge tube, the number density of the Kr* atoms in the atomic beam gets enhanced. At ~ 1 Gauss of applied magnetic field, we observed nearly two-fold enhancement (from ~ 1.5×10^{6} to ~ 3×10^{6} cm^{-3}) in the number density of Kr* atoms in the atomic beam. This enhancement in the number density is attributed to the applied magnetic field assisted alignment of the path of electrons and Kr-ions along the atomic beam direction. The alignment of electrons and Kr-ions along the atomic beam direction results in increase in the number density of Kr* atoms due to occurrence of more electron-ion recombination events in the beam path. The design, development and characterization of the Zeeman slower is also discussed in this chapter. The Zeeman slower of length ~ 80 cm consists of a tapered coil having total around 7200 turns, an extraction coil and a red detuned laser beam.

Chapter 3 provides the details about the Krypton magneto-optical trap setup and its characterization. This includes discussion on frequency stabilization using saturated absorption spectroscopy and atomic beam florescence spectroscopy (ABFS). The ABFS technique is a new frequency stabilization technique devised during this work. The cold atom number in the MOT is estimated by collecting the fluorescence from the MOT cloud on a CCD camera. The temperature of the atomic cloud is estimated using a transient absorption technique where absorption of a probe beam passing through the cloud is measured as the atomic cloud expands after switching off the trap. The number of atoms obtained in the MOT was in the range of 10^5 - 10^6 at temperature of ~ 300 μK. The loading time of the MOT was observed to be ~ 250 ms. The details of these works are presented in this chapter.

Chapter 4 describes the loading studies of Kr MOT with two hollow Zeeman slower beams. A significant enhancement in the number of cold atoms in an atomic beam loaded magneto-optical trap (MOT) for metastable Kr atoms is observed when hollow laser beams are used in a Zeeman slower instead of a Gaussian laser beam. In this Zeeman slower setup, a combination of two hollow laser beams, i.e., a variable diameter hollow beam generated using a pair of axicon lenses superimposed on a fixed diameter hollow beam, has been used. The observed enhancement in the number of atoms in the MOT is attributed to reduced destruction of the atomic cloud in the MOT and increased cooling of the off axis atoms in the atomic beam, resulting from the use of hollow beams in the Zeeman slower.

The loading behaviour of Krypton magneto optical trap with variation in Zeeman slower parameters was also investigated. Our observations show that the Zeeman slower beam can modulate the background atom collisions whereas cold collisions within the trap are nearly unaffected. Therefore, the optimization of Zeeman slower parameters for enhanced loading of the MOT is an important issue and is discussed in this chapter.

Chapter 5 presents our investigation of cold collision in the two-isotope Krypton magneto-optical trap. This includes the production of the cold atomic mixture of $^{84}Kr^*$ and $^{86}Kr^*$ atoms in a magneto-optical trap (MOT) formed by overlapping the cooling laser beams for these isotopes in the same region. Approximately $2x10^5$ atoms of each isotope were trapped in the two-isotope MOT (TIMOT). We have measured the homonuclear as well as the heteronuclear trap loss rates in this TIMOT setup. Two body heteronuclear loss rate coefficient due to collisions between ^{84}Kr* and ^{86}Kr* was estimated to be $\beta_{^{84}Kr^{*}-^{86}Kr^{*}}$ = (8.7±0.8)x10^{-10} cm^3/s. The heteronuclear cold collision loss rate was found to be nearly two times the homonuclear cold collision loss rate.

Chapter 6 presents the summary and main conclusions drawn from the research work presented here. The possible future work using this noble gas atom trap is also discussed.

References:

1. H. J. Metcalf and P. Van der Straten, "Laser Cooling and Trapping", Springer-Verlag New York, (1999).
2. Claude Cohen-Tannoudji and David Guery-Odelin, "Advances in Atomic Physics: An Overview", World Scientific, Hackensack, NJ, (2011).
3. J. Weiner, V. S. Bagnato, S. Zilio and P. S. Julienne, Rev. Mod. Phys. **71,** 1 (1999).
4. W. Vassen, C. Cohen-Tannoudji, M. Leduc, D. Boiron, C. I. Westbrook, A. Truscott, K. Baldwin, G. Birkl, P. Cancio, and M. Trippenbach, Rev. Mod. Phys. **84,** 175 (2012).
5. C. J. Pethick and H. Smith, "Bose-Einstein Condensation in Dilute Gases", Cambridge University Press, 2nd ed, (2008).
6. J. J. Garcia-Ripoll, P. Zoller, and J. I. Cirac, J. Phys. B: At. Mol. Opt. Phys. **38**, S567 (2005).
7. F. Shimizu, K. Shimizu and H. Takuma, Jap. J. Appl. Phys. **26,** L1847(1987).

8. C. Y. Chen, Y. M. Li , K Bailey, T. P. O'Connor, L. Young and ZT. Lu, Science **286,** 1139 (1999).

9. Xu Du, "Realization of Radio-Krypton Dating With an Atom Trap", Ph.D. thesis, Northwestern University, Evanston Illinois, (2003).

LIST OF FIGURES

Chapter 1

Introduction

The study of interaction of light with the matter has been an important subject of research for exploring various areas of basic physics such as atomic and optical physics, atomic and molecular spectroscopy, laser cooling and laser interferometry etc. When an atom is excited by a laser light with a frequency near to its resonance frequency, the absorption or fluorescence spectra thus produced provides information about the atomic energy levels of the atom. Advancement of lasers have played an important role in the fast growth of atomic physics due to special properties such as small linewidth, tunability, coherence and high intensity of the laser radiation. The laser atom interaction can be used effectively to manipulate the motion of an atom and subsequently to reduce its average kinetic energy. This reduction in the average kinetic energy and hence reduction in the momentum spread of the atomic sample results in the effect known as laser atom cooling. The multiple absorption and emission cycles are necessary for laser cooling process to be efficient. During this process, there is a possibility of atoms to go out of the resonance with the laser and stop to participate in the further cooling of the atoms. The important laser properties required for laser cooling is its frequency stability and tunability. These properties of laser help in the proper selection of laser frequency near the resonance frequency of the atom to obtain the optimum conditions for effective laser cooling of atoms. Another important parameter for laser cooling is the intensity of laser beams which governs the temperature and the number of atoms in the cold atomic cloud.

The mechanical effect on the deflection of neutral atom by the light was first demonstrated by Frisch [1] in 1933. The technique of laser cooling of neutral atoms came much later in 1975 and was independently suggested by T. W. Hansch and A. L. Schawlow for neutral atoms [2] and by D. Wineland and H. Dehmelt for ions [3]. The technique was first experimentally demonstrated by S. Chu et al. [4] in Na atoms in 1985. Over the years, the field of laser cooling is well established and it has already received two noble prizes i. e. in 1997 to Steven Chu of Stanford university (USA), Claude Cohen-Tannoudji of College de France (France), and William D. Phillips [4-5] of National Institute of Standards and Technology, Gaithersburg (USA) for their contribution to laser atom cooling; and in 2001 to Eric Cornell of National Institute of Standard and Technology, Colorado (USA), Wolfgang Ketterle of Massachusetts Institute of Technology (USA) and Carl Wieman [6-7] of University of Colorado (USA) for their development of Bose-Einstein condensation in dilute atomic gases.

The field of laser cooling and trapping of atoms has initiated several important developments in the field of ultra high resolution spectroscopy [8-11], cold collision physics [12-14], ionizing collisions [15-18], quantum optics [19-21], generation of cold molecule [22-23], Bose-Einstein condensation [24] and matter wave optics [25] etc. Due to its importance in basic research more than 20 atoms belonging to different groups have been cooled and trapped so far. Almost all atoms belonging to the alkali series such as Lithium [26], Sodium [27], Potassium [28], Rubidium [29], Cesium [30], Francium [31] and the alkaline-earth metals such as Beryllium [32], Magnesium [33], Calcium [34], Strontium [35], Barium [36], Radium [37] and the noble gas atoms such as Helium [38-42], Neon [43], Argon [44], Krypton [44-45] and Xenon [46] have been cooled and studied. Noble gas atoms forms an important part of the series due to its applications in dating, lithography, low level detection of radioactive traces including basic physics phenomena such as penning ionization and associative ionization [47-49].

In this chapter, the mechanism of laser cooling and trapping of neutral atoms is briefly intoduced. The concept of Doppler and sub-Doppler cooling are discussed. Next, working principle of the Zeeman slower is discussed. Finally, the laser cooling of the noble gas atoms and its applications are discussed.

1.1 Basics of laser atom cooling and trapping

The basic principle of laser atom cooling is based on the exchange of momentum between an atom and the light field through absorption and emission of photons. The momentum of an atom changes by $\hbar\vec{k}$ on absorption of a laser photon having wave vector $\vec{k}$ ($|\vec{k}| = 2\pi/\lambda$, λ is the wavelength of the laser) and $\hbar$ (= h/2π) is the reduced Plank's constant. The velocity of the excited atom also changes by $\frac{\hbar\vec{k}}{m}$, where m is the mass of the atom. The excited atom when spontaneously emits a photon; it gets a recoil in the direction opposite to that of the spontaneously emitted photon. The atom thus returns to the ground state, from where it can again be excited by the absorption of light photon. After a large number of absorption-emission cycles, due to random direction of emitted photons, the net recoil to the atom in the spontaneous emission becomes nearly zero. Thus, the atom gets a directional momentum change mainly due to absorption from the laser beam. This momentum exchange between the light field and the atom can result into a significant optical force responsible for deceleration of atom to reduce its velocity and hence kinetic energy. For an atom excited to a state having natural radiative lifetime τ, the maximum radiation force on the atom is given by $\hbar k\Gamma/2$, where $\Gamma = 1/\tau$. In case of ^{84}Kr atom having mass m = 84 amu, at excitation wavelength of nearly 811.5 nm, upper state lifetime of 28.63 ns, the maximum deceleration along the laser beam direction turns out to be ~10^5 m/s^2. Such a significant optical force responsible for reducing the velocity of the atom can be extended to utilize in three dimensions for reduction of the average kinetic energy and hence the temperature of an atomic ensemble.

1.2 Doppler cooling

The process of laser cooling of atoms using Doppler effect was proposed by Hänsch and Schawlow in 1975 [2]. In this process, the lasers frequency is slightly detuned towards the lower frequency from the resonance frequency of an atom. Due to the Doppler Effect, the atom moving opposite to the laser radiation observes a frequency shift of the laser radiation towards the atomic resonance frequency resulting in an increase rate of absorption of the laser radiation. The atom moving along the direction of the laser radiation observes a laser frequency shift towards the lower side of the atomic resonance frequency and thus less absorbed by the atom. Hence, there is always an asymmetric force acts on an atom moving in the fields of two counter propagating identical laser beams. Let us consider an atom moving with a velocity $\vec{v}$ in the field of laser radiation with a frequency ω_L. The frequency of the laser radiation as observed by the atom (ω'), in its reference frame, is represented as;

$$\omega' = \omega_L - \vec{\mathrm{k}}_{\mathrm{L}}.\vec{\mathrm{v}}\,, \tag{1.1}$$

where $\vec{\mathrm{k}}_{\mathrm{L}}$ and $\vec{v}$ are the laser wave vector and the velocity of the atom respectively.

The scattering force [50], $\vec{F}_{scatt}$ can then be written in the atom's frame of reference using the new detuning, $\Delta = \Delta_L - \vec{k}_L.\vec{v}$

$$\vec{F}_{scatt} = \hbar\vec{k}_L \frac{\Gamma}{2}\left[\frac{s}{1+s+\left[2\left(\Delta_L - \vec{k}_L.\vec{v}\right)/\Gamma\right]^2}\right], \tag{1.2}$$

where Γ is the atomic linewidth and s is the saturation parameter, defined as, $s = I/I_s$, where I and I_s are the laser intensity and the saturation intensity of the atomic transition involved in the cooling respectively.

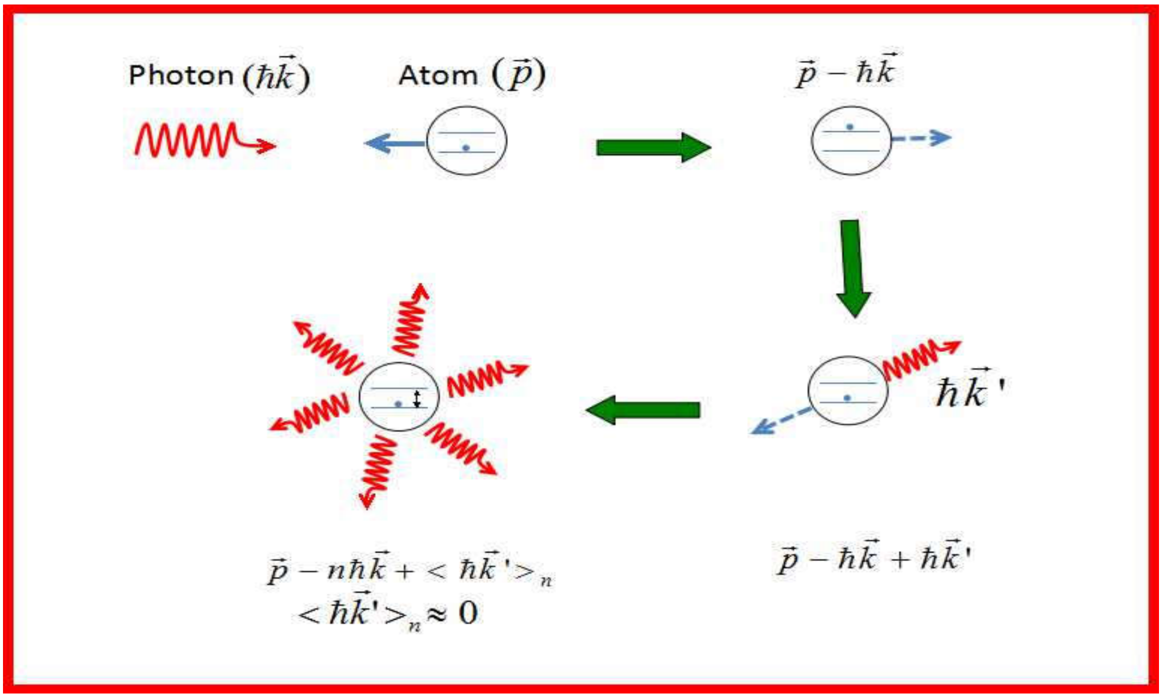

Fig. 1.1: A simplified representation of laser atom cooling process showing the absorption-emission cycles resulting in the slowing of an atom.

Now, let us consider a moving atom interacting with two counter-propagating laser beams of identical frequency, intensity and polarization. In the atom's frame of reference, the light field appears bi-chromatic with frequencies $\omega \pm |\vec{k}.\vec{v}|$. The total scattering force ($\vec{F}_{Total} = \vec{F}_+ + \vec{F}_-$) due to two counter-propagating laser beams of low intensity (s « 1) is given as [43],

$$\vec{F}_{Total} = \hbar\vec{k}_L \frac{\Gamma}{2}\left[\frac{s}{1+s+\left[2\left(\Delta_L - |\vec{k}_L.\vec{v}|\right)/\Gamma\right]^2}\right] - \hbar\vec{k}_L \frac{\Gamma}{2}\left[\frac{s}{1+s+\left[2\left(\Delta_L + |\vec{k}_L.\vec{v}|\right)/\Gamma\right]^2}\right], \quad (1.3)$$

where $\vec{F}_+$ and $\vec{F}_-$ refer to scattering forces due to laser beam propagating in the forward and the backward directions respectively. The force, F_{Total} can be further simplified in term of damping coefficient β, for $\vec{k}_L.\vec{v} << \Delta_L$ and $\vec{k}_L.\vec{v} << \Gamma$ as,

$$F_{Total} = -\beta v \,, \tag{1.4}$$

where $\beta = \dfrac{8\hbar k_L{}^2 s(\Delta_L/\Gamma)}{\left[1+s+(2\Delta_L/\Gamma)^2\right]^2}$

This force is called the Doppler cooling force and results in the reduction of temperature of the atoms. The representation of the Doppler cooling mechanism is shown in Fig. 1.1.

Thus, if one applies a laser light with a frequency less than (red detuned light) the resonant frequency of the atoms from two opposite directions, the velocity of the atoms is reduced. This is due to the fact that the atoms absorb more photons from the laser beam pointing opposite to the direction of their motion. In each absorption event, the atom loses momentum equal to the momentum of the photon and is kicked in the random directions by the spontaneous emission of the photon. The net change in the momentum of an atom averages to nearly zero over the large number of spontaneous/emission cycles. If the absorption and emission are repeated many times, the root mean square velocity, and therefore the kinetic energy of the atom will be reduced. The temperature of an ensemble of atoms is a measure of the average kinetic energy. Here, the concept of defining the temperature is different than that used in thermodynamics. The temperature (T) of an ensemble of atoms is related to the spread of the velocity distribution. The atom follow the Maxwell-Boltzmann distribution with root mean square (rms) velocity ($v_{rms} = \sqrt{\langle v^2 \rangle}$) which gives the spread in velocity (v) distribution. We can relate the thermal energy, $\frac{1}{2}k_B T$ to the v_{rms} using kinetic theory of gases as follow,

$$\frac{1}{2}k_B T = \frac{1}{2}m v_{rms}{}^2 \,, \tag{1.5}$$

where T is the temperature of the cooled atom in Kelvin and m is its mass. The reduction in v_{rms} implies the reduction in the temperature of the atomic cloud.

By using three orthogonal pairs of counter-propagating counter circularly polarized laser beams, an atom in the intersecting region of the laser beams can be cooled and its motion can be viscously confined in all the three dimensions. This mechanism is known as optical molasses. In the optical molasses, the atom undergoes as many spontaneous/emission cycles and performs a random walk in the momentum space, with a discrete step length equal to the photon momentum $\hbar k_L$, in the spatial region in which the laser beams overlap. Over the large number of spontaneous/emission cycles the average momentum change of the atom is nearly zero, but the root-mean-square momentum change is not zero. The later process results in the heating of the atomic sample. The temperature of the atomic cloud is thus determined by equilibrium between the cooling and the heating due to this diffusion process. So, the atomic cloud attain a temperature known as Doppler temperature (T_D).

The Doppler temperature is given as,

$$T_D = \frac{\hbar\Gamma}{2k_B}, \tag{1.6}$$

The Doppler cooling limit (T_D) of the temperature for Kr* is ~133 μK.

1.3 Sub-Doppler cooling

Sub-Doppler cooling such as Sisyphus cooling is a mechanism for laser cooling of atoms that uses light forces to cool atoms below the Doppler cooling limit [50-51]. In the laser cooling experiments with cesium atom in the year 1985, the temperature well below the Doppler cooling limit was observed in the optical molasses. It was realized that the simple mechanism of Doppler cooling [42] is not sufficient to explain the observation. The concept of Sisyphus cooling [53] was adopted to explain the observed results. It considers the polarization gradient, as generated by two counter-propagating linearly polarized laser beams with perpendicular polarization directions (lin ⊥ lin configuration) or circularly polarized beams with opposite circular polarization, and is therefore sometimes called polarization gradient cooling. When an atom in a certain dressed state "climb uphill", i.e. reach a position where their potential energy is relatively large, it becomes likely that they are optically pumped into another state for which the potential energy at that position is close to a minimum. In such a way, the polarization gradient introduces non-conservative force to the atoms.

The whole process of Sisyphus cooling is presented in Fig. 1.2. It involves a polarization gradient generated by two counter propagating beams either linearly polarized with perpendicular polarization directions (lin ⊥ lin configuration) or circularly polarized with opposite circular polarization (σ^+ - σ^- configuration). In two types of polarization gradients represented by the field configurations lin ⊥ lin and σ^+ - σ^- polarizations, structures of polarization variation are different. In the former case i.e lin ⊥ lin polarization, the polarization varies between linear and circular over a distance λ/8, as shown in Fig. 1.2(a). The resultant electric field is circularly polarized at positions where the two counter-propagating beams have a phase difference of ± π/2. The polarization changes from σ+ to σ- over a distance of λ/4, and between these positions, the light has elliptical or linear polarization. Fig. 1.2(b) shows the light shifted energy states at positions over a distance of wavelength for lin ⊥ lin polarization configuration. The shift in the atom's energy (ΔE_g) in the ground state magnetic sublevels because of the Stark effect due to the electric field of the light is given as [47],

$$\Delta E_g = \frac{\hbar \Delta_L I / I_s C_{ge}^2}{1 + (2\Delta_L / \Gamma)^2}, \tag{1.7}$$

where C_{ge} is the Clebsch-Gordan coefficient of the transition ground (g) $\leftrightarrow$ excited (e) state. The C_{ge}^2 gives the transition probability of the corresponding transition. The ground state light shift is negative for red detuning and positive for blue detuning of laser with respect to the atomic resonance. The light shift varies for different magnetic sublevels, as C_{ge}^2 depends on the magnetic quantum number along with the polarization of light field.

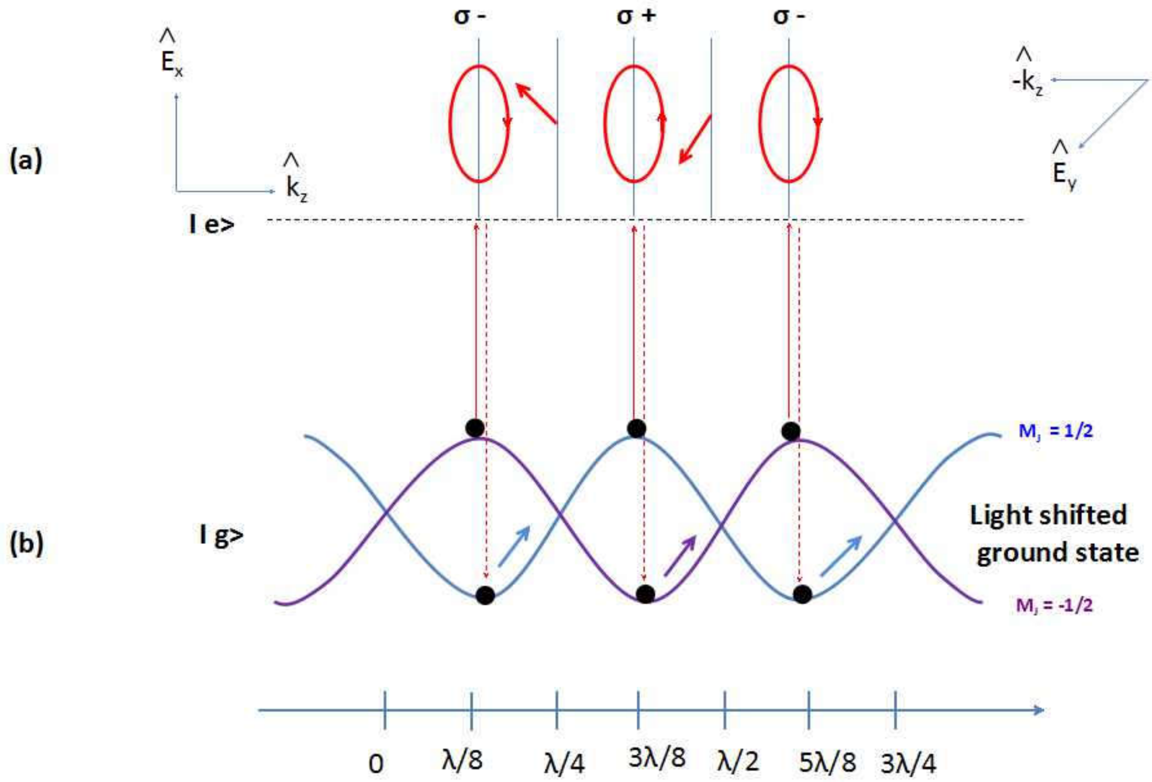

Fig. 1.2: Mechanism of Sisyphus cooling (a) showing the resultant polarization in a standing wave formed by two laser beams that propagate along z and – z direction and have orthogonal polarization. The resultant electric field is circularly polarized at positions where the two counter-propagating beams have a phase difference of ± π/2. The polarization changes from σ^+ to σ^- over a distance of λ/4, and between these positions the light has elliptical or linear polarization, (b) the light shifted energy states at positions over a distance of wavelength. The light shift varies with position and optical pumping process transfer atoms from the top of a hill to the bottom of a valley.

In the latter case, i.e., σ^+ - σ^- polarizations, the polarization is linear everywhere but the direction rotates to form a helix. It is therefore called polarization gradient cooling. When atoms in certain dressed state "climb uphill" to reach a position where their potential energy is relatively large. It becomes likely that they are optically pumped into another state for which the potential energy at that position is close to a minimum as shown in Fig. 1.2. In this way, the polarization gradient introduces non-conservative light forces, which can reduce the average kinetic energy of the atoms. This mechanism by which atoms dissipate energy as they move through a standing wave is known as Sisyphus effect. Sisyphus cooling mechanism is important as it makes it possible to cool atoms to very low temperatures ("sub-Doppler temperatures").

1.4 Magneto-optical trap (MOT)

A magneto-optical trap (MOT) is a robust technique to obtain cold atomic cloud with temperature in the range of micro Kelvin. Atoms of several groups such as alkali, alkaline-earth, noble gas atoms etc. have been cooled and trapped using MOT. The working of MOT to cool and trap atoms can be understood by considering the idealized one-dimensional scheme as shown in Fig. 1.3(a). In this scheme, the atoms are placed in a weak magnetic field B which varies linearly with distance z as B (z) = bz. The value of B is equal to zero at the central point z = 0 and negative for negative z values. For simplicity, we assume atoms to have two electronic states: the ground state with the energy E_g and the total angular momentum $J = 0$ and the excited electronic state with the energy E_e and the total angular momentum $J = 1$. The excited state in the magnetic field B(z) is split into three Zeeman magnetic sublevels, M_J = 0, ±1. The energies corresponding to the two extreme magnetic sublevels, M_J = ±1, are $E_e^{\pm 1} = \hbar\omega_0 \pm \mu_B g B(z)$, where z is the position of the atom, ω_0 is the resonance transition frequency in a zero magnetic field, μ_B is the Bohr magneton and g is the Lande's g-factor.

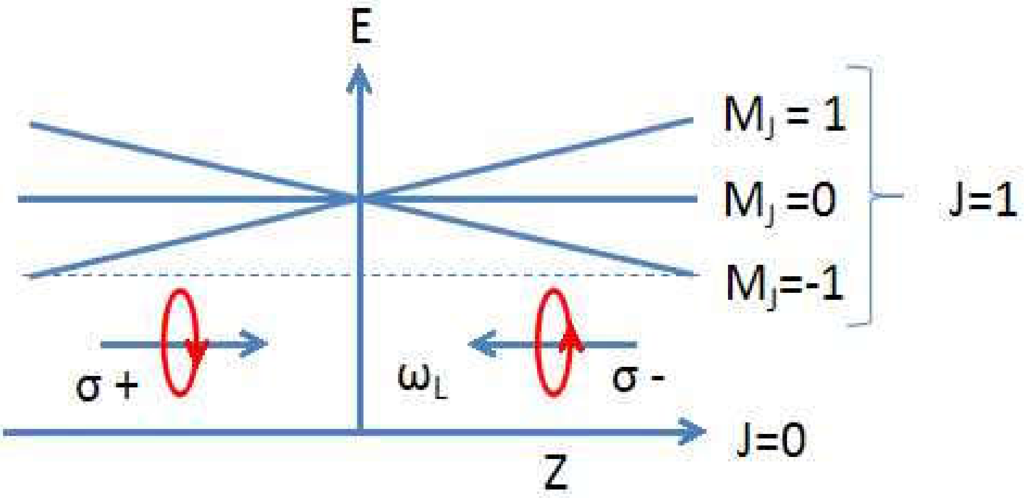

(a)

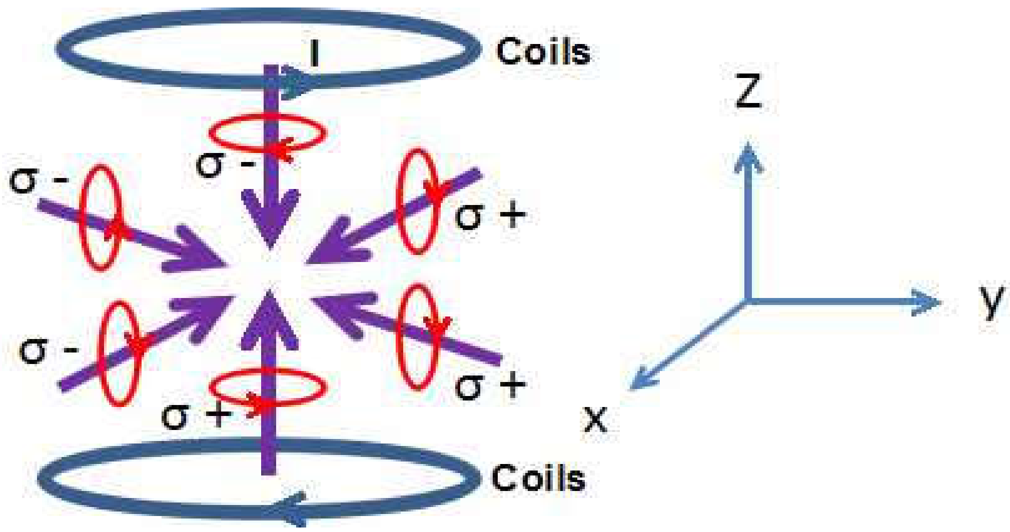

(b)

Fig. 1.3: (a) Schematic of two level system showing the Zeeman's splitting of the energy level according to the applied magnetic field and (b) Three-dimensional MOT arrangement with three pairs of mutually perpendicular counter propagating and counter circularly polarized laser beams with a pair of magnetic coils in the anti-Helmholtz configuration.

In the MOT setup, each dimension (out of three: x, y, and z) has two circularly polarized σ^+ and σ^- laser beams propagating in the opposite directions. The frequency of the laser beams is kept red-shifted ($\omega_L < \omega_0$) with respect to the transition frequency of the unperturbed atom. The atom interaction with these beams leads to cooling and trapping of atom in the region of intersection of beams.

In the above scheme, the atom is subjected to scattering caused by the transitions between the ground state and the two upper-state magnetic sublevels $M_J = \pm 1$. The rate of excitation of atoms to the upper-state sublevels depends on the position of the atoms. When the atom is moving in the positive z direction, the atom is excited with a higher probability to the magnetic sublevel $M_J = -1$ because of the less detuning of the laser with the $M_J = -1$ state compare to $M_J = 1$ state. Similarly, for an atom moving along negative z axis, will have more probability of excitation to the magnetic sublevel $M_J = 1$ state because of the less detuning of the laser with the $M_J = 1$ state compare to $M_J = -1$ state. As a result, the direction of the radiation pressure force on an atom depends on the sign of the coordinate z. When the atom coordinate is negative, $z < 0$, it mainly interacts with the σ^+ polarized radiation, and experiences a force in the positive direction of the z-axis. On the contrary, at a positive atom coordinate, $z > 0$, the atom mainly interacts with the σ^- polarized laser light and is subjected to a force in the negative direction of the z-axis. The radiation pressure force in the scheme is thus always directed opposite to the direction of motion of the atom. Accordingly, the scattering force produces a trapping potential well for atoms located at the central point $z = 0$, where all the six laser beams intersects each other.

Thus, three pairs of counter circularly polarized laser beams in the presence of inhomogeneous magnetic field are used to form the magneto-optical trap. A spherical quadrupole magnetic field having centre at the intersection of the three pair of cooling laser beams will exert a velocity dependent and position dependent force towards the centre of the MOT.

The total force on an atom in presence of two counter-propagating beams with quadrupole magnetic field gradient can be written as [50],

$$\vec{F}_{MOT} = \hbar \vec{k}_L \frac{\Gamma}{2}\left[\frac{s}{1+s+\left[2\left(\Delta_L - |\vec{k}_L.\vec{v}| + \mu B_z/\hbar\right)/\Gamma\right]^2}\right] - \hbar \vec{k}_L \frac{\Gamma}{2}\left[\frac{s}{1+s+\left[2\left(\Delta_L + |\vec{k}_L.\vec{v}| - \mu B_z/\hbar\right)/\Gamma\right]^2}\right], \tag{1.8}$$

where $\mu = (g_e m_e - g_g m_g)\mu_B B_z$ is the effective magnetic moment for the transition in magnetic substate. The g_e and g_g are Landé g factor for excited state and ground state respectively, μ_B is the Bohr magneton and B_z ($= bz$, where b $= \frac{dB_z}{dz}$) is the magnetic field in the z direction due to spherical quadrupole field. For Doppler shift and Zeeman shift values less than detuning Δ_L, above Eq. (1.8) can be approximated as [54],

$$F_{MOT} = -\beta v - \kappa z, \tag{1.9}$$

where $\kappa = \frac{\mu b}{\hbar k_L}\beta$ and $\beta = \frac{8\hbar k_L{}^2 s(\Delta_L/\Gamma)}{\left[1+s+(2\Delta_L/\Gamma)^2\right]^2}$.

The force on an atom in a MOT consist of two parts, one is velocity dependent damping force and another is position dependent restoring force.

The MOT can be conveniently loaded from a background of thermal vapour or slowed atomic beam. However, the trapping potential in a magneto-optical trap is small in comparison to thermal energies of the atoms and most collisions between trapped atoms and the background gas may supply enough energy to the trapped atom to take it out of the trap. At high background pressure, atoms are kicked out of the trap faster than they can be loaded.

So, the pressure in the MOT chamber need to be of the order of 10^{-8} Torr for typical MOT parameters.

1.5 Characterization of cold atomic cloud in a MOT

The cold atomic cloud in the temperature range of few hundreds of micro Kelvin are routinely obtained by laser atom cooling technique in a standard magneto-optical trap (MOT). Precise knowledge of physical parameters of laser cooled atomic cloud such as loading time, temperature, size and number density are of prime importance for many applications. Hence, characterization of the cold atomic cloud forms the integral part of any laser cooling setup. In the forthcoming section, characterization of our MOT setup is discussed in detail.

1.5.1 Measurement of number

The number of cold atoms in a MOT is estimated by collecting the fluorescence from the MOT cloud on a CCD camera or by collecting the fluorescence from the MOT onto the calibrated photodiode using the following treatment.

The fluorescence image captured on a charge-coupled device (CCD) camera due to scattering by a resonant beam from the cold atomic cloud can be used to estimate the number of atoms in a MOT. A CCD is a light-sensitive integrated circuit consists of picture elements (called pixel) that stores and displays the data for an image in such a way that each pixel in the image is converted into an electrical charge. The stored electrical charge is proportional to the intensity of the light falling on the CCD pixel in its linear working range. In this imaging technique, the size of the cold atomic cloud is also deduced from the same image and can be used for estimation of the number density.

A cold atomic cloud with N number of atoms scatter photons isotropically with a rate γ_{sc}, when shined with a light of intensity I and detuning Δ. The scattering rate γ_{sc} is given by Eq. (1.10) [50]

$$\gamma_{sc} = \frac{\Gamma}{2}\left[\frac{I/I_s}{1+I/I_s+4[\Delta/\Gamma]^2}\right]. \tag{1.10}$$

The number of photons N_p collected in a solid angle dΩ subtended on the collecting lens used to image on the CCD camera with an exposure time (t_{exp}) is given by [55],

$$N_p = N.\gamma_{sc}.\frac{d\Omega}{4\pi}.t_{\exp}. \tag{1.11}$$

The output voltage from a pixel is converted into a digital number (called counts) during readout. If η is the quantum efficiency of the CCD camera, then N_p photons can be converted into CCD count using N_c, = N_p.η. Where η is the quantum efficiency of the CCD camera which is the ratio of the number of charge carriers generated to the number of photons falling on it.

Now, the number of cold atoms in the cloud N is inferred as,

$$N = \frac{8\pi\left[1+\left(6\frac{I}{I_s}\right)+4\left(\frac{\Delta_L}{\Gamma}\right)^2\right]}{\Gamma\left(6\frac{I}{I_s}\right)t_{\exp}\eta d\Omega}N_c, \tag{1.12}$$

where I_s is the saturation intensity, I is the intensity of each cooling beam in the MOT, Γ is the natural linewidth of cooling transition.

The number of atoms in a MOT can also be estimated by counting the number of photons reaching to the photodiode detector. A photodiode is a semiconductor device that converts light photons into the current. The current in the detector circuit is produced due to the generation of electron hole pair in the photodiode by the incident photons. The output voltage from the photodiode detector circuit is calibrated with the incident laser power. Let *dΩ* be the solid angle subtended by the detector at the trap centre. Then, the number of atoms in the MOT can be given by,

$$N = \frac{4\pi}{hc} \cdot \frac{\lambda}{\Omega} \cdot \frac{P}{\gamma_{sc}}, \tag{1.13}$$

where P is the power collected onto the calibrated photodiode.

1.5.2 Measurement of temperature

There are several methods to estimate the temperature of the cold atomic cloud in a MOT. The commonly used methods are free expansion method, time of flight method, fluorescence decay, release and recapture, fountain and size determination of the atomic cloud etc. [56-57]. Transient absorption technique is also used to measure the temperature where the number of cold atoms available in the MOT are low [58-59]. The use of transient absorption technique to measure the temperature of the Kr*-MOT is demonstrated, where the number of cold atoms are low. It was also concluded that for the low number of atoms in the MOT, this technique works better than the commonly used method of free-expansion. This is perhaps due to weak fluorescence signal from the cloud over a small solid angle of the detection. The results of the temperature measurements by the transient absorption technique was compared with the results of temperature measurement by the size of the cloud and found to be comparable.

As discussed before, the cold atom number and the size of the MOT are estimated by collecting the fluorescence from MOT cloud on a CCD camera. In the Kr*-MOT (cold atom number ~ 5×10^5), there was a proportional increase in the density of the trapped atoms with the number of trapped atoms in the Kr*-MOT indicating that the MOT operation is in the constant volume regime. The spatial time dependent density ($n(r,t)$) distribution of the trapped atoms follows a Gaussian function in such a constant volume regime and can be written as [60],

$$n(r,t) = n_0(t)e^{-r^2/2\rho^2}, \tag{1.14}$$

where $n_0(t)$ is the peak cold atom number density at time t during the loading of the MOT, r is the distance from the trap centre and ρ is the rms radius of the Gaussian density distribution. In general ρ is a function of time but for the constant volume MOT operation regime, ρ is time independent.

In the transient probe absorption technique, absorption of a weak probe beam passing through the atomic cloud in the MOT during the free expansion of the cloud is measured using a photodiode detector. When MOT beams are switched-off, the time evolution of the absorption signal gives the information about the atomic density at different time during the free-expansion of the cloud. The transmitted intensity (I) at different time (t) can be expressed as follows [58],

$$\frac{I}{I_0} = \exp\left[-\frac{\sigma N_0}{\pi(\rho_z^{\,2} + v_{rms}^{\,2}t^2)}\right], \tag{1.15}$$

where I_0 is the initial intensity of the probe beam before passing through the cold atomic cloud, ρ_z is the initial rms radius of the cloud along z-axis, σ is the absorption cross section of the ^{84}Kr* atom at wavelength 811.5 nm, N_0 is the initial number of atoms in the MOT, v_{rms} is the rms speed of the atoms in the MOT and is given as $v_{rms}^{\,2} = \frac{k_B T}{m}$, where m is the mass of the ^{84}Kr atom. On substituting the value of v_{rms} in Eq. (1.15), the final expression becomes,

$$\frac{I}{I_0} = \exp\left[-\frac{\sigma N_0}{\pi({\rho_z}^2 + \frac{k_B T}{m} t^2)} \right]. \tag{1.16}$$

Temperature of the cold atomic cloud can also be estimated by size determination technique. When particles with Maxwell-Boltzmann velocity distribution are trapped in a harmonic potential, the density distribution is Gaussian. Then for each coordinate of the harmonic trap, the ensemble averaged potential energy $\kappa_i < \rho_i^2 >/2$ is equal to the $k_B T/2$, where i = 1, 2 and 3 correspond to x, y and z directions respectively and the corresponding ρ_i is represented by ρ_x, ρ_y and ρ_z, k_B is the Boltzmann constant and κ is the spring constant which depends upon the MOT parameters as follows [54]

$$\kappa = \mu_B \frac{2\pi}{\lambda} \frac{dB}{dz} \frac{\left[8 \frac{\Delta_L}{\Gamma} \frac{I}{I_s} \right]}{\left[1 + 6 \frac{I}{I_s} + \left(\frac{\Delta_L}{\Gamma} \right)^2 \right]^2}, \tag{1.17}$$

where μ_B is the Bohr magneton, $\frac{2\pi}{\lambda}$ is the magnitude of the wave vector, $\frac{dB}{dz}$ is the magnetic field gradient, Δ_L is the laser detuning, Γ is the linewidth and I and I_s are the single beam intensity and saturation intensity respectively.

Thus,

$$T = \frac{\kappa {\rho_z}^2}{k_B}. \tag{1.18}$$

After substituting the value of κ estimated from Eq. (1.17) and ρ_z from CCD camera in Eq. (1.18), temperature of the cold atomic cloud, T can be estimated.

1.5.3 Measurement of MOT loading rate

Loading studies is one of the essential part of characterization of any MOT setup. Loading rate is the number of atoms being captured in a MOT per unit time. The number of atoms loaded in a MOT at any instant of time *t*, is given as $N = N_s[1-\exp(-t/t_L)]$, where N_s is the steady state cold atoms number and t_L is the loading time. The loading time is defined as the time required to trap 67% of the maximum number of the atom in the MOT. The loading rate and the loading time is governed by the trap parameters, pressure and various loss mechanisms involving collision of the trapped atom with the background atoms and cold collision within the trap. Collision of the trapped atoms with the background atoms, light assisted collisions, collision between cold atoms are the different loss mechanisms associated with the MOT.

The temporal evolution of number of cold atoms (*N(t)*) in a MOT is given by

$$\frac{dN(t)}{dt} = L - \gamma N(t) - \beta \int_V n^2(r,t) d^3r, \tag{1.19}$$

where *L* is the MOT loading rate, *γ* is the background collision loss rate coefficient for ^{84}Kr*, *n(r, t)* is number density of the cold atoms, *β* is the cold collision loss rate coefficient due to collision between two cold atoms.

The number density distribution of cold atoms in the constant volume case is given by Eq. 1.14. In order to estimate the MOT loading rate *L*, the background collision loss rate coefficient γ and cold collision loss rate coefficient *β*. Eq. (1.19) was integrated over the trap volumes by using number density distribution given by Eq. (1.14). The following loading equation for MOT is obtained,

$$\frac{dN(t)}{dt} = L - \gamma N(t) - \beta \frac{N^2(t)}{2^{3/2} V}, \tag{1.20}$$

where, $V(=(2\pi)^{3/2}\rho^3)$ is the trap volume for spherical cloud ($\rho_x = \rho_y = \rho_z = \rho$) and the solution of Eq. (1.20) is given as

$$N(t) = N_s\left[1 - \frac{(1+\xi)\exp(-t/t_L)}{1+\xi\exp(-t/t_L)}\right], \tag{1.21}$$

where, $t_L = \left[\frac{(1-\xi)}{(1+\xi)}\frac{1}{\gamma}\right]$ and $\xi = 1 - \frac{N_s\gamma}{L}$ (1.22)

At steady state $\left(\frac{dN(t)}{dt} = 0\right)$, $L = \gamma N_s + \beta\frac{N_s^2}{2^{3/2}V}$

and $\xi = \left[1 + \sqrt{8}\frac{\gamma}{\beta_1 n_{0s}}\right]^{-1}$. (1.23)

N_s and n_{0s} are the steady state number and the steady state peak number density of the MOT cloud and t_L is the loading time of the MOT. The values of γ and β for the MOT can be estimated by fitting Eq. (1.21) to the experimentally observed MOT loading curve of the atoms in the MOT cloud.

1.6 Laser cooling of noble gas atoms and their applications

The laser cooling of noble gas atoms is accomplished in the metastable state unlike the alkali atoms where laser cooling is achieved in the ground state. The amount of energy needed to excite the ground state atom to its excited energy state is very large (~10-20 eV). In the case of the Krypton atom, the first excited state is metastable state (~ 40 s) which is ~10 eV (120 nm) away from the ground state. Also, the transition to the first excited state from the ground state is dipole forbidden. Thus, it is convenient to cool and trap Kr atoms in the metastable state which can be performed using laser radiation of wavelength ~ 811.5 nm. The excitation to this metastable state can be done by various techniques. Radio frequency (RF) discharge is widely used technique to produce metastable noble gas atoms due to its simplicity. The number of metastable atoms produced using this method depends on the RF power and pressure used in the discharge tube. The metastable atoms generated using this method move towards the trapping chamber in a form of atomic beam with velocity much higher than the capture velocity of the MOT. For, an efficient loading of the MOT, pre-cooling (or slowing) of atoms in the longitudinal direction is required before they are captured in the MOT. The process of pre-cooling is achieved by using the Zeeman slower, in which a suitable laser beam is used opposite to the direction of the atomic beam for pre-cooling the atoms in the beam. For the maximum absorption of the laser light by the atoms during pre-cooling in the Zeeman slower, the frequency of the laser light is tuned in such a way that the moving atoms observe the frequency of the laser near to their resonant frequency. However, the Doppler shifted light frequency observed by the atoms changes as the atoms slow down during its motion in the Zeeman slower. Therefore, to keep the laser tuned to the resonant frequency of the atoms, either laser frequency is required to change continuously or a variable magnetic field is required to tune the atomic transition frequency in the Zeeman slower. In the later case, the purpose is to change the resonant frequency using a variable magnetic field in such a way that it compensates for the change in speed of the atoms. Metastable atoms generated in the discharge tube enter into the Zeeman slower are continuously slowed down and then further cooled and trapped in the MOT. A schematic of a typical experimental setup for laser cooling and trapping of the metastable Kr (Kr*) atoms is shown in Fig. 1.4 [61, 62].

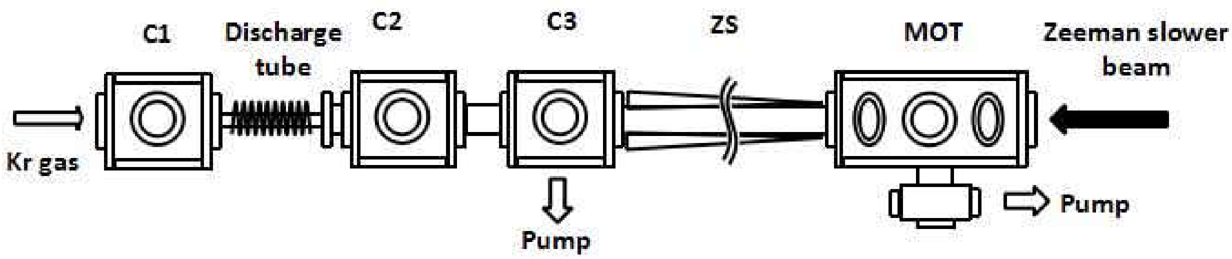

Fig. 1.4: Schematic of the experimental setup for laser cooling and trapping of the metastable Kr atoms. C1, C2, C3: different vacuum chambers; ZS: Zeeman slower; MOT: magneto-optical trap.

The setup consists of a gas inlet chamber (C1), a RF discharge tube, an analysis chamber (C2), pumping chamber (C3), Zeeman slower (ZS), and a MOT chamber. The gas first flows into the gas inlet chamber and then in the RF discharge glass tube. The metastable atoms are produced in this tube by RF-driven discharge. The analysis chamber (C2) pressure (~10^{-5} Torr) is kept lower than the pressure in the discharge tube (~10^{-3} Torr), to allow the flow of RF excited gas into this chamber. This gas subsequently flows into the pumping chamber (C3), the Zeeman slower and the MOT chamber, which are kept at successively lower pressure values. The Zeeman slower (ZS) tube connected between the pumping chamber and the MOT chamber to slow down the Kr* beam before cooling and trapping in the MOT chamber. Atoms emanating from discharge region move out in the form of a atomic beam. Transverse cooling is usually performed in the analysis chamber (C2) for reducing the divergence of the atomic beam in the transverse direction. This results into increase in the flux of Kr* atoms in the forward direction. But, in this setup, transverse cooling was not performed as pure sample of Kr gas was being used. Also sufficient flux of Kr* atoms was obtained for the study.

The metastable Kr atoms can be laser cooled by using a laser of appropriate frequency to excite the $4p^55s[3/2]_2$ to $4p^55p[5/2]_3$ transition. The longitudinal cooling of metastable atoms needs to be performed in a Zeeman slower so that the atoms speed is brought lower than the capture speed of the magneto-optical trap (MOT). The MOT serves as an important tool to provide the sample of cooled and trapped atoms for various experiments including study of inter-atomic interactions. Such interactions, either in the absence or in presence of near resonant light, manifest in the form of cold atom collisions. The cold atom collisions generally refer to the case when colliding atoms have de Broglie wavelength comparable or larger than the range of the inter-atomic distance. The homonuclear cold collisions have been extensively studied and used to generate a reliable source of cold molecules. Another interesting inter-species cold atomic mixture is produced by simultaneously cooling and trapping of the alkali metal and metastable state noble gas atoms. The high value of internal energy associated with metastable noble gas (Ng*) atoms in the MOT, leads to a process known as Penning ionization ($Ng^* + Ng^* \rightarrow Ng^+ + Ng + e^-$) and associative ionization ($Ng^* + Ng^* \rightarrow Ng_2^+ + e^-$) which makes it interesting to study.

Laser cooling of Kr atoms to a temperature of few hundreds of micro-Kelvin, have many applications in the field of high resolution spectroscopy, atom trap trace analysis, collision studies and dating etc. Since noble gases are chemically inert, dating of their radio isotopes is immune to the chemical interactions which can alter the isotopic abundance in the transport processes. Therefore noble gas radio isotope tracers have advantages over the reactive element tracers (such as ^{14}C), the interpretation of their abundance data is much simpler and consequently would lead to more accurate age information of the sample. The time range of ^{14}C-dating is from a few hundred years to 50,000 years. In order to cover the dating range from the present to a few million years, more radioisotope tracers are needed. There are three long-lived noble gas radioisotopes which are believed to be the ideal tracers to fill the gaps; ^{85}Kr ($t_{1/2}$ = 10.76 yr) is used as a tracer in the time range from the present to 50 years, ^{39}Ar ($t_{1/2}$ = 268 yr) is used between 40 years to 1,000 years, ^{81}Kr ($t_{1/2}$ = 230 kyr) can be used in the range from 50,000 years to a million years.

Atom trap trace analysis (ATTA) has become an essential tool for low level detection of radioactive traces. Since ^{235}U (or ^{239}Pu) nucleus splits into less massive nuclei in the fission, including ^{85}Kr and a few neutrons, the ATTA setup for ^{85}Kr (natural abundance 2×10^{-11}, $t_{1/2}$ = 10.76 Yrs) can be used as a tracer for monitoring nuclear fission activities [63]. ATTA is unique among trace analysis techniques as it is free of interferences from other isotopes, isobars, or molecular species and can be used to detect single photon. Low level detection of ^{85}Kr may also be used as a tracer to monitor the nuclear-fuel reprocessing activities to alarm the hazard to human body. Further, fission isotopes are monitored to assess the contamination of the environment either by the regular operation of a nuclear facility or by a nuclear accident.

References:

1. R. Frisch, Z. Phys., **86**, 42 (1933).
2. T. Hansch and A. Schawlow, Opt. Commun. **13**, 68 (1975).
3. D. Wineland and H. Dehmelt, Bull. Am. Phys. Soc. **20**, 637 (1975)
4. S. Chu, L. Hollberg, J. E. Bjorkholm, A. Cable and A. Ashkin, Phys. Rev. Lett. **55**, 48 (1985).
5. S. Chu and C. N. Cohen-Tannoudji, Rev. Mod. Phys. **70**, 707 (1998),
6. W. D. Phillips, C. E. Wieman, D. E. Pritchard and D. J. Wineland, Rev. Mod. Phys. **71**, S253(1999)
7. E. A. Cornell and C. E. Wieman, Rev. Mod. Phys. **74**, 875 (2002).
8. C. J. Borde, "Atomic interferometry and laser spectroscopy," in "Laser spectroscopy X: Proceedings of the 10th international conference", M. Ducloy, E. Giacobino, and G. Camy, eds. (World Scientific Publishing Co Pte Ltd, Font-Romen, France, 1991).
9. C. J. Borde, "Matter wave interferometers: a synthetic approach" in "Atom Interferometry", P. R. Berman ed. (Academic Press Inc., CA 1997), PP. 257-292.
10. A. Peters, K. Y. Chung, and S. Chu, Metrologia **38**, 25-61 (2001).
11. H. Perrin, P. Lemonde, F. P. dos Santos, V. Josse, B L. Tolra, F. Chevy and D. Comarat, Comptes Rendus Physique **12**, 417-432 (2011).
12. P. L. Gould, P. D. Lett, P. S. Julienne, W. D. Phillips, H. R. Thorsheim and J. Weiner, Phys. Rev. Lett. **60**, 788 1988.
13. M. Prentiss, A. Cable, J. E. Bjorkholm, S. Chu, E. L. Raab and D. E. Pritchard, Opt. Lett. **13**, 452 1988.
14. J. Weiner, Cold and Ultracold Collisions in Quantum Micro-scopic and Mesoscopic Systems Cambridge University Press, Cambridge, U.K., 2003.

15. H. C. Mastwijk, J. W. Thomsen, P. van der Straten, and A. Niehaus, Phys. Rev. Lett. **80**, 5516 1998.

16. P. J. J. Tol, N. Herschbach, E. A. Hessels, W. Hogervorst, and W. Vassen, Phys. Rev. A **60**, R761 1999.

17. M. Kumakura and N. Morita, Phys. Rev. Lett. **82**, 2848 1999.

18. N. Herschbach, P. J. J. Tol, W. Hogervorst, and W. Vassen, Phys. Rev. A **61**, 050702(R) 2000.

19. L.V. Hau, S. E. Harris, Z. Dutton, and C. H. Behroozi, Nature **397**, 594 (1999).

20. M. Fleischhauer and M. D. Lukin, Phys. Rev. Lett. **84**, 5094, (2000).

21. G. Gilbert, A. Aspect, and C. Fabre, Introduction to Quantum optics (Cambridge university press, 2010.

22. M. J. Kevin , Eite Tiesinga, P. D. Lett, and P. S. Julienne, Rev. Mod. Phys. **78**, 483 (2006).

23. C. R. Menegatti, B. S. Marangoni and L. G. Marcassa, Laser Physics **18**, 1305 (2008).

24. C. J. Pethick and H. Smith, Bose-Einstein condensation in dilute gases, Cambridge university press, 2008, 2nd ed.

25. P. Meystre, Atom optics, springer, 2001.

26. Z. Lin, K. Shimizu, M. Zhan, F. Shimzu and H. Takuma, Jpn. J. Appl. Phys. **30**, L1314 (1991).

27. Paul D. Lett, Richard N. Watts, Christoph I. Westbrook, and William D. Phillips, Phys. Rev. Lett. **61**, 169 (1988).

28. M. Landini, S. Roy, L. Carcagn, D. Trypogeorgos, M. Fattori, M. Inguscio and G. Modugno, Phys. Rev. A **84**, 043432 (2011)

29. B. Sheehy, S.-Q. Shang, P. van der Straten and H. Metcalf, Chemical Physics **145**, 317(1990).

30. C. Solomon, J. Dalibard, W. D. Phillips, A. Clairon and S. Guellati, Europhys. Lett. **12**, 683 (1990).

31. S. N. Atutov, V. Biancalana, A. Burchianti, R. Calabrese, L. Corradi, A. Dainelli, V. Guidi, A. Khanbekyan, C. Marinelli, E. Mariotti, P. Minguzzi, L. Moi, Z. Peshev, S. Sanguinetti, G. Stancari, L. Tomassetti, and S. Veronesi, Laser Phys. **15**, 1080 (2005).

32. F. M. J. Cozijn, J. Biesheuve, A. S. Flores, W. Ubachs,1 G. Blume, A. Wicht, K. Paschke, G. Erbert, and J. C. J. Koelemeij, Opt. Lett. **38**, 2370 (2013).

33. Z. Andelkovic, R. Cazan and W. Nortershauser, Phys. Rev. A **87**, 033423 (2013).

34. Shinji Urabe, Masayoshi Watanabe, Hidetsuka Imajo, and Kazuhiro Hayasaka, Opt. Lett. **17**, 1140 (1992).

35. Xinye Xu, Thomas H. Loftus, John L. Hall, Alan Gallagher, and Jun Ye, J. Opt. Soc. Am. B **20**, 968 (2003).

36. S. De, U. Dammalapati, K. Jungmann, and L. Willmann, Phys. Rev. A **79**, 041402 (2009).

37. J. R. Guest, N. D. Scielzo, I. Ahmad, K. Bailey,J. P. Greene, R. J. Holt, Phys. Rev. Lett. **98**, 093001 (2007).

38. W. Rooijakkers, W. Hogervorst, W. Vassen, Opt. Commun. **135**, 149 (1997).

39. W. Vassen, C. R. Acad. Sci. Paris, t.2, Serie IV, 613 (2001).

40. J. Lawall, S. Kulin, B. Saubamea, N. Bigelow, M. Leduc, and C. Cohen-Tannoudji, Phys. Rev. Lett. 75, 4194 (1995).

41. J. M. McNamara, R. J. W. Stas, W. Hogervorst and W. Vassen, Phys. Rev. A 75, 062715 (2007).

42. W. Vassen, C. Cohen-Tannoudji, M. Leduc, D. Boiron, C. I. Westbrook , A. Truscott, K Baldwin, G Birkl, P Cancio, and M. Trippenbach, Rev. Mod. Phys. 84, 175 (2012).

43. Fujio Shimizu, Phys. Rev. A **39**, 2758 (1989).

44. Hitetoshi Katori and Fujio Shimizu, Jpn. J. Appl. Phys. **29**, L2124 (1990).

45. Xu Du, "Realization of Radio-Krypton Dating With an Atom Trap", Ph.D. thesis, Northwestern University, Evanston Illinois, (2003).

46. K. A. Suominen and K. Burnett, Phys. Rev. A **53**, 1678 (1996).

47. Methods of low-level counting and spectrometry, Proceeding of a symposium, Berlin, (1981).

48. J. Arnold and W. Libby, Science 110, 678 (1949).

49. W. Libby. Radiocarbon dating. Nobel Lecture, December 12, 1960.

50. C. J. Foot, Atomic Physics, Oxford University Press Inc. New York, (2005).

51. P. D. Lett, W. D. Phillips, S. L. Rolston, C. E. Tanner, R. N. Watts, C. I. Westbrook, J. Opt. Soc. Am. B **6**, 2084 (1989).

52. D. S. Weiss, E. Riis, Y. Shevy, P. J. Ungar, S. Chu, J. Opt. Soc. Am. B **6**, 2072 (1989).

53. J. Dalibard, C. Cohen-Tannoudji, J. Opt. Soc. Am. B **6**, 2023 (1989).

54. H. J. Metcalf, P. van der Straten: Laser cooling and trapping, Springer-Verlag NY, Inc. (1999).

55. Surjya Prakash Ram, "Studies on generation and manipulation of laser cooled Atoms", Ph.D. thesis, Homi Bhabha National Institute, Indore, India (2003).

56. Hema Ramachandran, Current Science **76**, 213(1999).

57. X. Xu, T. H. Loftus, M. J. Smith, J. H. Hall, A. Gallagher, and J. Ye, Phys. Rev. A **66**, 011 401(R) (2002).

58. Xinye Xu, Thomas H. Loftus, John L. Hall, Allen Gallagher and Jun Ye, J. Opt. Soc. Am. B **20**, 968 (2003).

59. R. R. Silva, K. M. F. Magalhaes, E. A. L. Henn, L. G. Marcassa, V. S. Bagneto, Opt. Commun. **265**, 526(2006).

60. Vibhuti Bhushan Tiwari, “Studies with laser cooled and trapped Rb atoms”, Ph.D. Thesis, Devi Ahilya Vishwavidyalaya, Indore, India (2009)

61. S. Singh, Vivek Singh, V. B. Tiwari, S. R. Mishra and H. S. Rawat, Indian Journal of Pure and Applied Physics, **51**, 230(2013).

62. S. Singh, V. B. Tiwari, S. R. Mishra and H. S. Rawat, Laser Phys. **24**, 025501 (2014).

63. C. Y. Chen, Y. M. Li, K. Bailey,T. P. O’Connor, L. Young, Z.-T. Lu, Science, **286**, 1139 (1999)

Chapter 2

Generation and transfer of metastable Kr atoms through the vacuum chambers

2.1 Introduction

The laser cooling of noble gas atoms is generally accomplished in the metastable state, since the laser (with larger photon energy) required for the ground state excitation for laser cooling and trapping are not available. In case of the Krypton atom, the first excited state is metastable state which is ~ 120 nm (~10 eV) higher from the ground state [1-2]. Also, the transition to the first excited state from the ground state is dipole forbidden. Thus, it is convenient to cool and trap Kr atom in the metastable state which can be excited to the higher state using ~811.5 nm laser radiation. The Kr atoms in the metastable state (denoted as Kr* atoms) can be prepared by electron beam excitation [3], optical excitation [4], DC glow discharge [5], RF discharge [6] and microwave discharge [7]. Among these, the RF discharge method is most widely used due to its simplicity in implementation. The number of Kr* atoms produced using this method depends on the RF power used for the excitation of the atoms and the pressure of the gas in the discharge tube. The Generation and transfer of atoms through various vacuum chambers as well as the design, development and characterization of the Zeeman slower is presented in this chapter.

2.2 Energy levels of Kr atoms:

Natural Krypton gas has several stable isotopes such as ^{78}Kr (isotopic abundance = 0.35%), ^{80}Kr (2.25%), ^{82}Kr (11.6%), ^{83}Kr (11.5%), ^{84}Kr (57%), ^{86}Kr (17.3%) and two long lived radioactive isotopes ^{85}Kr (half life = 10.76 yrs, isotopic abundance = 2×10^{-11}) and ^{81}Kr (half life = 230 kyrs, isotopic abundance = 6×10^{-13}). The even isotopes of the Kr gas atoms do not have a nuclear spin (I) and therefore they do not have any hyperfine structure in the energy levels. Since, the last shell of the electronic configuration is not closed, the Kr* atoms have both the orbital as well as the spin angular momenta.

The electronic configuration of Krypton (having atomic number 36) is $1s^2\ 2s^22p^6\ 3s^23p^63d^{10}\ 4s^24p^6$. The ground state level is $4p^6$ (completely filled shell), for which total orbital, total spin and total electronic angular momentum are all zero and can be represented as $\vec{L} = 0$, $\vec{S} = 0$ and $\vec{J} = 0$. The electronic configuration of Kr* formed by the excitation of a valence electron from (p to s orbital) the outermost shell is $4s^24p^55s^1$ and it has one electron in the 5s orbital (called valence or outer electron) and one unpaired electron in the 4p orbital (called core electron). It is to be noted that in metastable noble gas atoms, electrostatic interaction of the core electron with the outer electron is weak as compared to the spin-orbit interaction of the core electrons but is strong compared to the spin coupling of the outer electron. Hence, first $\vec{L}$ and $\vec{S}$ are coupled to give angular momentum of the core electrons $\vec{j}$ and this $\vec{j}$ is then coupled to the orbital angular momentum $\vec{l}$ of the valence electron to form the angular momentum $\vec{K}$. Such a scheme is known as jl coupling [8]. Finally, $\vec{K}$ is coupled to the spin $\vec{s}$ of the valence electron to form the total electronic angular momentum $\vec{J}$. The notation for the energy states is then given by $^{2S+1}L_j\ n\ l\ [K]_J$, with n the principal quantum number of the outer electron.

In case of Kr atoms, the core of the first excited state ($4s^24p^55s^1$) possesses both total angular momentum ($\vec{L}$) and total spin angular momentum ($\vec{S}$). The sum of these angular momenta is denoted by $\vec{j}$. The total angular momentum J of the electrons is estimated by addition of $\vec{j}$ with the orbital angular momentum ($\vec{l}$) and spin angular momentum ($\vec{s}$) of the valence electron as described in the previous paragraph. The procedure for calculation is given below,

$$\vec{j} = \vec{L} + \vec{S},$$

$$\vec{K} = \vec{j} + \vec{l}$$

$$\text{and } \vec{J} = \vec{K} + \vec{s}\,.$$

The first excited state ($4s^2 4p^5 5s^1$) which is metastable state (lifetime, $\tau \sim 40$ s) has $L = 1$, $S = 1/2$ which gives $j = 3/2$, 1/2 for core electron. The valence electron has $l = 0$ and s = 1/2, which gives $K = 3/2$, 1/2 and $J = 0$, 1 and 2. Fig. 2.1 shows the partial energy levels diagram showing the metastable energy state for $K = 3/2$ and $J = 2$ which is used as lower state for cooling transition. This state is represented as $4p^5 5s[3/2]_2$.

Further, excitation to energy level $4s^2 4p^5 5p$ (lifetime, $\tau \sim 28.63$ ns) for spectroscopy and laser cooling is achieved by laser light of wavelength, $\lambda \sim 811.5$ nm. $4p^5 5p$ has $L = 1$, $S = 1/2$ which gives j = 3/2, 1/2 for core electron. The valence electron has $l = 1$ and $s = 1/2$, thus for $j = 3/2$, $K = 5/2$, 3/2, 1/2 and for $j = 1/2$, $K = 3/2$, 1/2. Accordingly there will be different J for different K. For $K = 5/2$, $J = 3$, 2, for $K = 3/2$, $J = 2$, 1 and for $K = 1/2$, $J = 1$, 0. The excited state energy level with $K = 5/2$ and $J = 3$ is represented as $4p^5 5p[5/2]_3$ and is shown in the Fig. 2.1.

However, for odd isotopes, $4p^5 5s[3/2]_2$ and $4p^5 5p[5/2]_3$ states are split into many energy levels ($\vec{F}$) due to hyperfine interaction of the total electronic angular momentum ($\vec{J}$) of the atom with the nuclear spin ($\vec{I}$) and is given by $\vec{F} = \vec{J} + \vec{I}$. $\vec{F}$ is known as total angular momentum of the atom. The energy level diagram for ^{83}Kr (nuclear spin $I = 9/2$) atoms along with frequency separation between hyperfine levels is shown in the Fig. 2.2. Transitions relevant to ^{83}Kr cooling and repumping are also shown in Fig. 2.2.

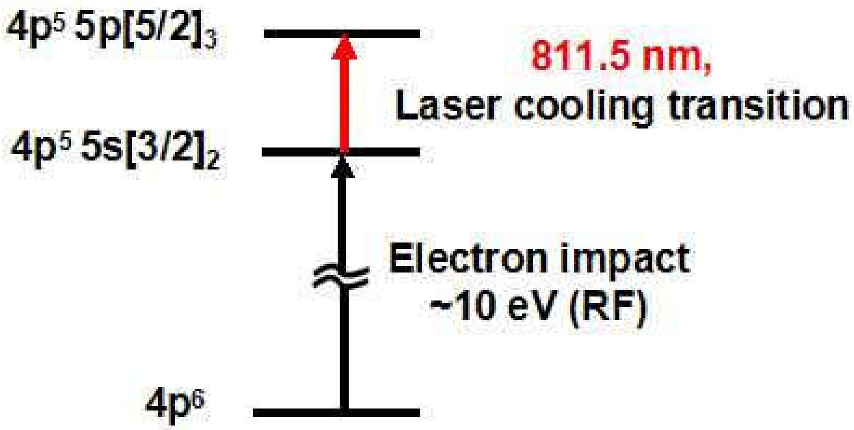

Fig. 2.1: Energy level diagram of ^{78}Kr, ^{80}Kr, ^{82}Kr, ^{84}Kr and ^{86}Kr with relevant cooling transitions.

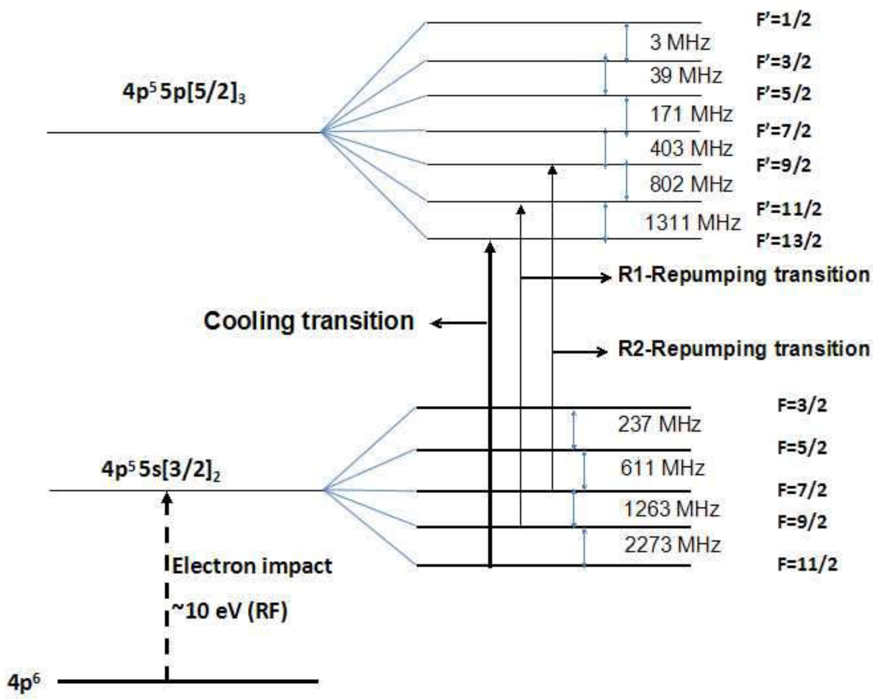

Fig. 2.2: Energy level diagram of ^{83}Kr isotope with frequency separation and relevant cooling transitions.

2.3 Generation of Kr* atoms:

The laser cooling of the noble gas Kr atoms is accomplished in the metastable state [9] with a lifetime of nearly 40 s. The number of metastable atoms produced in the RF discharge method is determined by the values of the RF power used for the excitation of the atoms and the pressure of the gas in the discharge tube. The RF electric field in the inductive coil generates a RF magnetic field in the discharge region which induces an electric field E in the discharge region.

The general principal of the RF excitation of a gaseous medium placed in the RF field can be explained by considering the RF field as an oscillating time varying electric field E (angular frequency, ω_{RF}) given by ,

$$E = E_0 \cos(\omega_{RF} t)\,. \tag{2.1}$$

Where E_o is the maximum amplitude of the electric field.

The Lorentz force F (magnitude) due to this RF field on a free electron (generated in the gas by cosmic rays or other sources of ionizing radiation) in the gaseous medium is given as $F = eE$ (the RF induced magnetic field being insignificant compare to the electrical field and hence ignored). The acceleration (a) of electron in this field is given as,

$$a = eE/m \;= eE_0 \cos(\omega_{RF} t)/m\,.$$

The average kinetic energy ($< E_K >$) gained by the electron in this oscillating electric field is estimated as [10]

$$< E_K > = \frac{1}{4m\omega_{RF}^2} e^2 E_0{}^2\,. \tag{2.2}$$

Once the energy gain by the electron is sufficient enough to ionize the gas, the discharge process is initiated due to the collision of the electrons with the neutral atoms and generates further electrons and ions. These free electrons further gain energy in the RF field and collide with the neutral atom to excite them into the metastable state. This process is a cascading in nature and can excite sufficient number of atoms in the metastable state until steady state number of atoms in the metastable state are achieved.

The Kr* atoms are mainly generated through the collision of electrons with the ground state atoms. The generation rate of Kr* atoms is proportional to σ_c, N_g *and* N_e, where σ_c is the electron impact excitation rate coefficient, N_g is the Krypton atom number density in the ground state and N_e is the electron density in the discharge. The metastable atom number density (at constant pressure) increases with the RF power mainly due to the increase in the electron density with the RF power as σ_c and N_g generally remain nearly unchanged at a given pressure. The saturation in the number density of the electrons with the RF power occurs at a given pressure of gas which leads to saturation of the number density of the Kr* atoms in the discharge tube. Also it is observed that the number density of the Kr* atoms first increases and then decreases with the pressure in the discharge tube for the constant RF power. The increase in the number density is due to the increase in the electron density at higher pressure values in the discharge tube. The production of the metastable atoms increases with increase in pressure due to more number of collisions of electrons with ground state atoms which increases with pressure. At higher pressure, the de-excitation of the metastable atoms also increases due to their collisions with the ground state atoms that lead to the slow decrease of Kr* density for higher pressures at a fixed value of RF power.

The commonly used method for producing metastable noble gas atoms is through RF discharge, but it is relatively inefficient but simple to implement, in which only a small fraction of gas atoms ($\sim 10^{-4}$) can be excited into the metastable energy state. The RF discharge plasma usually contains electrons, ions, ground state atoms and metastable state atoms. This plasma is routinely used as a source of metastable atoms. To form an atomic beam of the metastable atoms, the plasma in the discharge tube is allowed to flow from one end of the tube to the various connected chambers maintained at a lower pressure than the pressure in the discharge tube. In the following section, we present the development and characterization of the experimental setup consists of various vacuum chambers including MOT chamber. Various experimental parameters affecting the generation of the Kr* atoms in the discharge tube and their efficient transfer to the MOT chamber is also discussed. The experimental results on the generation of the metastable Krypton (Kr*) atomic beam from the RF-discharge plasma of Krypton (Kr) gas show that the presence of charged particles (such as Kr-ions and electrons) in the atomic beam is useful for producing higher number density of the Kr* atoms. The electrons and Kr-ions also produce Kr* atoms via electron-ion radiative recombination process. These results are useful for obtaining a higher number density of Kr* atoms in the atomic beam emanating from the discharge tube for atom cooling and trapping application. The characterization of the source of metastable Kr atoms produced using radio frequency (RF) excitation of Kr gas in a discharge tube is an important study for the development of the MOT setup. The generation of ^{84}Kr* atoms in the discharge tube was studied by varying the pressure and the RF power in the tube. The number density of ^{84}Kr* atoms was measured using laser absorption method. This optimization of the number density of ^{84}Kr* atoms is particularly useful for laser cooling and trapping of ^{84}Kr* atoms in the MOT.

A weak probe laser beam with scanning frequency (from extended cavity single mode semiconductor diode laser, DL 100L, TOPTICA, Germany) is passed through the discharge tube perpendicular to the tube axis. The $1/e^2$ radius of probe beam was ~ 0.7 mm and the linewidth of this laser was ~1 MHz at 811.5 nm wavelength. The linewidth of the probe laser is much smaller than the expected width of the transition, which is necessary for accurate measurement of the number density of the cold atoms by absorption probe method. A part of this laser beam was passed through a sealed Kr cell excited by the RF source to generate Doppler-free saturated absorption spectroscopy (SAS) signals for transitions from the Kr* atom. The metastable number density in the $5s[3/2]_2$ state is measured by observing the transmission signal (*V)* of the probe laser beam by scanning the probe laser frequency around $5s[3/2]_2 \rightarrow 5p[5/2]_3$ transition. Typical photodiode signal observed due to absorption of the probe beam is shown in Fig. 2.3, where V_{max} and V_{min} are the maximum and minimum values of the photodiode signals.

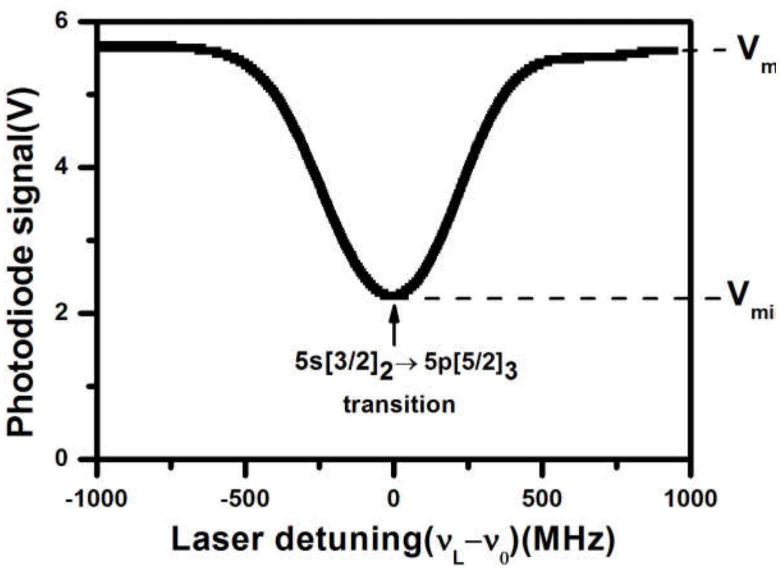

Fig. 2.3: Typical photodiode signal observed for Kr* atom number density measurements, where ν_L (= $\omega_L/2\pi$) and ν_0 (= $\omega_0/2\pi$) are the laser and atomic resonance frequencies respectively.

The transmitted intensity of the probe beam is given by

$$I(\omega, L) = I(\omega, 0)\exp[-n\sigma(\omega)L], \tag{2.3}$$

which can be written for resonance frequency ω_0 as,

$$\frac{I(\omega_0, L)}{I(\omega_0, 0)} = e^{-n\sigma(\omega_0)L} \tag{2.4}$$

where n and $\sigma(\omega)$ are the number density and the absorption cross section (1.7×10^{-11} cm^2) for a Doppler broadened profile respectively. Here L denotes the length of interaction region which is cross sectional diameter of the discharge region (~ 6 mm) in the discharge tube, ω denotes the probe laser frequency and $I(\omega,0)$ and $I(\omega,L)$ are the intensity values of the probe laser beam at the entrance and the exit of the discharge tube. Here, V_{min} *and* V_{max} can be approximated to be proportional to $I(\omega_0,0)$ and $I(\omega,L)$ respectively in the far off frequency range from the resonance frequency. This is because, at far off resonance, $I(\omega, L) \sim I(\omega_0,0)$.

Hence,

$$\frac{V_{\min}}{V_{\max}} = e^{-n\sigma(\omega_0)L}. \tag{2.5}$$

Using the value of $\sigma(\omega_0)$ for the measured Doppler broadened absorption profile and knowing L, we can find the number density as [10],

$$\text{Number density } (n) = \frac{\log_e\left[\frac{V_{\max}}{V_{\min}}\right]}{\sigma(\omega_0)L}. \tag{2.6}$$

The number density of Kr* atoms was measured in the discharge tube using probe absorption method for different values of the RF power. As shown in Fig. 2.4, the observed number density at pressure of ~3.5 mTorr, first increases from 2.0×10^9 cm^{-3} to 1.7×10^{10} cm^{-3} with the RF power increasing from 1.5 W to 4 W. At higher power (> 4W), the number density saturates with further increase in the RF power. At an increased pressure (~ 12 mTorr), the variation in the number density with the RF power was similar except the number density (~ 2.0×10^{11} cm^{-3}) of Kr* atoms was higher in the discharge tube. The saturation in the number density with the RF power was due to saturation in the electron number density in the discharge tube at a given pressure.

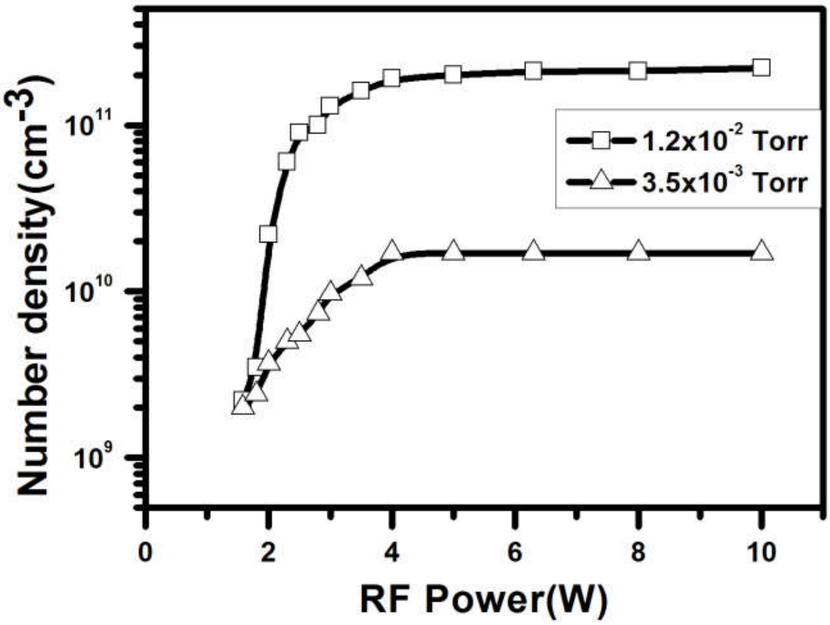

Fig. 2.4: Measured variation in the number density of $^{84}Kr^{*}$ with the RF power for two different values of pressure, 3.5×10^{-3} and 1.2×10^{-2} Torr in the discharge tube.

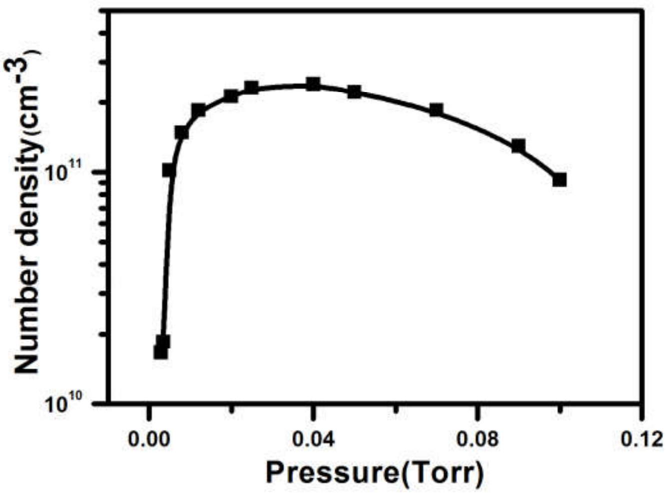

Fig. 2.5: Measured variation in $^{84}Kr^{*}$ atom number density with pressure in the discharge tube at 4 W of RF power.

It is known from the earlier work that Kr* atoms are mainly generated through collision of electrons with the ground state atoms. As observed (Fig. 2.5), the number density of the ^{84}Kr* atoms increases with the pressure till 40 mTorr and then decreases slowly with the pressure at higher pressure at a fixed value of the RF power. The increase in the the number density of the ^{84}Kr* atoms was due to increase in the electron density with increase in pressure in the discharge tube. The production of metastable atoms increases with increase in pressure due to more number of collisions of electrons with ground state atoms. At higher pressure, the de-excitation of metastable atoms also increases due to their collisions with ground state atoms [11].

2.4 Transfer of Kr* atoms

In order to transfer the metastable Kr atoms from the RF discharge tube to the MOT chamber, the maintaining of appropriate differential pressure in the various vacuum chambers was the main consideration. This was also necessary because the source chamber and the MOT chamber work at two significantly different pressure. The generation of Kr* atom in the discharge tube requires ~10^{-3} mTorrr pressure for obtaining the larger density of Kr* atoms, whereas the MOT chamber needs to be at lower pressure (10^{-8} mTorr) to reduce the background collision losses for the MOT cloud. Considering these requirement, various vacuum chambers for the experimental setup was designed accordingly.

2.4.1 Vacuum system for the experimental setup

The vacuum systems as shown in Fig. 1.4 consists of the gas inlet chamber (C_1) (~10^{-3} torr), the discharge tube, the analysis chamber (C_2) (~ 10^{-5} torr), a pumping chamber (C_3) (~ 10^{-7} torr), Zeeman slower (ZS) and the magneto-optical trap MOT chamber (~ 10^{-8} torr) in a steady condition with gas flow. The Krypton gas first flows into the source chamber and then in the RF discharge glass tube. Its flow rate can be controlled through a fine needle valve attached with the Kr gas cylinder. The glass tube has inner diameter 10 mm and length 150 mm in which RF discharge (frequency ~30 MHz) was created to excite the Kr atoms to the metastable energy state. The RF power was inductively coupled to Kr gas through a copper coil surrounding the glass tube. A stainless-steel tube of inner diameter 5 mm and length 50 mm has been used between the analysis chamber and pumping chamber to set the appropriate conductance between the chambers for obtaining the desired differential pressure. It also helps to collimate the atomic beam flowing towards analysis chamber. The various chambers were pumped using turbo-molecular pump (TMP) of appropriate capacity to maintain the suitable differential pressure throughout the setup.

In the vacuum system, the conduction of the various connecting tubes, degassing rate from the various chambers and the pumping speed of the turbo-molecular pumps used governs the ultimate pressure which can be obtained in the different chambers. Pumping speed (S_{pump}) is defined as the volume of gas removed from the system per unit time, measured at the inlet of the pump (liters/sec). Conductance (C) is the ease of the flow of gas through a vacuum line. It is defined as the amount of gas, which flow through line per unit time. Conductance for various shapes such as tube (C_{tube}), elbow (C_{elbow}) and aperture ($C_{aperture}$) is estimated by the following expressions,

$$C_{tube} = 3.81 D^3 \left(\frac{T}{M} \right)^{\frac{1}{2}} / L \tag{2.7a}$$

$$C_{elbow} = 3.81 D^3 \left(\frac{T}{M} \right)^{\frac{1}{2}} / (L_1 + L_2) \tag{2.7b}$$

$$C_{aperture} = 3.64 A \left(\frac{T}{M} \right)^{\frac{1}{2}}, \tag{2.7c}$$

where D is the diameter of the vacuum line in cm, T is the temperature in Kelvin, M is the average mass of the gas in amu (~ 28.5), A is the area of the aperture in cm^2 and L_1, L_2 are the lengths of the tubes.

Effective pumping speed (S_{eff}) of the pump resulting after connecting tube of conduction C is given as

$$\frac{1}{S_{eff}} = \frac{1}{S_{pump}} + \frac{1}{C}. \qquad (2.8)$$

The ultimate pressure (P) in the chamber is given as, $P = Q / S_{eff}$, where, (Q) is the throughput (torr x litres/sec) and is defined as the product of the volume of gas flowing across any plane in the system per unit time and the pressure in that plane. It is difficult to calculate the expected pressure in the chamber during the Kr gas flow condition. While under no external gas flow condition, the ultimate pressure calculated using throughput and effective pumping speed does not differ much from the measured values.

Another important relation for maintaining the differential pressure between two pipes is governed by the following relation,

$$C(P_2-P_1) = S\,P_1$$

and

$$CP_2 = SP_1 \text{ for } P_1 << P_2. \qquad (2.9)$$

Where P_1 and P_2 are the required pressure in the two chambers connected by a tube of conduction C and using pump of pumping speed S.

2.4.2 Effect of stray magnetic field on transfer of Kr* atoms

In our experimental setup, it was observed that the Kr ions after RF-discharge tube did not propagate in the same direction as that of the neutral Kr atoms. It was concluded from the observation that the purple color beam (of Kr-ions) emanating from the discharge tube was not collinearly aligned with the tube axis along the horizontal direction (i.e. direction of propagation of atomic beam), and was measured to be deviated by ~ 2 degree angle in the downward direction as shown in Fig. 2.6. During the experimentation, it was realized that the purple color ions beam was deflected because of the stray magnetic field (including earth magnetic field of ~ 250 mG) present near the setup and its effect on the setup was investigated. The effect of this stray magnetic field (~ 1G) on the setup can be nullified either using a bias magnetic field or suitably shielding the setup using a high μ- metal sheet. The purple color ions beam was accurately aligned along the atomic beam direction by a magnetic field applied using a current carrying coil (called alignment coil) placed outside the chamber. This coil was positioned outside the pumping chamber (Fig. 2.6(a)) such that its axis (in the horizontal direction) crossed the atomic beam axis at ~ 90 degree angle at a distance of s = 5 cm from the exit of the discharge tube. This coil provided a variable magnetic field which reached the value ~ 1 Gauss at the beam axis for current of ~ 2 A in the coil. When the current in the alignment coil was increased, the purple color beam of the ions started changing its direction as shown schematically in figure 2.6(b) (crosses show that applied magnetic field direction was perpendicular to the plane of paper in the inward direction).

In order to accurately align the purple color ions beam along the atomic beam direction, the required applied magnetic field value was ~ 1 Gauss. Figure 2.7 shows the observed variation in the deviation angle (θ) of the ions (measured with respect to the initial direction of the ions at zero applied magnetic field) with the applied magnetic field due to this coil.

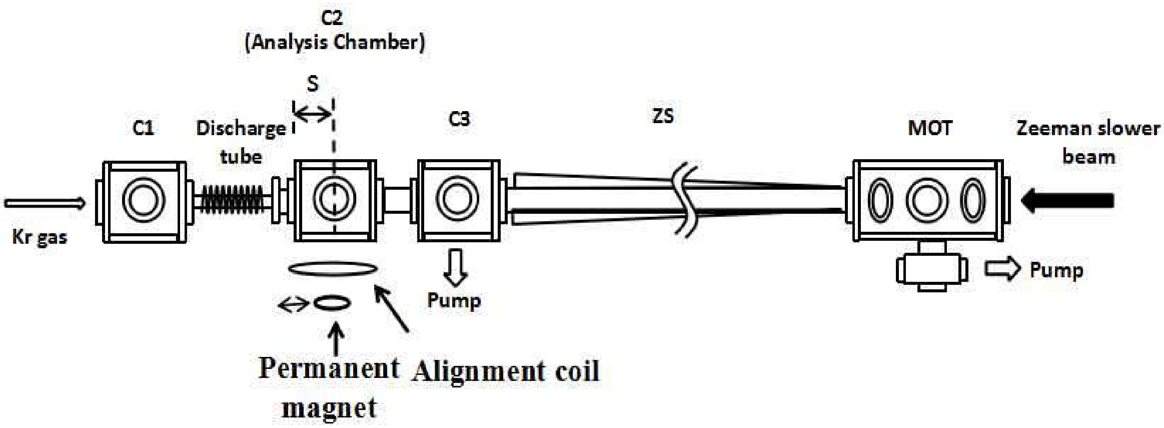

(a)

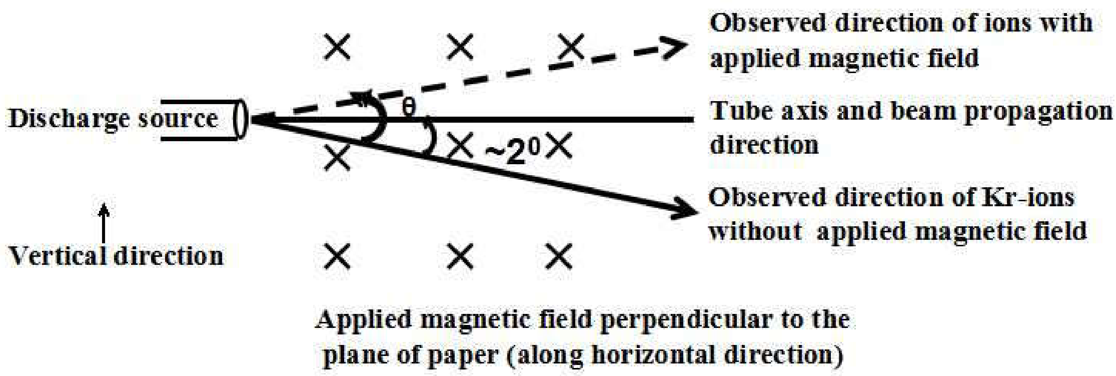

(b)

Fig. 2.6: (a) Schematic of the experimental setup, (b) The schematic of the observed deviation of Kr-ions from the atomic beam direction (with and without applied magnetic field).

The number density of ^{84}Kr* atoms in the beam was measured at the centre of the trapping chamber. For this, a laser beam of appropriate frequency was applied perpendicular to the atomic beam (to minimize the Doppler broadening) at the MOT chamber. The density of ^{84}Kr* atoms was estimated by collecting laser induced fluorescence from the Kr* atoms on a calibrated sensitive photodiode. It was observed that when the direction of the ion beam was brought closer to the direction of the atomic beam by applying magnetic field, the number density of the ^{84}Kr* atoms in the trapping chamber was increased.

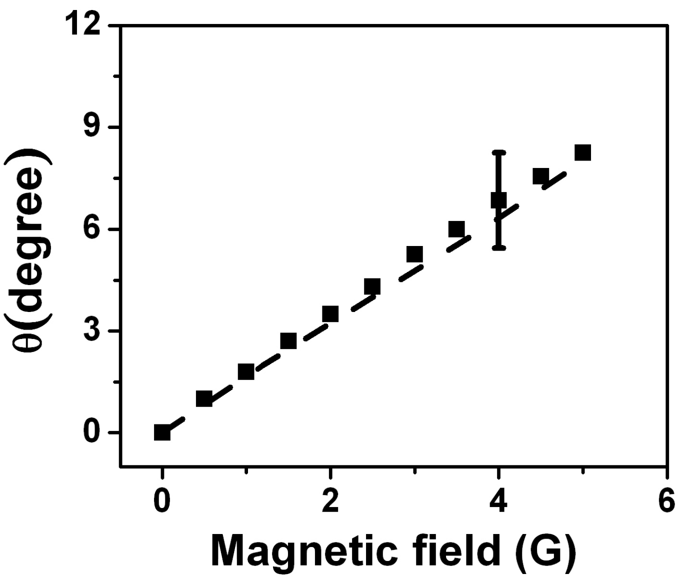

Fig. 2.7: Observed variation in deviation angle (θ) of Kr-ions with the applied magnetic field. The dashed line shows the calculated deviation angle for Kr ion with applied magnetic field.

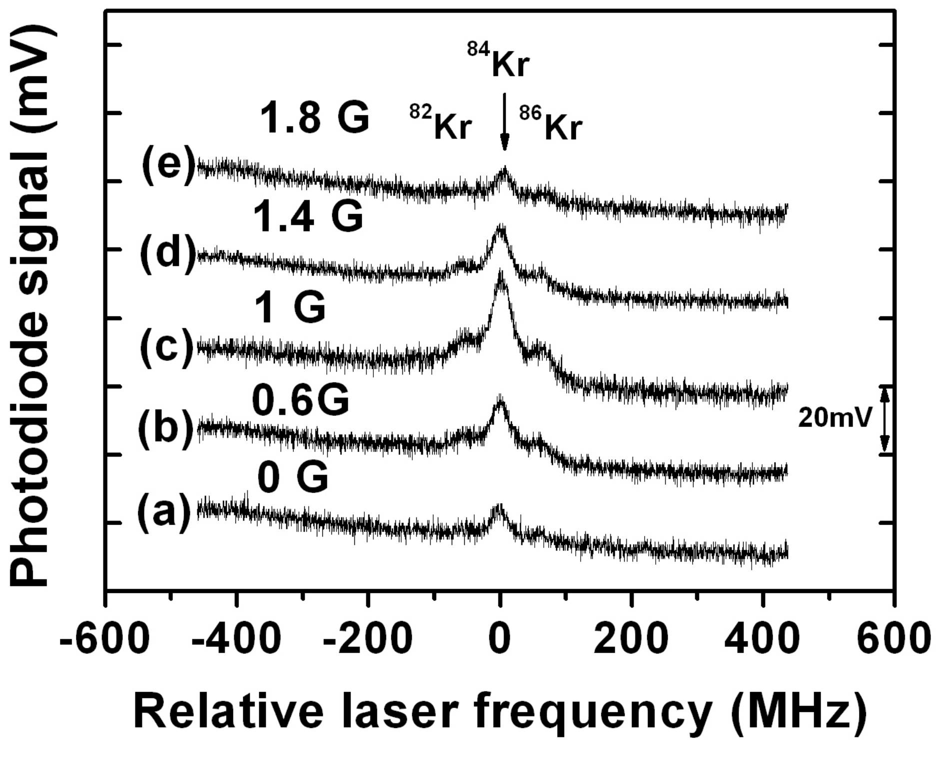

Fig. 2.8: Observed photodiode signals for measuring fluorescence from the MOT chamber for different values of the applied magnetic field due to alignment coil. In each trace, the three Doppler-free peaks correspond to three isotopes $^{82}Kr^*$, $^{84}Kr^*$, and $^{86}Kr^*$ respectively in

metastable state. The estimated number density of metastable $^{84}Kr^*$ atoms for curves (a) to (e) are respectively 1.5×10^6 cm^{-3}, 2.3×10^6 cm^{-3}, 3.0×10^6 cm^{-3}, 2.3×10^6 cm^{-3} and 1.5×10^6 cm^{-3}.

Figure 2.8 shows the fluorescence signals recorded for estimation of Kr* atoms number density in the MOT chamber for different values of applied magnetic field due to the alignment coil. In this figure, curves (a)-(e) show the detected fluorescence signal variation with the probe laser frequency for different values of the applied magnetic field. These signals were detected by a photodiode and recorded using an oscilloscope. In the Fig. 2.8, recorded data for signals were given appropriate shifts along the ordinate axis to plot the signals without overlap. It is evident from the Fig. 2.8 that the number density of Kr* atoms in the trapping chamber is changing with the applied magnetic field. Figure 2.9 shows the measured variation of the number density of $^{84}Kr^*$ atoms in the trapping chamber with the magnitude of applied magnetic field of the alignment coil at the atomic beam axis. As shown in the Fig. 2.9, the number density initially increased with the magnetic field and reached the maximum value for ~ 1 Gauss of applied field. At this value of field, it was observed that the direction of colored beam of Kr-ions was closely matching with the direction of atomic beam. At further higher values of magnetic field, the number density started decreasing with increasing applied magnetic field (Fig. 2.9). At these values of magnetic field, the ions path gets again misaligned with the beam axis, with ions direction now making an angle in the opposite direction from that of the atomic beam axis. Although, it could be interesting to measure number density of ions in the beam and compare it with that of metastable (or neutral) atoms but there was no setup ready for this study. Nevertheless, effect of ions number density on the production of metastable atoms in the plume beam could be observed by measuring the enhancement in the number of Kr* atoms reaching to the MOT chamber after alignment of direction of ions.

In the RF excited plasma, electron-ion radiative recombination represented by two body interaction process $Kr^{+}+e^{-} \rightarrow Kr^{*}+h\nu$ (where e^{-} and $h\nu$ denote low energy electron and photon energy respectively) seems contributing significantly to the production of Kr* atoms. Another two body process such as dissociative recombination process [12] represented by $Kr_2^{+}+e^{-} \rightarrow Kr^{*}+Kr$ is unlikely to contribute significantly to the production of Kr* atoms due to low pressure in the discharge tube. The higher order recombination process, e. g. three body recombination involving one ion and two electrons, requires a high number density (~ 10^{12} cm^{-3}) of ions and electrons. Thus, this process is also ruled out to contribute significantly to the production of Kr* atoms in the Kr*-MOT setup.

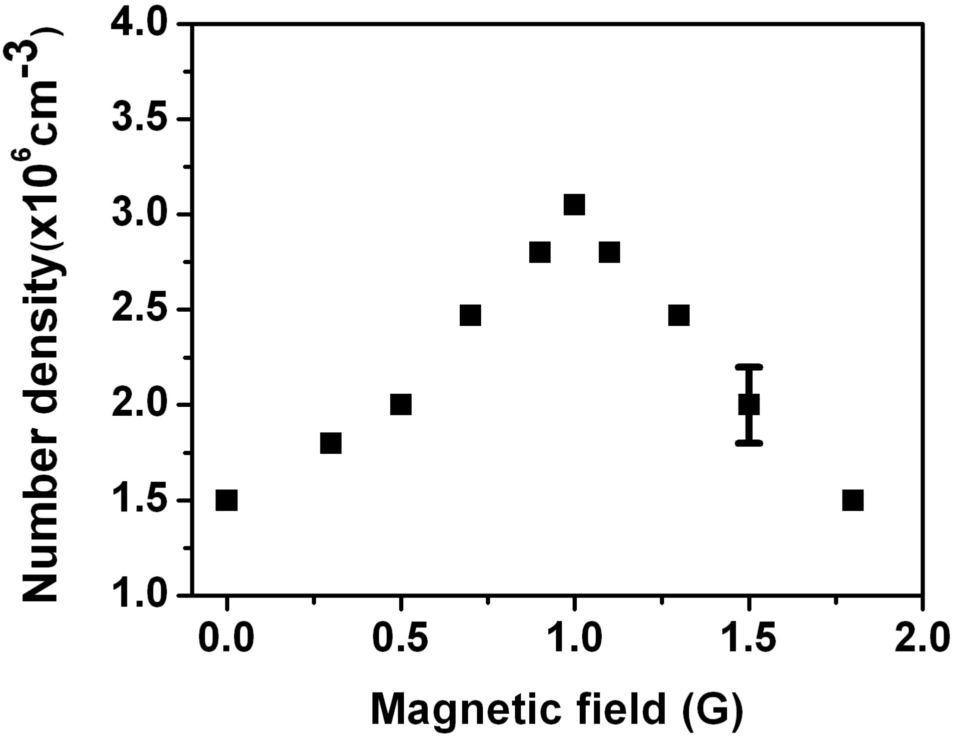

Fig. 2.9: Variation in measured number density of $^{84}Kr^{*}$ in the MOT chamber with magnetic field due to alignment coil. The characteristic error bar determined from scatter in the values obtained in repeated measurements is shown for one data point.

In the RF discharge, which was to produce Kr* atoms, ions can acquire energy upto ~ 40 meV whereas electrons can acquire energy typically in range of ~ 10 eV. Due to stray magnetic field (~ 1 Gauss) surrounding the setup, electrons having energy lower than 2 eV in the distribution are expected to survive in the analysis chamber (C2) as the radius of curvature of ~5 cm (at ~ 1 Gauss field and 2 eV energy) remains smaller than the cross-section size of the analysis chamber (~ 10 cm). Thus, in presence of the stray magnetic field of ~ 1G, only low energy electrons (energy < 2 eV) corresponding to radius of curvature < 5 cm will survive in the analysis chamber. These low energy electrons will interact with the deviated Kr-ions beam and result in electron-ion recombination. Electrons having energy higher than 2 eV will be lost as they collide with the chamber walls due to larger radius of curvature. On the other hand, Kr-ions (energy ~ 40 meV) have relatively large radius of curvature (~ 3 m) in presence of the stray magnetic field of ~ 1 Gauss. Hence, ions will show a small deflection from the beam axis, which was ~ 2 degree over the interaction path length of ~10 cm in the pumping chamber. When an external magnetic field was applied by using a current carrying coil (alignment coil) to nullify the stray magnetic field, electrons and ions get aligned along the atomic beam direction. This results in increase in the number density of electrons and ions in the atomic beam and consequently increase in number of recombination events to produce metastable Krypton (Kr*) atoms in the atomic beam path. Thus applied magnetic field can result in the enhancement in number of metastable Krypton (Kr*) atoms in the atomic beam.

It was noted that after alignment of ions along atomic beam direction, the purple color ion beam remains visible only upto 10-15 cm distance from the exit end of the discharge tube. To find the actual distance from discharge tube over which electron-ion recombination process effectively contributes to the production of Kr* atoms, following measurements were performed.

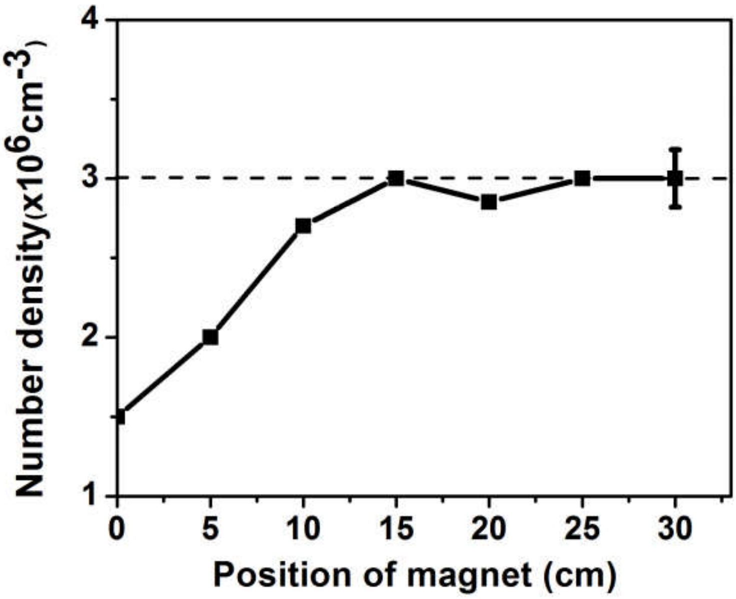

Fig. 2.10: Variation in ^{84}Kr* number density in the MOT chamber with position of permanent magnet with respect to exit of the RF-discharge tube. The horizontal dotted line shows the number density in absence of permanent magnet for the optimum value of field (~ 1 Gauss) due to alignment coil. The error bar shown for one data point was determined from the scatter in the values obtained in the repeated measurements. The error bars represents the deviation, in both positive and negative directions, from the average value. The error bar was prepared for 10 repetitions of a single observation. The error bar for other data points have also been calculated and found to be of the similar order and therefore error bar on one data point has only been shown. The variation in repeated observations is due to statistical variations in the measurement. We do not expect any significant systematic shift in these data.

First, the current in the alignment coil is set to obtain maximum number density of Kr* atoms in the trapping chamber as per data shown in Fig. 2.9. Then the permanent magnet was kept outside the TC chamber with magnetic field (~1 Gauss at atomic beam axis) parallel to that of the alignment coil. The field due to this magnet destroyed the alignment of ions along the atomic beam axis and resulted in decrease in the number density in the trapping chamber. As the distance of this magnet from discharge tube exit was increased along the atomic beam direction, the number density of $^{84}Kr^*$ atoms in the trapping chamber started increasing with distance and reached to the maximum value at distance of ~ 15 cm (refer Fig. 2.6 (a)) and remained nearly unchanged beyond this distance (Fig. 2.10). From the figure, it can be understood that when magnet was positioned closer to the discharge tube, the overlap of ions with atomic beam was for a shorter length. This resulted in lower number of $^{84}Kr^*$ atoms produced (via electron-ion recombination process) and accumulated in the atomic beam. As the distance of magnet was increased, the overlap of ions beam with atomic beam was increased, which resulted in increase in the number density of $^{84}Kr^*$ atoms due to larger contribution of electron-ion recombination process for production of $^{84}Kr^*$ atoms in the beam. Nearly unchanged number density after the distance of ~ 15 cm of magnet from the discharge tube indicates that electron-ion recombination process becomes weak after this distance. This may be due to insufficient number density of ions in the beam after a distance of ~ 15 cm of beam propagation [13].

2.5 Zeeman slower

The average speed of atoms in the Kr* atomic beam is around 300 m/s which is much higher than the capture speed (typically ~ 25 m/s) of a MOT. Therefore, it is necessary to reduce the speed of atoms before they reach the MOT chamber. This was implemented by using a Zeeman slower. In a Zeeman slower, a spatially varying magnetic field and a red-detuned counter propagating (to atomic beam direction) laser beam (referred as Zeeman slower laser beam) was used to reduce the speed of atoms in the atomic beam. The spatially varying magnetic field in the Zeeman slower results in spatially varying shift in the energy levels of cooling transitions. This compensates for varying Doppler shift of Zeeman slower laser beam frequency during the slowing of atoms in the atomic beam. This is the most effective and commonly used method to slow down a beam of atoms from initial speed of hundreds of m/s to few tens of m/s.

2.5.1 Design of a Zeeman slower

There are three types of Zeeman slower used, increasing magnetic field slower, decreasing magnetic field slower and the Zeeman slower that involves both decreasing and increasing magnetic fields. In an increasing field Zeeman slower, the atoms with initial higher speed encounter a very low magnetic field so that the slower laser beam is required to be detuned by the Doppler shift of the atom with maximum speed. The disadvantage of an increasing field slower is that the magnetic field has a large value at the far end of the slower and close to the MOT, which may interfere with the magnetic field of the MOT. In a decreasing field slower, the atoms initially encounter the high field and then low field before ejecting out of the slower. The MOT placed at the end of the slower is therefore less perturbed by the field of the Zeeman slower. For the decreasing field slower, a σ^+ circularly polarized light beam is used for cooling whereas σ^- circularly polarized light beam is used for slowing atoms when increasing field type slower is used.

In presence of a magnetic field B, an atom undergoes a Zeeman shift of its energy levels given by,

$$\Delta E = -g_J \mu_B M_J B, \tag{2.10}$$

where, $\mu_B = e\hbar / 2m$ is the Bohr magneton and g_J is the Lande g factor and M_J is the magnetic substate.

The Zeeman slower used in the setup was decreasing field Zeeman slower. In this Zeeman slower, the magnetic field variation along the atomic beam direction is kept such that the Zeeman shifted atomic transition frequency is equal to the Doppler shifted frequency of the counter propagating slowing laser beam. This is expressed as $\omega_0 + (\mu_B B_Z/\hbar) = \omega_L + kv$, where ω_0 is the atomic resonance frequency in absence of magnetic field, ω_L is the laser frequency, μ_B is Bohr magneton, $\hbar$ = reduced Planck's constant, B_Z is the magnetic field at a distance of z from the edge of the Zeeman slower as shown in Fig. 2.11 (a), k is the magnitude of wavevector and v is the speed of the atom interacting with the Zeeman slower laser beam moving opposite to the laser beam. The effective slowing laser beam detuning from the atomic transition is defined as,

$$\Delta = (\omega_L - \omega_0) + kv - \mu_B B_z / \hbar \,. \tag{2.11}$$

The deceleration *a(z, r)* of the atom in the Zeeman slower at the longitudinal distance z and transverse distance r is given as,

$$F(z,r) = ma(z,r) = \hbar k \frac{\Gamma}{2} \frac{I_{zs}(r)/I_s}{1 + I_{zs}(r) + 4(\Delta/\Gamma)^2} \,. \tag{2.12}$$

Here, $F(z, r)$ is the scattering force, $k = 2\pi/\lambda$, where λ is the wavelength, Γ (= 2π x 5.56 MHz) is the linewidth, I_s is the saturation intensity (for ^{84}Kr* atom, I_s = 1.36 mW/cm^2) and $I_{zs}(r) = I_0 \exp(-2r^2/\rho_0^2)$, is the transverse intensity profile of the Zeeman slower laser beam. Here r and ρ_0 denote the transverse position and the beam spot size (1/e^2 radius) respectively. This deceleration governs the variation in the longitudinal velocity with distance z as,

$$v(z+\delta z)^2 = v(z)^2 - 2a(z,r)\delta z \,, \tag{2.13}$$

where $v(z)$ and $v(z+\delta z)$ are the velocities at distances z and $z+\delta z$ in the Zeeman slower. While designing the Zeeman slower, the variation of B_z with z is adjusted in such a way to keep detuning Δ minimum to achieve maximum deceleration throughout the length of the Zeeman slower.

An extraction coil is also required to be used with the Zeeman slower. The role of the extraction coil used with the Zeeman slower is to tailor the B_z field in such a way that the longitudinal velocity of atoms reaches to a low velocity outside the Zeeman slower in the

MOT chamber. This facilitates atoms to reach the capture volume of the MOT and get trapped in the MOT. The currents in the Zeeman slower and the extraction coils were optimized independently to get the maximum flux of slowed atoms in the MOT chamber.

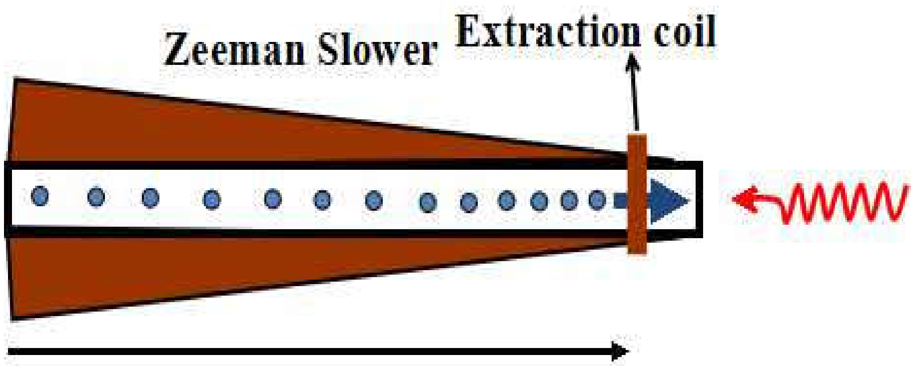

(a)

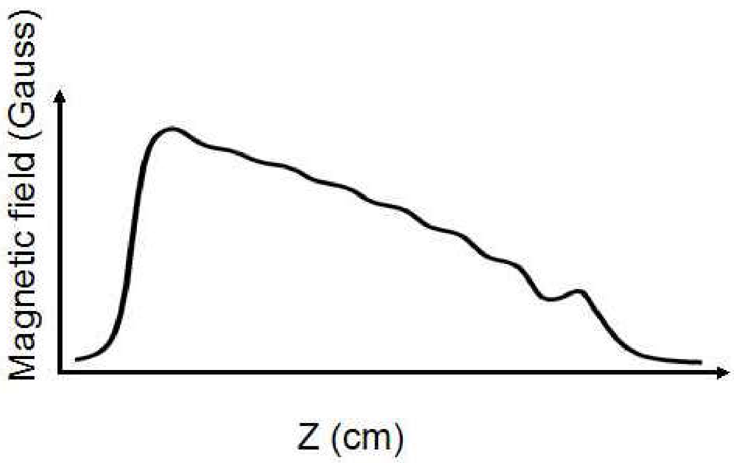

(b)

Fig. 2.11: (a) Schematic of the Zeeman slower and (b) Typical magnetic field profile along the length of the Zeeman slower.

The schematic and the magnetic field variation in the Zeeman slower is as shown in the Fig. 2.11. The magnetic field along the direction of atomic beam direction was designed to provide an effective cooling of the longitudinal velocity of an atomic beam. The Zeeman shifted atomic transition frequency need to be equal to the Doppler shifted frequency of counter propagating laser beam throughout the Zeeman slower length.

2.5.2 Measurement on a Zeeman slower

In order to characterize a Zeeman slower, one needs to observe the magnetic field along the length of Zeeman slower and the final velocity of the atom at the exit of the Zeeman slower and these parameters are required to be matched with the theoretically simulated results. Fig. 2.12 shows the photograph of the inhouse developed Zeeman slower and Fig. 2.13 (a) and (b) show the magnetic field profile and the speed of the atom along the length of Zeeman slower for the parameters mentioned in the figure captions. Experimental results are well matched with the theoretically calculated results.

Fig. 2.12: Photograph of in-house developed Zeeman sower.

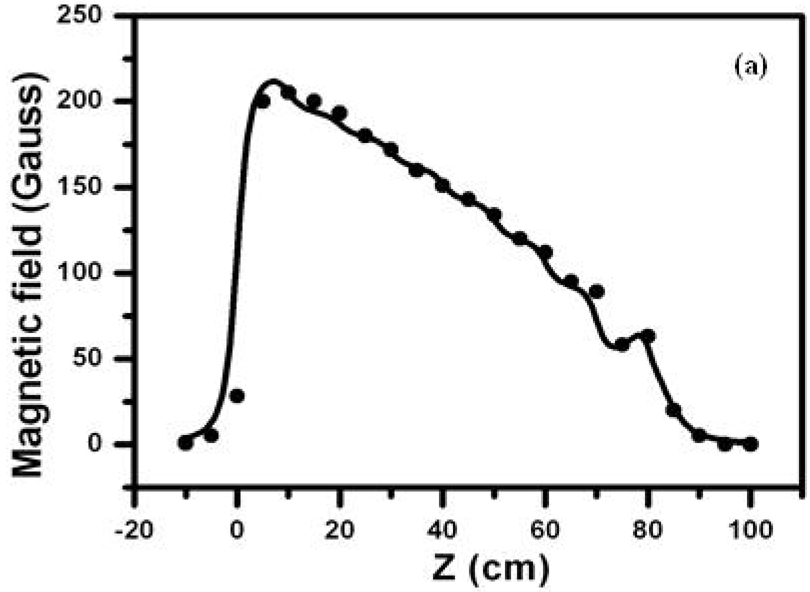

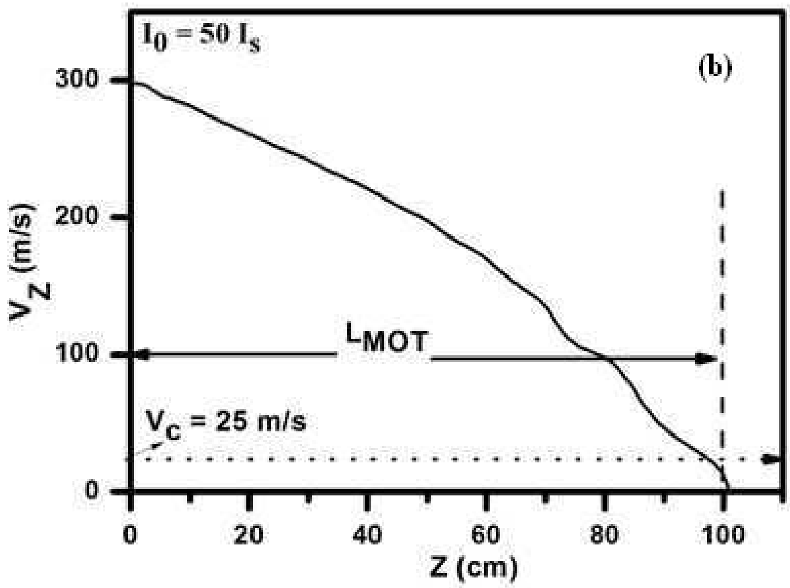

Fig. 2.13: (a) The dots represent the measured magnetic field of Zeeman slower (without extraction coil) for current of 1.3 A. The continuous curves show simulated magnetic field for current in Zeeman slower coil and extraction coils as 1.3 A and 3.5 A respectively. (b) The simulated variation in speed of an atom during its motion in the Zeeman slower for currents of 1.3 A and 3.5 A respectively in Zeeman slower coil and extraction coil.

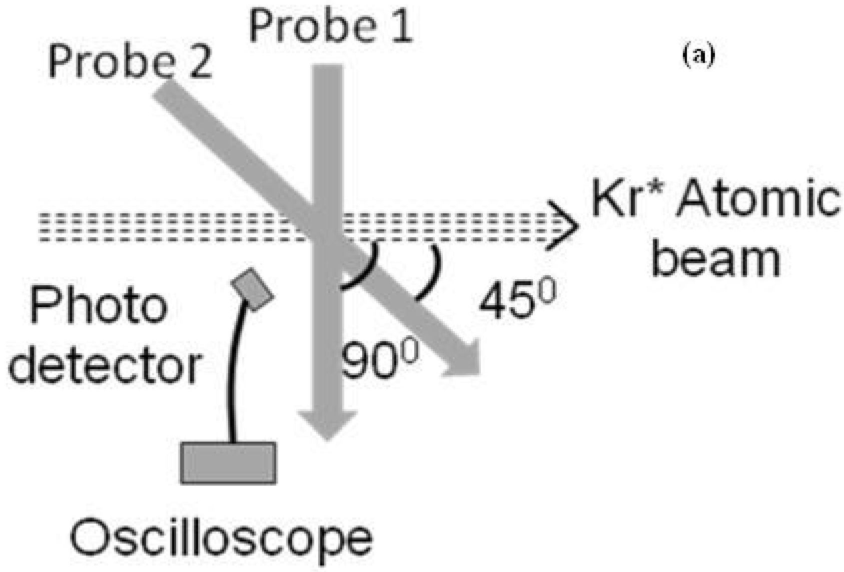

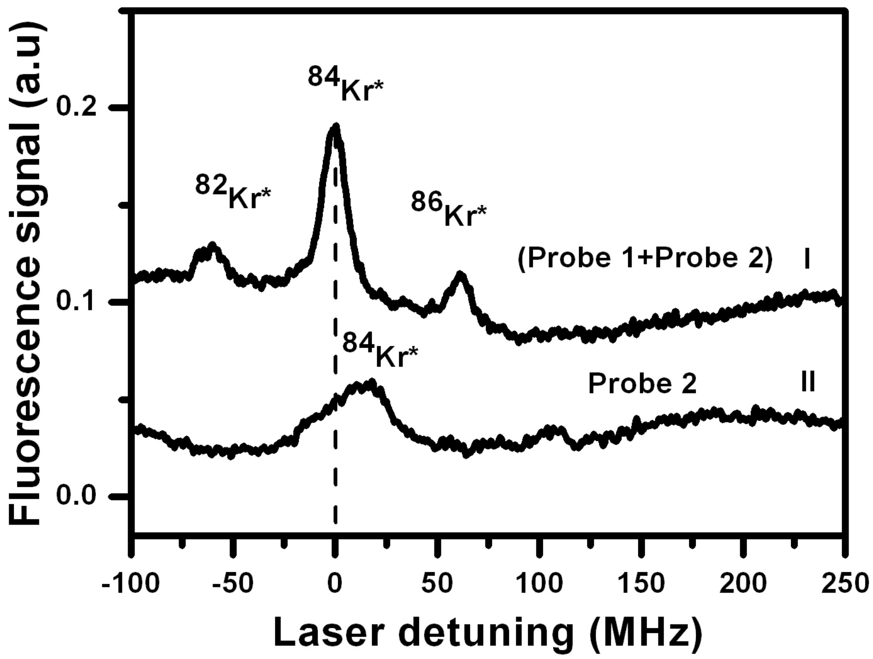

Fig. 2.14: (a) Schematic of experimental setup for measurement of velocity of atomic beam; (b) Typical fluorescence signals due to two probe laser beams (probe 1 and probe 2) passing simultaneously at 90^0 and 45^0 (curve I). The curve II is due to the probe at 45^0 only shows the velocity profile of slowed atomic beam (^{84}Kr*).

Fig. 2.14 (a) shows the schematic of the experimental setup used to measure the speed of ^{84}Kr* atoms by generating fluorescence signal from atomic beam obtained due to excitation from probe laser beams (at 90^0 and 45^0) derived from the same laser. Figure 2.14 (b) shows the fluorescence signal observed in the trap chamber. Curve I shows the fluorescence signal from atomic beam due to both the incident probe laser beams at 90^0 and 45^0 simultaneously recorded on photodiode and used for frequency reference. The curve II is due to the probe at 45^0 only and this curve shows the velocity profile of the slowed atomic beam (^{84}Kr*) after the operation of Zeeman slower. The peak in the curve II correspond to the velocity of atoms of ~ 15 m/s and the full width at half maxima correspond to ~30 m/s. This width is mainly due to spatial inhomogeneity of the laser radiation intensity and magnetic field of the Zeeman slower [14]. The atoms with velocity of ~ 15 m/s can now be trapped in the MOT.

After reducing the longitudinal velocity of the atomic beam in the Zeeman slower, atoms are further cooled and trapped in the MOT.

2.6 Conclusion

In conclusion, in this chapter, the work related to the generation and transfer of Kr* atoms has been described. First, we have optimized the production of the Kr* atoms in the discharge tube and their transfer to the MOT chamber. It was shown that by applying an external magnetic field, the loss of Kr-ions due to stray magnetic field in an atomic beam can be reduced, and Kr* number density in the beam can be increased due to increased production of Kr* atoms via electron-ion radiative recombination process. Such magnetic field assisted enhancement in Kr* number density in the atomic beam is useful to increase the loading rate of a MOT for Kr* atoms. The working principle, concept of designing of the Zeeman slower, its fabrication and testing was also discussed in the chapter.

References:

1. C. Y. Chen, Y. M. Li, K. Bailey, T. P. O' Connor, L. Young and Z . -T. Lu, Science **286,** 1139 (1999).
2. C. –F. Cheng, W. Jiang, G. –M. Yang, Y. –R. Sun, H. Pan, Y. Gao, A. –W Liu and S. –M Hu, Rev. Sci. Instrum. **81,** 123106 (2010).
3. T. W. Riddle, M. Onellion, F. B. Dunning and G. K. Walters, Rev. Sci. Instrum. **52**, 797 (1981).
4. L. Young, D Yang1 and R W Dunford, J. Phys. B:. **35** 2985 (2002).
5. W. Rooijakkers , W. Hogervorst and W. Vassen, Opt. Commun. **123**, 321 (1996).
6. C. Y. Chen, K. Bailey, Y. M. Li, T. P. O'Connor, Z. -T Lu, X. Du, L. Young and G. Winker, Rev. Sci. Instrum. **72**, 271 (2001).
7. Y. Ding, K. Bailey, A. M. Davis, S. –M. Hu, Z. –T. Lu and T. P. O'Connor, Rev. Sci. Instrum. **77**, 126105 (2006).
8. Giulio Racah, Phy. Rev. **61**, 537 (1942).
9. Fujio Shimizu, Kazuko Shimizu and Hiroshi Takuma, Jap. J. Appl. Phys. **26,** L1847 (1987).
10. Annemie Bogaerts, Erik Neyts, Renaat Gijbels and Joost van der Mullen, Spectrochimica Acta Part B **57** 609 (2002)
11. S. Singh, V. B. Tiwari, S. R. Mishra and H. S. Rawat, "Characterization of RF discharge produced metastable Kr atoms", Abstract book of DAE-BRNS National Laser Symposium (NLS- 21), Mumbai, Feb. 6-9, 725(2013).
12. M A Biondi, Phys. Rev. **129**, 1181(1963) .
13. S. Singh, Vivek Singh, V. B. Tiwari, S. R. Mishra and H. S. Rawat, Indian Journal of Pure and Applied Physics **51**, 230 (2013).
14. P. N. Melentiev, P. A. Borisov and P. A. Balykin, J. Exp. Theo. Phy. **98**, 667(2004).

Chapter 3

Development and characterization of Kr* Magneto-optical trap setup

3.1 Introduction

The Kr atoms in the metastable state (Kr*) are produced using RF excitation mechanism and these atoms were generated in the discharge tube. The discharge tube in the setup was kept relatively at higher pressure compare to the MOT chamber. The Kr* atoms generated in the discharge tube move towards the MOT chamber due to the differential pressure between the discharge tube and the MOT chamber. The Kr atoms were laser cooled in the metastable state by using a laser of wavelength ~ 811.5 nm to excite the atoms from the $4p^5 5s[3/2]_2$ to $4p^5 5p[5/2]_3$ closed transition. For this, a reference signal is necessary for locking of the cooling laser frequency at the above cooling transition. The Doppler-free saturated absorption spectroscopy (SAS) is a widely used technique to generate such a reference signal [1]. The initial longitudinal cooling of metastable atoms needs to be performed in a Zeeman slower so that the atoms speed is brought lower than the capture speed of the MOT. The laser cooled atoms in the MOT need to be characterized for the number and the temperature of the cooled atoms before proceeding for further studies on these atoms. In this chapter, the above mentioned steps, from the generation of metastable atoms to the characterization of cold atoms in MOT, are discussed in the context of the Kr*-MOT setup. During the development of the setup, a new frequency stabilization scheme based on the atomic beam fluorescence has also been studied. The locking of cooling laser using this technique provides wider tunability and firm locking of the cooling laser beam compared to that of the locked laser using SAS technique. This is also discussed in this chapter.

3.2 Laser systems

Laser atom cooling and trapping of Kr atoms required several beams with narrow linewidth and precise frequency control. The cooling of even isotopes of Kr atoms requires laser beams for the Zeeman slowing of the atomic beam, cooling and trapping of atoms in the MOT and characterization of the cold atomic cloud in the MOT at suitable powers and frequencies.

Three extended cavity diode laser (ECDL) systems at wavelength of ~811 nm and linewidth of ~ 1 MHz have been used during the development and experiments using the Kr*-MOT. These ECDL systems are very compact and widely frequency tunable [2–5]. In these laser system, first order diffracted beam from the diffraction grating is coupled back to the laser diode. The diffraction grating acts as wavelength selective element in the external resonator of ECDL. The grating is used either in Littrow or Littman-Metcalf configuration. In Littrow configuration, the grating is aligned such that the first order diffraction from the grating is coupled directly back into the laser while the output is obtained from the zeroth-order. The wavelength tunability is achieved by rotating the diffraction grating. While in Littman-Metcalf configuration, output from the diode laser incident on a grating at a grazing angle. The first order diffracted beam goes to an additional mirror, which then reflects the beam back to the grating and then into the diode laser. The wavelength tunability is achieved by varying the mirror angle. Hence, the zeroth order output beam remains fixed as the wavelength is changed. Both of these configurations have their merits and demerits. But the most common configuration used in ECDL is Littrow configuration due to its advantage of large output power. The three laser systems in Littrow configuration used were from TOPTICA, Germany (Model: TA PRO with power ~ 1W, DL 100 with power ~ 150 mW and DL 100 with power ~ 100 mW).

These ECDL system consists of a laser diode with collimating optics, mounted on a conducting base with heat sink. The temperature of the base plate and diode laser mount in these systems is controlled by using a suitable electronics and thermoelectric coolers. This helps in the passive stabilization of the output frequency of the diode laser. The grating is mounted on a mount with a piezoelectric transducer (PZT) and its controlling electronics. This make it possible to course tune and fine tune the frequency of the laser beam. The laser system is usually placed on the vibration isolation table to isolate the system from various spurious noise in the surrounding. The cavity length and hence laser frequency changes over the time due to the mechanical vibrations, fluctuations in the diode injection current. Hence, active frequency stabilization of these laser systems are also required.

For active frequency stabilization, a negative feedback loop is used to stabilize the frequency of ECDL. The laser frequency is actively compared with a reference frequency signal obtained using saturated absorption spectroscopy. A reference DC voltage corresponding to the desired frequency on the spectroscopy signal (corresponds to desired frequency) is fed to the proportional-integral-differential (PID) controller. Usually, saturated absorption spectroscopy is performed in a glass cell of appropriate atomic vapor or gas to get such a reference signal for the frequency locking of the cooling laser. The difference between a set reference voltage and the signal voltage is known as error voltage which is proportional to the fluctuations of laser frequency from the set frequency. The function of PID controller is to minimize the error voltage by negative feedback and hence keep the output frequency stable.

3.3 Frequency stabilization of lasers

The active frequency stabilization of the laser system is an integral part of any magneto-optical trap setup. In order to lock the laser on the desired frequency, one needs to generate a reference signal corresponding to the atomic resonance that is usually done using cell of same atomic species. The reference signal with steep slope and improved signal to noise ratio is required to have the better stability of the laser system locked using this reference. The active frequency stabilization of the ECDL system was performed by providing suitable feedback to the laser diode using proportion-integral-differential (PID) circuitry. The reference signal used for generation of the error signal from the PID control loop is generated by saturated absorption spectroscopy (SAS) or from the atomic beam fluorescence spectroscopy (ABFS). During this work, the laser frequency stabilization using SAS and ABFS has been performed which are explained in the subsequent section below.

3.3.1 Saturated absorption spectroscopy (SAS)

The Doppler-free saturated absorption spectroscopy (SAS) is one of the most commonly used techniques to generate the reference signal for the frequency locking of the laser system used for obtaining the cooling laser [6]. The SAS signal for locking the laser system for laser cooling of Kr atoms was derived using the RF excited discharge from a glass cell filled with Kr gas at a pressure of few hundreds of mTorr. The SAS signal was generated by measuring the absorption of a weak probe laser beam in the presence of a counter-propagating strong pump laser beam in a Kr discharge. The rising or falling part of the SAS signal was used for side-locking of the laser frequency near the peak of the atomic transition [2]. In the side-locking, the lock stability of the laser depends significantly on the slope of the SAS signal at the locking position. The steeper slope gives the better frequency stability. The fluctuations in the laser frequency can be monitored by measuring the error signal, which is the difference between a set reference voltage and the signal voltage. This error signal can be generated by a proportional-integral-differential (PID) controller used for locking the laser frequency. In order to ensure the repeatability of same locking point (or detuning), the position of the absorption signal are calibrated routinely with respect to the other nearby peaks. Saturated absorption spectroscopy (SAS) is also well known technique for studying fine and hyperfine spectra of an atom, where population change in an energy level is monitored by a weak probe beam in the presence of a strong pump beam.

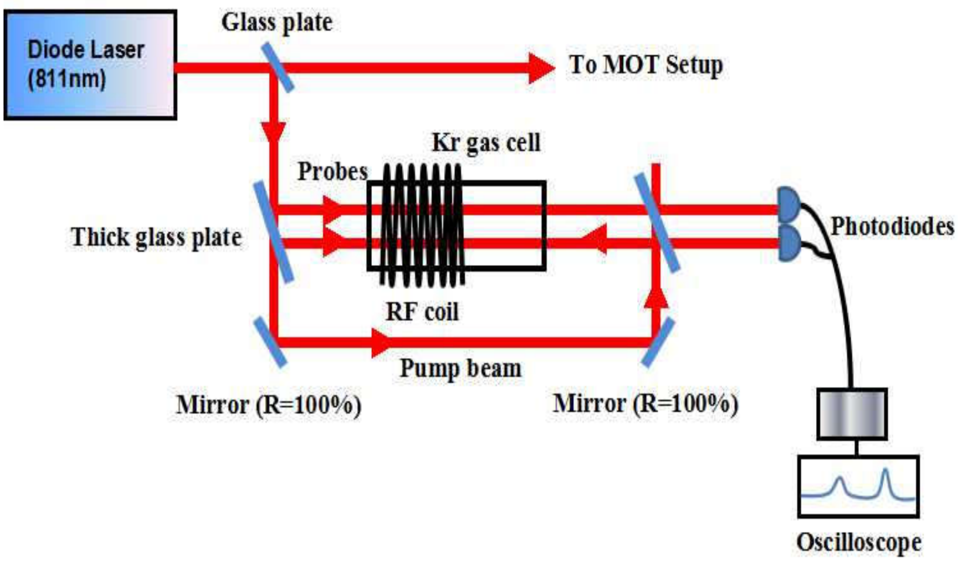

Fig. 3.1: Schematic of the saturated absorption spectroscopy setup.

The schematic of the experimental setup for the SAS of Kr* atoms is shown in Fig. 3.1. A small portion of laser power was reflected from the glass plate for spectroscopy and rest of the laser is transmitted and directed to MOT setup for laser atom cooling and trapping. The Kr atoms are excited in the metastable state using the RF excitation mechanism which has already been explained in the previous chapter. Two counter propagating linearly polarized laser beams pass through a Kr gas cell at a pressure of ~ 200 mTorr. Both the beams were derived from the same laser system. For the laser frequency, different than the atomic transition frequency, one beam interacts with a group of atoms with velocity v and the other beam interacts with another group of atoms with velocity -v. When the laser frequency was tuned to the atomic transition frequency, both the beams interacted with only one group of atoms with velocity, v=0 along the path of laser beam. In this case, if one of the laser beams (pumped beam) is strong enough to saturate the atomic transition, then over a narrow range of frequencies the absorption of the probe beam decreases and a narrow dip is observed in the Doppler broadened absorption profile using a photodiode detector. To eliminate the Doppler profile, a third probe (reference) beam was passed through the Kr gas cell and was detected by another photodiode. Two signals detected by a pair of photodiodes were electronically subtracted to obtain only the saturated absorption dips on a flat background. These dips arise from the transition between different fine and hyperfine energy levels of the Kr* atoms over the tuning range of frequencies. There were some peaks which lies exactly between the two principle peaks are called cross-over peaks. These cross-overs peaks originate due to two beams resonate with two different transitions interact with same velocity class of atoms. In order to explain the existence of the cross-over peaks, let us consider two hyperfine transitions corresponding to two resonant frequencies ω_1 and ω_2 such that ω_1-ω_2 is less than Doppler width and both share the lower transition level. At laser frequency $\omega_c = (\omega_1+\omega_2)/2$, a group of atoms moving in the direction of the pump beam with velocity $v_{z1} = (\omega_c-\omega_1)/k = [(\omega_1+\omega_2)/2 - \omega_1]/k = (\omega_2- \omega_1)/2k$ will see the laser frequency red shifted in resonance with ω_1. Same group of atoms, now moving opposite to the counter propagating probe beam [$v_{z1} = (\omega_2- \omega_c)/k = [\omega_2 - (\omega_1+ \omega_2)/2]/k = (\omega_2- \omega_1)/2k$] will also see the laser frequency blue shifted in resonance with ω_2. Hence, cross-over signals at laser frequency ω_c is obtained due to saturation of this group of atoms by the pump beam. Here, $k = 2\pi/\lambda$ is the magnitude of the wave vector.

The photograph of the actual experimental SAS setup for Kr* atoms is shown in Fig. 3.2. The length and diameter of RF excited Kr gas cell was 10 cm and 2.5 cm respectively with a Kr gas pressure of ~ 200 mTorr. Initially 1.5 W RF power at ~30 MHz was required to ignite the discharge and later, discharge was sustained upto around 50 mW RF power. The RF amplifier and the impedence matching circuitry to couple the RF power to the Kr gas cell were developed inhouse. As discussed in the previous chapter the excitation of atoms to the metastable state $4p^5 5s[3/2]_2$ from ground state($4p^6$) is through electron impact mechanism. For even isotopes, the transition $4p^5 5s[3/2]_2 \rightarrow 4p^5 5s[5/2]_3$ is excited by laser light of wavelength 811.5 nm. However, for odd isotopes, metastable levels $4p^5 5s[3/2]_2$ and $4p^5 5s[5/2]_3$ have many energy levels due to hyperfine interaction.

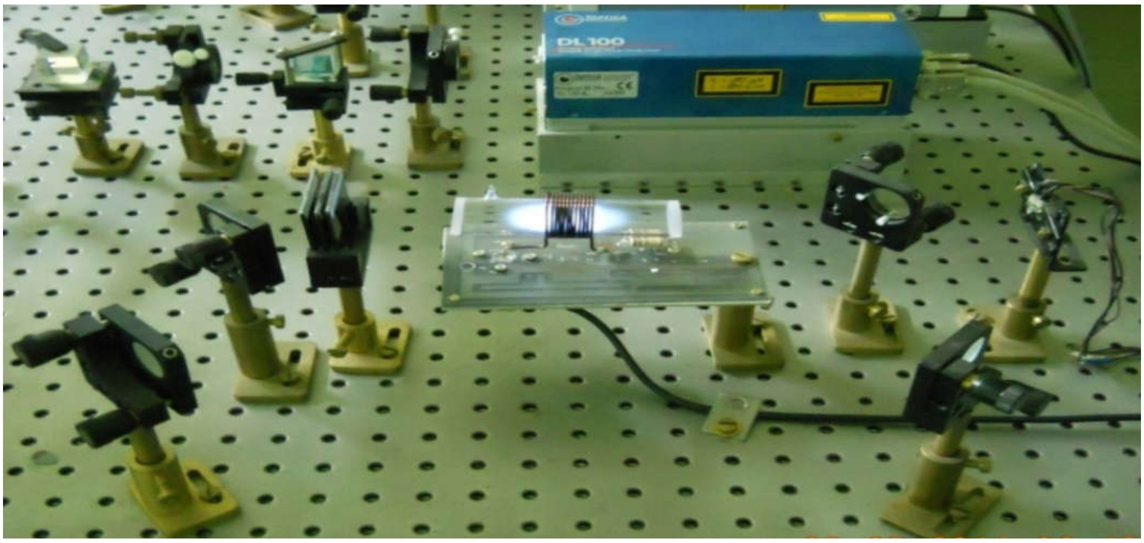

Fig. 3.2: Photograph of actual SAS setup for high resolution spectroscopy of Kr atom in the RF discharge

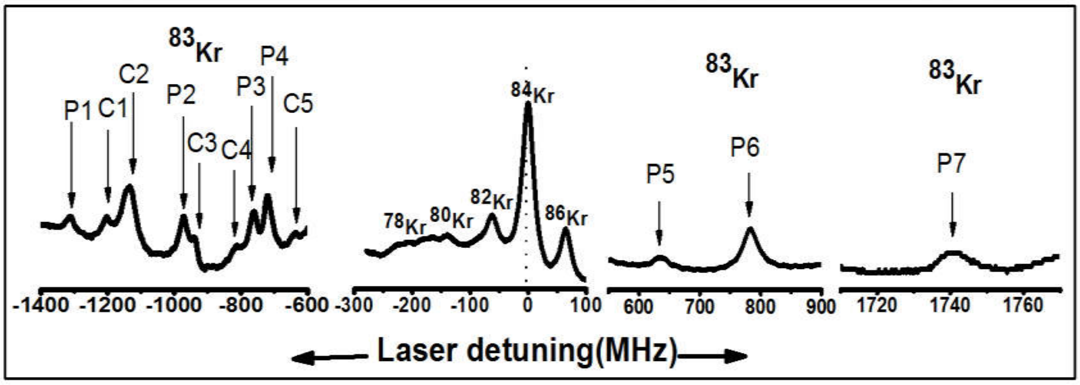

Fig. 3.3: Doppler free saturated absorption spectra of Kr* atoms.

Figure 3.3 shows the experimentally observed Doppler free saturated absorption spectra for various isotopes of Kr* atom. Peaks denoted by P are principal peaks of ^{83}Kr* corresponding to the hyperfine energy levels and peaks denoted by C are cross-overs. P1 to P7 peaks correspond to the transitions (7/2, 5/2), (3/2, 5/2), (7/2, 7/2), (11/2, 9/2), (11/2, 11/2), (15/2, 13/2) and (13/2, 13/2) respectively. C1, C2, C3, C4 and C5 correspond to cross-over between (7/2, 5/2) and (5/2, 5/2), (7/2, 5/2) and (3/2, 5/2), (9/2, 7/2) and (7/2, 7/2), (9/2, 7/2) and (5/2, 7/2) and (7/2, 7/2) and (5/2, 7/2) respectively, where (F', F) are upper and lower hyperfine levels respectively. The obtained accuracy in Doppler free saturated absorption spectroscopy for resolving hyperfine spectra of various isotopes of Kr atoms is only limited by the linewidth of the laser.

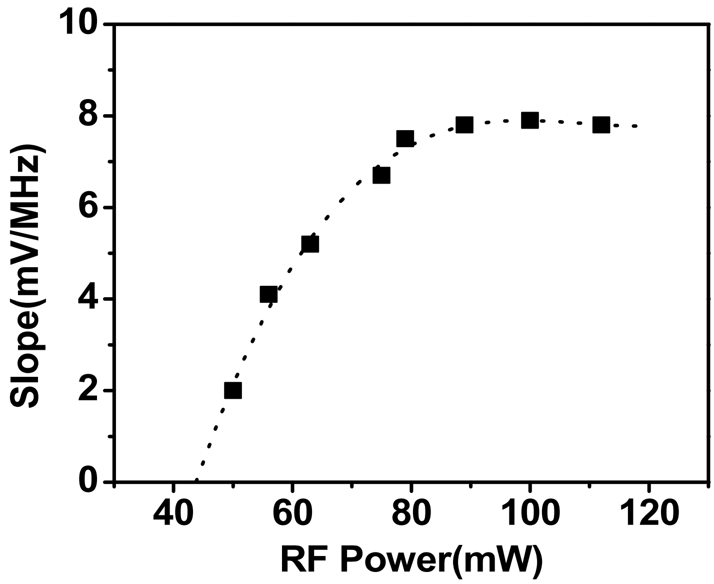

Fig. 3.4: Variation in slope of $^{84}Kr^*$ saturated absorption spectroscopy signal with different RF power. Dotted curve is guide to eye.

The variation of slope of $^{84}Kr^*$ SAS signal was also studied for different RF power applied to inductive coil for maintaining the discharge in the cell. The variation in the slope of $^{84}Kr^*$ SAS signal with different RF power is shown in the Fig. 3.4. It was observed that the discharge region in the cell grows approximately linearly with the RF power and reaches maximum at around 80 mW RF power. This was also confirmed with the observed height as well as slope of the SAS signal. After this power level, the discharge region covered nearly whole cell length. Laser frequency locking using SAS signal for this maximum slope is expected to provide better frequency stabilization.

3.3.2 Atomic beam fluorescence spectroscopy (ABFS)

In this technique, the fluorescence signal from the atomic beam of Kr* atoms, which are to be laser cool in the MOT, was generated for locking the cooling laser frequency. This atomic beam fluorescence spectroscopy (ABFS) setup was a part of the MOT setup. The ABFS signal was obtained by exciting the Kr* atomic beam using a probe laser beam, which was a part of the cooling laser beam and intersects with the atomic beam in the observation chamber at an angle. By varying this angle between the probe laser beam and the atomic beam, the spectral shift in the fluorescence signal can be achieved to obtain the desired frequency offset (i.e. detuning) for locking the cooling laser frequency. The dependence of the atomic beam fluorescence (ABF) signal (i.e. peak height and slope) on the RF power in the discharge tube and pressure in the setup (observation chamber) was studied to correlate its effect on the number of atoms in the MOT. Earlier, the frequency stabilization schemes other than the SAS technique have also been reported. Fletcher et al. [7] have generated a frequency locking signal using the fluorescence from cold atoms in a MOT. Douglas et al. [8] implemented another laser frequency stabilization scheme using a frequency locking signal generated by the absorption from metastable Argon atoms produced for loading a MOT.

In the following section, the study on an atomic beam loaded MOT for even isotope ^{84}Kr* atoms is presented and the atomic beam fluorescence was used to lock the cooling laser frequency.

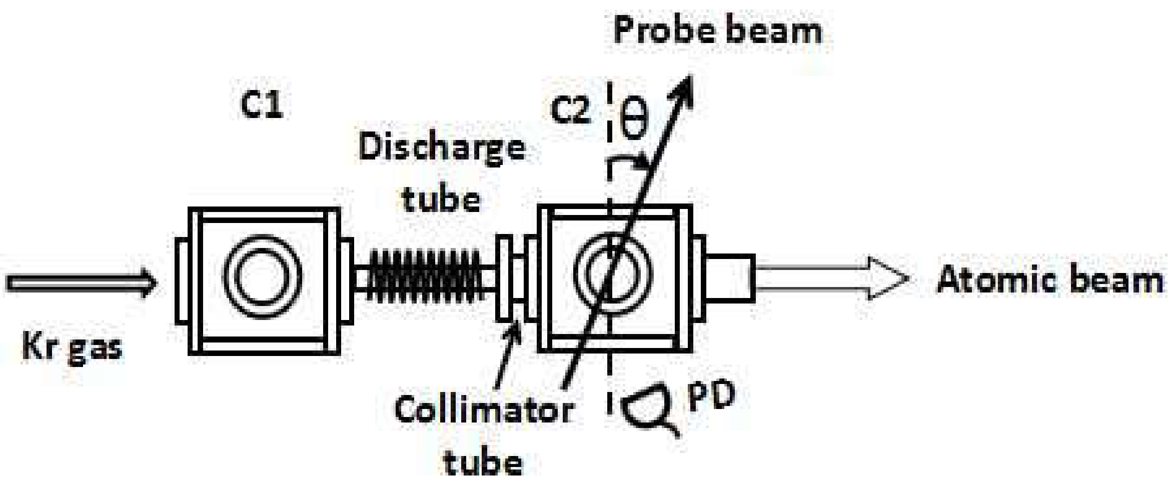

Fig. 3.5: Schematic of the experimental setup for atomic beam fluorescence spectroscopy. C1 and C2 are the source chamber and the observation chamber respectively.

To generate the signal for frequency locking, a part of the cooling laser beam (i.e. probe beam as shown in the Fig. 3.5) was passed through the observation chamber such that it was at a small angle (θ) from the perpendicular to the atomic beam propagation direction. The desired atomic beam fluorescence (ABF) signal was generated by tuning the laser frequency around $5s[3/2]_2 \rightarrow 5p[5/2]_3$ transition of ^{84}Kr* and detecting the fluorescence from the atomic beam using a sensitive photodiode (PD). The typically observed atomic beam fluorescence (ABF) signals for three different values of the probe angle θ are shown in the Fig. 3.6. Such ABF signals were used to lock the laser frequency as well as to achieve a variable detuning of the laser during the experiments. The locking was always chosen at ~ - 6 MHz from the peak of the ^{84}Kr* ABF signal. The variable detuning of the cooling laser was achieved when peak position of the signal was varied by varying the angle θ.

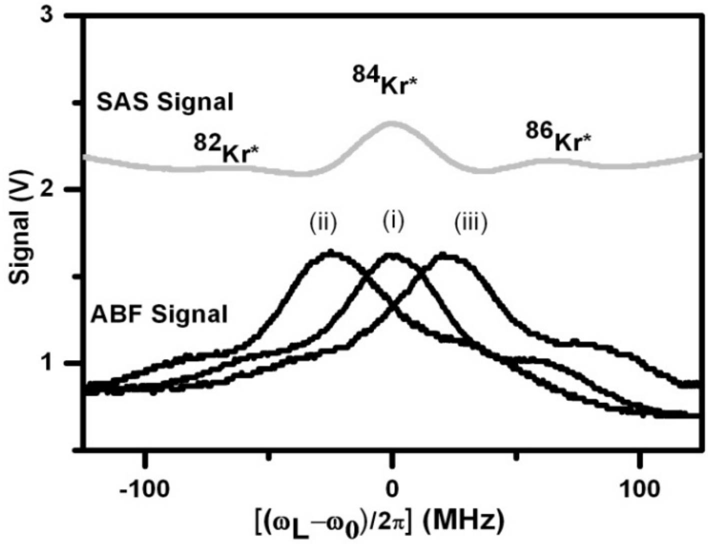

Fig. 3.6: The atomic beam fluorescence (ABF) signal at three different probe beam angles, (i) $\theta = 0^0$, (ii) $\theta = -4^0$ and (iii) $\theta = 4^0$. Here, ω_L and ω_0 are respectively the cooling laser frequency and ^{84}Kr* atomic transition frequency. The upper curve shows the saturated absorption spectroscopy (SAS) signal for reference.

The slope (mV/MHz) of the ABF signal, which is an important parameter for the stability of the locked laser frequency, was measured at the half of the peak height of the signal voltage. The slope as well as the peak height of the ABF signal varied with the RF power and the pressure in the observation chamber. The measured variation in the peak height of the signal with the pressure in the observation chamber is shown in Fig. 3.7 (a), for different values of the RF power in the discharge tube. The corresponding variation in the slope of the ABF signal is shown in Fig. 3.7 (b). For these measurements, the probe beam was kept at an angle $\theta = 0^0$ (i.e. the probe beam was perpendicular to the atomic beam). We find that, at a given RF power in the discharge tube, there exists an optimum pressure at which the peak height and the slope of the signal are maximum. Both, the RF power and the pressure affect the flux of Kr* atoms in the atomic beam which governs the slope and the peak height of the signal. At a given RF power, the peak height and the slope first increases with the pressure and then decreases with it after reaching a maximum value (Fig. 3.7 (a) and 3.7 (b)). With the increase in the pressure, initially, the number density of atoms in the chamber increases which results in the more production of the metastable atoms. With further increase in the pressure, the de-excitation of metastable atoms due to collisions with the ground state atoms increases. This results in the decrease in the peak height as well as in the slope, after attaining the maximum values, as the pressure was increased.

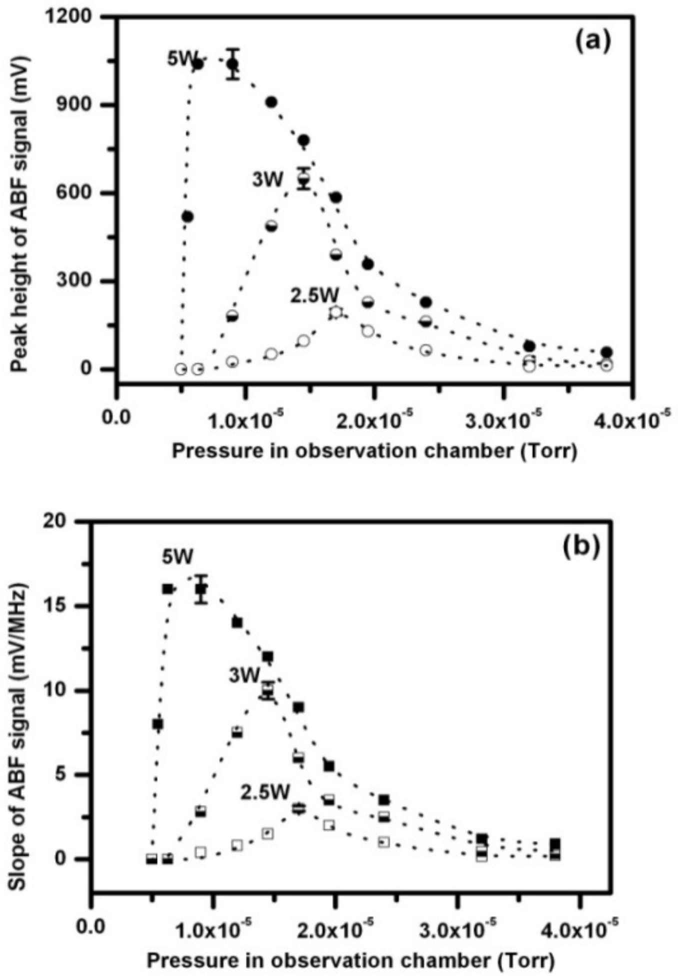

Fig. 3.7: (a) Variation in the peak height of the $^{84}Kr^*$ atomic beam fluorescence (ABF) signal with pressure in the observation chamber for different values of the RF power, and (b) the variation in the slope of $^{84}Kr^*$ ABF signal with the pressure for different values of the RF power. The probe beam was kept at $\theta = 0^0$. The dotted lines are guide to eye. The error bars shown are determined from scatter in the values obtained in the repeated measurements.

In the variation with the RF power (at constant pressure), the peak height and the slope of the locking signal first increases with the RF power and then saturates as shown in the Fig. 3.8. The increase in signal and its slope with the RF power is due to increase in electron-atoms collisions with increase in the RF power. The increased collision rate results in the increased production of atoms in the metastable state. The saturation of signal height (and slope) at higher RF power occurs due to saturation in the number density of the metastable atoms produced in the discharge [9].

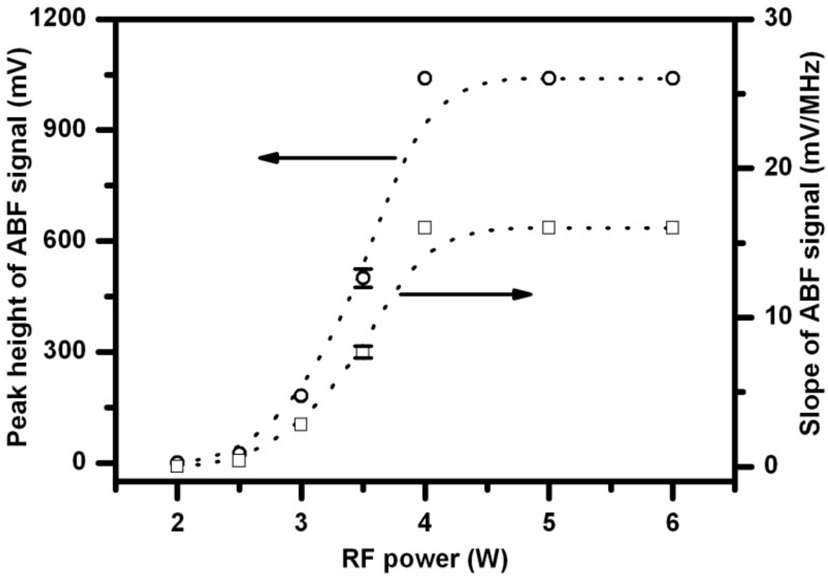

Fig. 3.8: Variation in the peak height and slope of the ABF signal of ^{84}Kr* with RF power, at ~ $1x10^{-5}$ Torr pressure in the observation chamber and at probe beam angle $\theta = 0^0$. The dotted lines are guide to eye. The error bars shown are determined from scatter in the values obtained in the repeated measurements.

From the observations shown in the Fig. 3.8, it is evident that the number of Kr* atoms in the atomic beam (i.e. flux) changes with the RF power. This should also affect the loading of the Kr*-MOT. In order to verify this, the RF power was varied at constant pressure and measured the variation in ^{84}Kr* number of atoms in the MOT. The measured variation in the number of atoms in the MOT with the RF power is shown in the Fig. 3.9. Here, for each RF power, laser was locked at the side of the ^{84}Kr* transition peak with a fixed detuning of ~ - 6 MHz. The probe beam was kept at an angle $\theta = 0^0$ for generation of the ABF signal. The number of atoms in the MOT was estimated by the fluorescence imaging method after collecting the fluorescence from the MOT cloud on a CCD camera [10-11]. As can be noted from the Fig. 3.9, the cold atom number first increases with the RF power and then saturates. This saturation in the number of cold ^{84}Kr* atoms in the MOT is due to the saturation of the number of ^{84}Kr* atoms produced in the discharge.

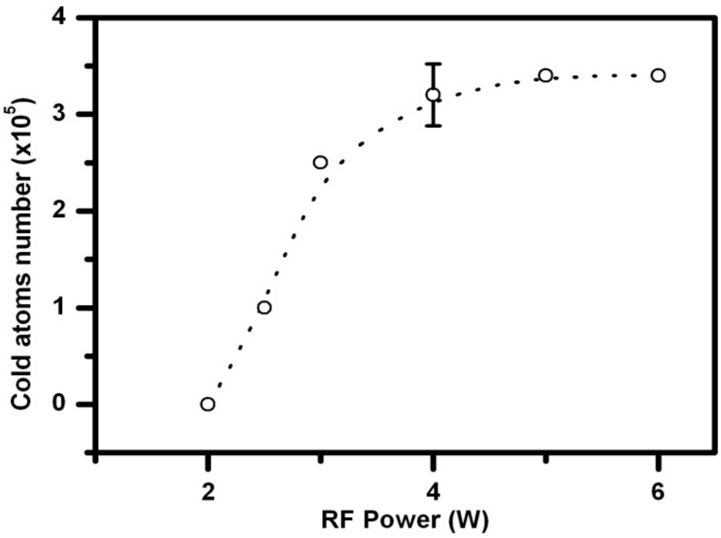

Fig. 3.9: The measured variation in the cold atoms number (^{84}Kr*) in the MOT with the RF power at a pressure of 9x10^{-6} Torr in the observation chamber. The dotted lines are guide to eye. The error bar shown is determined from the scatter in the values obtained in the repeated measurements.

Next, by varying the angle θ, the peak position of the generated ^{84}Kr* ABF signal was varied. Using this variation of the peak position, the detuning of cooling laser frequency from the resonance frequency was varied by varying the angle θ and keeping the locking position fixed from the signal peak position. It was observed that the cold atom number in the MOT was maximum at the cooling laser detuning of ~ - 6 MHz as shown in Fig. 3.10. This study is useful to optimize the detuning of the cooling laser for maximizing the cold atom number in the trap. The variation in detuning can also be useful to set the value of temperature of atoms in the MOT. It is noted that the ABF signal is dependent on the pressure, RF power and temperature of the Kr gas in the setup. The RF power and the pressure in the chambers were set to particular values after optimizing the number of atoms in the MOT. The fluctuations in the RF power (~ ± 6%) and the variation in the pressure (which was ~2% over 8 hrs of duration) in the observation chamber make a negligible contribution to the frequency fluctuations of the locked laser. The temperature in the laboratory was also kept nearly constant (in the range of 21 - 22 ^{0}C). This variation in the temperature does not change the Doppler width of the ABF signal significantly. It was observed that the laser remained locked with the ABF signal for ~ 1 hour during the experiments.

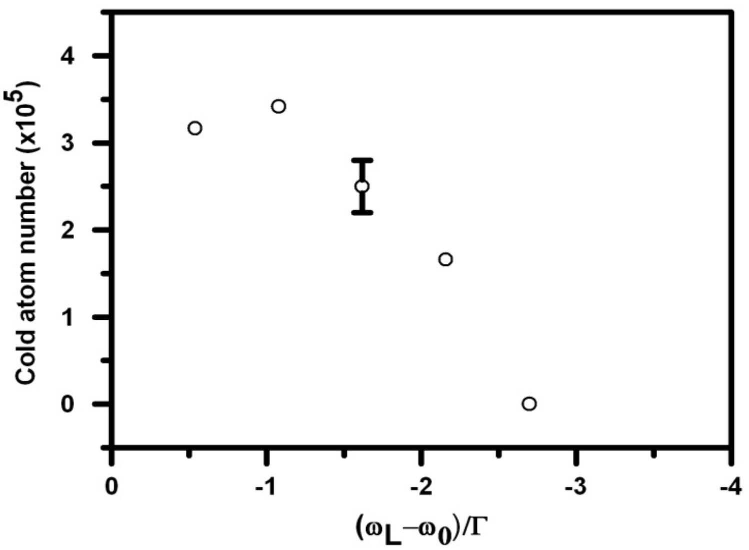

Fig. 3.10: The measured variation in the cold atoms number with the detuning of cooling laser beam. The error bar shown is determined from the scatter in the values obtained in the repeated measurements.

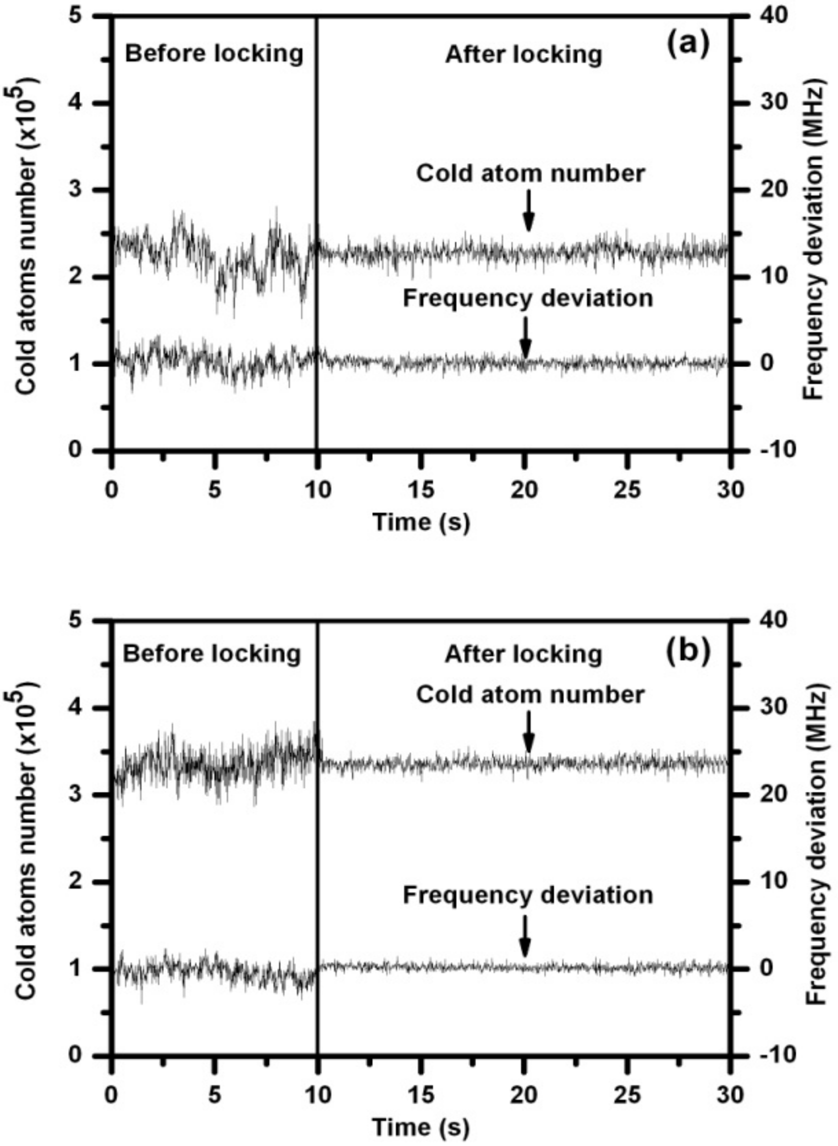

Fig. 3.11: The measured variation in the cold atoms number in the MOT and the cooling laser frequency deviation with time, before and after locking the cooling laser frequency. Figures (a) and (b) correspond to the different values (10 mV/MHz and 16 mV/MHz respectively) of the slope of the ABF signal. The probe beam was at an angle $\theta = 0^0$.

Fig. 3.11 (a) and 3.11 (b) shows the fluctuations in the cooling laser frequency and the number of cold atoms in the MOT, before and after locking of the cooling laser for two different slopes, 10 mV/MHz and 16 mV/MHz, which correspond to the pressure in the observation chamber 1.5×10^{-5} Torr and 9×10^{-6} Torr respectively. In this figure, the frequency deviation has been derived from the deviation of the signal voltage from the set reference voltage. For locking the laser frequency, a standard PID controller (TOPTICA, Germany) is used which has earlier provided a good long-term frequency stability [12]. For data shown in the Fig. 3.11 (a) and 3.11 (b), the PID setting of the servo control was kept the same for the signals having different values of the slope. As is evident from these figures that both the cold atoms number and error signal (i. e frequency deviation) show the significant reduction in the fluctuations after locking of the cooling laser frequency. Figure 3.11 (a) shows that the fluctuations in the cold atom number in the MOT gets reduced from ± 30% (before locking) to ± 10% (after locking) whereas the fluctuations in the frequency gets reduced from ± 2 MHz (before locking) to ± 0.5 MHz (after locking). Upon locking with a higher slope of 16 mV/MHz (Fig. 3.11(b)), the corresponding fluctuations in the cold atom number and the laser frequency fluctuations get further reduced [13].

3.4 Operation and characterization of MOT setup

The MOT for Kr* atoms consists of three pairs of counter-propagating laser beams directed along three mutually orthogonal axes in presence of a quadrupole magnetic field to provide spatially varying Zeeman shift. The schematic of the experimental setup and photograph of actual setup for Kr* atom cooling is shown in Fig. 3.12 (a) and (b) respectively.

The Krypton gas first flows into the RF discharge glass tube through the inlet chamber (C1) with pressure ~10^{-3} Torr and its flow is controlled by a fine leak valve attached with the Krypton gas cylinder. The glass tube has inner diameter of 10 mm and length of 150 mm.

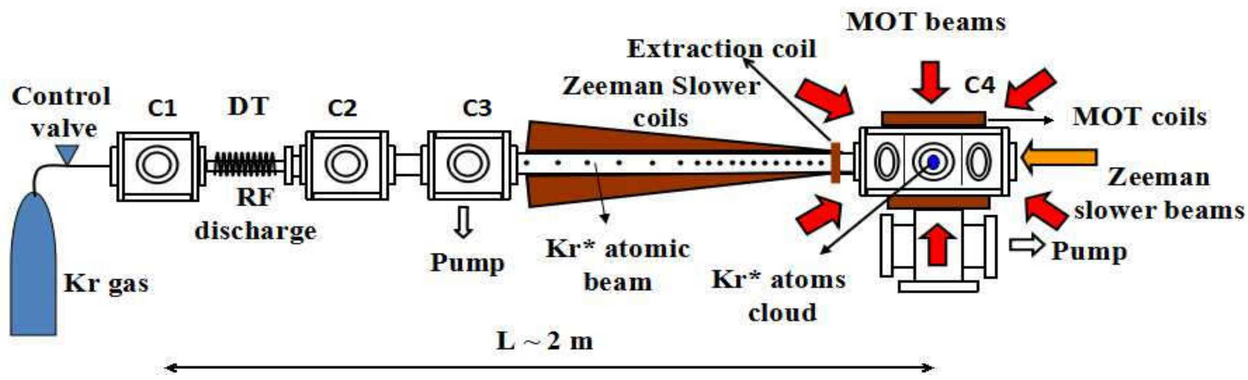

(a)

(b)

Fig. 3.12: (a) Schematic of the experimental setup for cooling and trapping of metastable Kr atoms. C1, C2, C3: different vacuum chambers; DT: discharge tube; ZS: Zeeman slower; MOT: magneto-optical trap. (b) Photograph of actual setup.

The Kr* atoms produced in this tube by the RF-driven discharge (frequency ~ 30 MHz) pass through the analysis chamber (C2) with pressure ~10^{-5} Torr. A stainless-steel tube of inner diameter 5 mm and length 50 mm has been used between the discharge tube and analysis chamber to set appropriate conductance between the chambers for obtaining the desired differential pressure. It also helps in collimating the atomic beam flowing towards analysis chamber. A Zeeman slower (length ~ 80 cm) along with an extraction coil was connected between the pumping chamber (C3) with pressure ~ 10^{-6} Torr and the MOT chamber (C4) with pressure ~ 10^{-8} Torr. It slows down the ^{84}Kr* atomic beam before cooling and trapping in the MOT chamber. This laser beam propagates opposite to the atomic beam and is σ^+ polarized. Its frequency was detuned by ~ 80 MHz to the red of the ^{84}Kr* transition between $5s[3/2]_2$ and $5p[5/2]_3$ states. The cooling laser beam for the MOT was split into three beams each having ~ 5 mW power (size $1/e^2$ radius ~ 3 mm). These beams were used in the retro-reflection geometry to obtain desired six beams for the MOT. The frequency of the MOT cooling laser was kept at ~ 6 MHz red-detuned to the $5s[3/2]_2 \rightarrow 5p[5/2]_3$ transition of ^{84}Kr*. A pair of anti-Helmholtz magnetic coils provided the magnetic field gradient of ~ 10 Gauss/cm for the MOT formation.

The optical layout for laser cooling of Kr atoms is shown in Fig. 3.13 for generation of six counter propagating counter circularly polarized laser beams for cooling and trapping of Kr* atoms. There are two saturated absorption spectroscopy setups for generating the frequency reference for locking of lasers using PID. Appropriate half- wave plates and quarter wave plates along with polarizing beam splitter cube are used for splitting the laser beams. Beam expanders are used for expanding the beams. AOMs are used for shifting the laser frequency. One frequency shifted circularly polarized (σ+) laser beam is also used for Zeeman slowing propagating opposite to the atomic beam.

Figure 3.14 shows the CCD image of the ^{84}Kr* cold atomic cloud in presence of cooling laser beams. Precise knowledge of number, size, temperature and loading rate of cold atomic cloud are of importance for any experiment with the cold atoms and hence measurement of these parameters is essential in the cooling setup. In the following sub section the details of the methods used to measure the various parameters mentioned above are discussed.

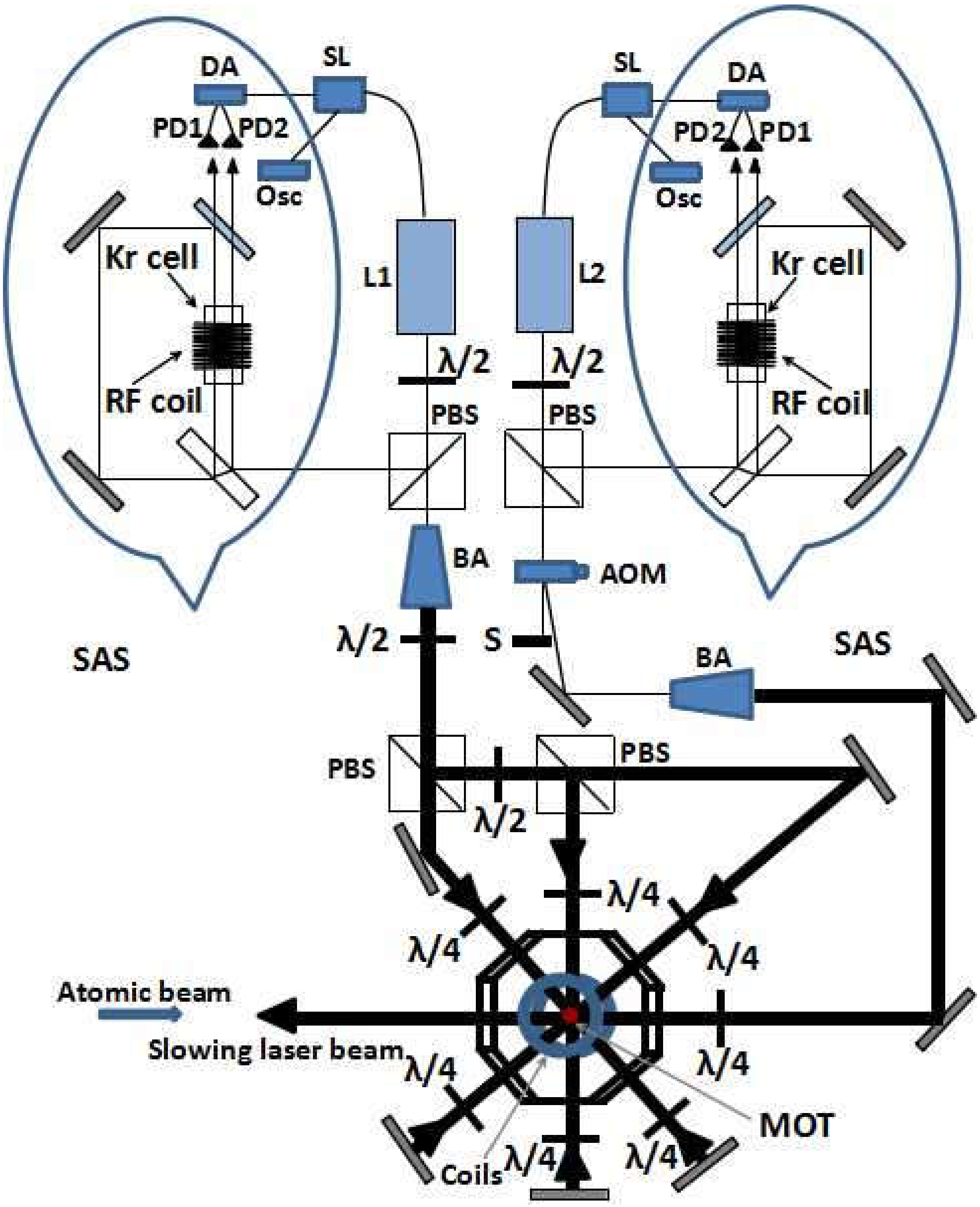

Fig. 3.13: Schematic of optical setup for cooling and trapping of metastable Kr atoms. SAS: saturated absorption spectroscopy, PD: photodiode, DA: difference amplifier, Osc: oscilloscope, SL: servo lock, L: laser head, PBS: polarizing beam splitter cube, BA: beam expander, AOM: acousto-optic modulater, S: beam stopper, λ/2: half wave plate, λ/4: quarter wave plate, MOT: Magneto-optical trap.

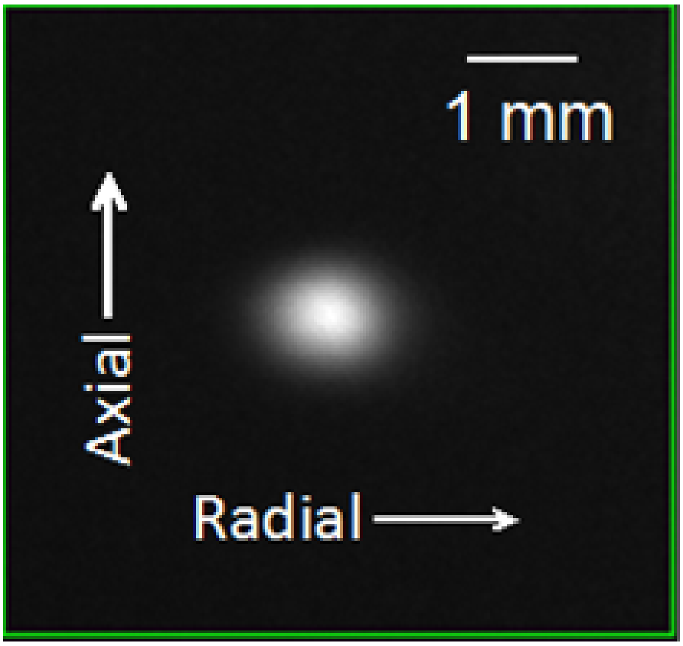

Fig. 3.14: CCD image of $^{84}Kr^*$ cold atomic cloud in the magneto-optical trap.

3.4.1 Number measurement of cold atoms in a MOT

After loading the atoms in the MOT, the cold atom number in the MOT was estimated by collecting the fluorescence from the cold atomic cloud on a CCD camera or on a calibrated photodiode using Eq. (1.12) in case of CCD camera and Eq. (1.13) in case of photodiode. The number of cold atoms obtained in the MOT was ~10^6. The sizes (FWHM) of cold atomic cloud along the radial and axial direction are 1.2 mm and 1 mm respectively. Using these values, the peak number density in the atomic cloud is estimated to be ~10^8 cm^{-3} [14].

3.4.2 Temperature measurement of cold atomic cloud in a MOT

As discussed earlier, for low number of atoms in the MOT, the transient probe absorption technique works better than the commonly used free-expansion technique for the temperature measurement of the cold atomic cloud. So, the transient probe absorption technique [15-16] was used to estimate the temperature of the cold atomic cloud and compared the results with that obtained from the size measurement of the cold atomic cloud [17]. Although, the temperature measurement of the cold atomic cloud was tried by standard free expansion imaging method but because of very strong background and low number of atoms in the MOT, expansion images were not good enough to analyze for measuring the temperature.

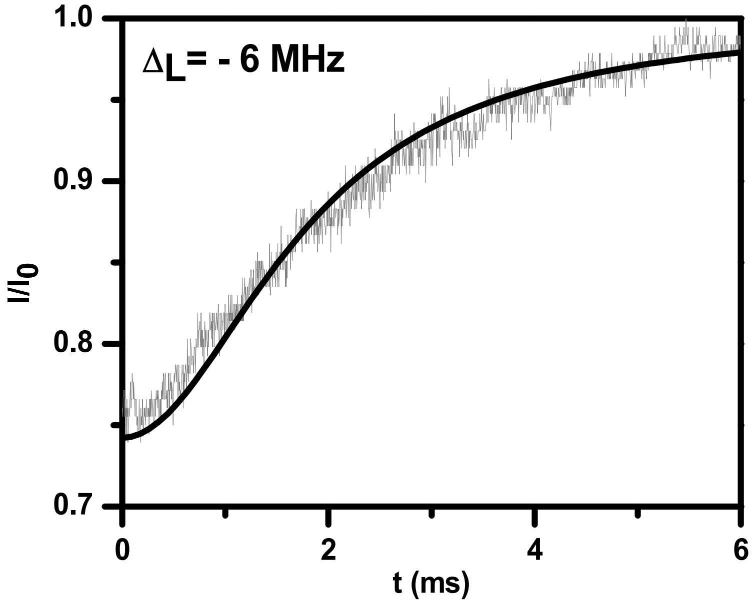

Fig. 3.15: Typical absorption signal as a function of time, detected on a photodiode detector during the free expansion of the cold atomic cloud. The MOT was formed with each cooling beam power of 5mW with $1/e^2$ radius of ~ 3 mm and detuning - 6 MHz. Probe beam power was ~ 25 μW with $1/e^2$ radius of 200 μm. Solid line is the best fitted curve for given value of ρ_z and N_0.

In the transient probe absorption technique, absorption of a weak probe beam passing through the cold atomic cloud in the MOT during the free expansion of the cloud was measured using a photodiode detector. The weak resonant probe beam of ~ 25 μW power with $1/e^2$ radius of 200 μm was passed through the cold atomic cloud in the MOT. It was observed that this probe beam does not change the shape of the cloud. This indicates that the probe beam does not significantly heat the cloud to change its temperature. When MOT beams are switched-off, the time evolution of the absorption signal gives the information about the atomic density at different time during the free-expansion of the cloud. The transmitted intensity (I) at different time (t) can be expressed by Eq. (1.16) during the free expansion of the cold atomic cloud.

The temperature was estimated by fitting the experimental curve as shown in the Fig. 3.15 with the Eq. (1.16) for the known values of ρ_z and N_0 measured using CCD camera.

Temperature of the cold atomic cloud was also estimated by the size determination technique using Eq. (1.18). The temperature of the trapped atoms was measured for different detuning of the cooling laser by substituting the experimentally observed ρ_z of the cold atomic cloud and estimated the temperature using Eq. (1.18). Results obtained for cooling laser detuning from both the techniques were compared and plotted in Fig. 3.16. It is evident from the figure that the temperature measured from both the techniques are in good agreement [18].

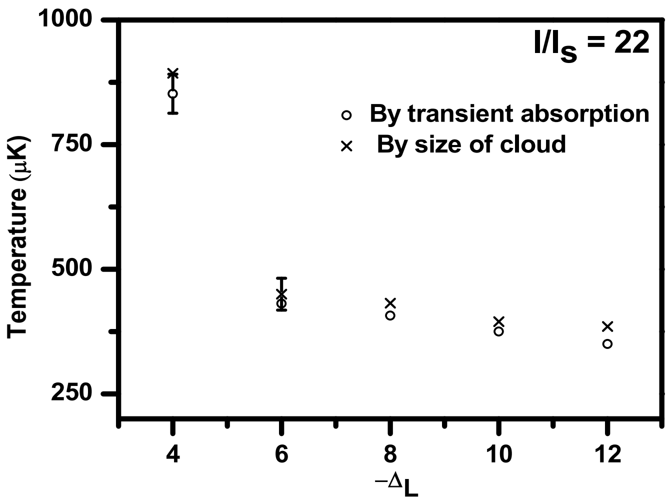

Fig. 3.16: Measured variation of temperature of the cold atomic cloud in the Kr*-MOT for different detuning of the cooling laser beam by transient absorption (empty circle) and size determination (cross) techniques. The error bars shown were determined from scatter in the values obtained in the repeated measurements.

3.4.3 MOT loading

In the constant volume regime, which is the case of our MOT operation, the solution of the loading rate equation is given by Eq. 1.21. The values of the MOT loading time is estimated by fitting this to the experimentally observed loading curve of the atoms in the MOT.

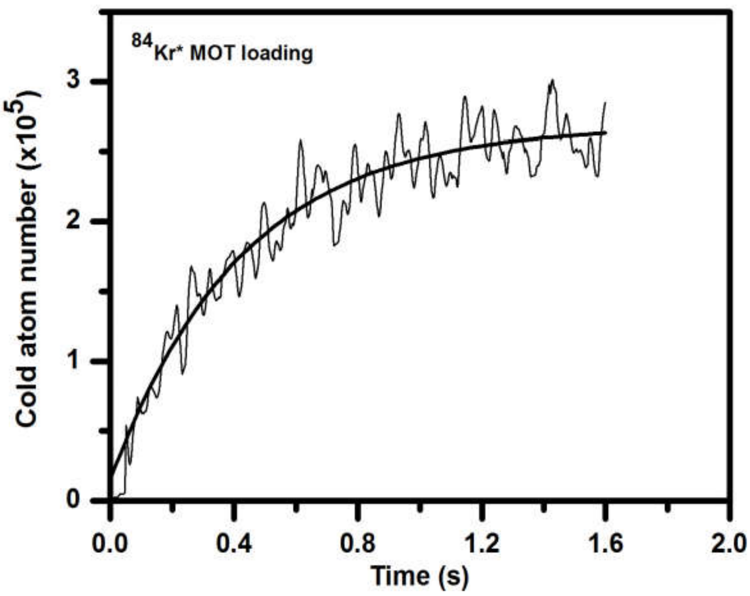

Fig. 3.17: Loading curves of ^{84}Kr* MOT. The cooling laser beam intensity in each beam was ~ 3.5 mW/cm^2 and the detuning was ~ - 6 MHz from the resonance transition of ^{84}Kr*. The Solid lines show the fitted curves.

The Fig. 3.17 shows the typical loading curves of the ^{84}Kr*-MOT. The estimated MOT loading time was ~ 250 ms. The cooling beam intensity in each beam was ~ 3.5 mW/cm^2 and detuning was kept ~ - 6 MHz from the cooling transitions of ^{84}Kr* using the SAS setup. A σ+ polarized Zeeman slowing laser beams with power ~ 7 mW and detuning ~ - 70 MHz from the cooling transition of ^{84}Kr* was passed opposite to the direction of the propagation of the atomic beam. The 1/e^2 radius of the cooling as well as Zeeman slower beams was ~ 3 mm.

3.5 Conclusion

In conclusion, the work related to the development of a magneto-optical trap setup for metastable Krypton (Kr*) atoms has been discussed. This includes the investigations and optimization made on various parts and sub-systems during the assembly and operation of the MOT setup.

It was also demonstrated that atomic beam fluorescence technique is a simple and useful for the frequency stabilization of a laser for the ^{84}Kr*-MOT which provides a wider locking range than SAS technique. The spectral shift in fluorescence signal, obtained by varying the angle between the probe laser beam and the atomic beam, provides the opportunity to lock the laser frequency over a wide spectral range. Besides this, the technique of ABFS for frequency stabilization makes the setup simple by eliminating the requirement of a separate Kr-cell based SAS stabilization setup.

Various measurement on the cold atoms cloud in the MOT have been carried out. The number of atoms obtained in the MOT was ~10^6 at temperature of ~ 300 μK. The sizes (FWHM of the image profile) of atomic cloud along the radial and axial direction are 1.2 mm and 1 mm respectively, which correspond to the peak number density in the cloud as ~10^8 cm^{-3}. The loading time of the MOT was observed to be ~ 250 ms.

The temperature of the cold Kr* atom in the MOT was measured by transient absorption technique and compared the results with measurement of temperature by size of cloud. The results were found to be in good agreement. The transient absorption technique is simple and sensitive and can be used to determine the temperature of cold atomic cloud with low number of atoms where free-expansion method is difficult to apply.

References:

1. W. Demtroder, Laser Specroscopy, second ed., springer, Berlin, (1998).
2. K. B. MacAdam, A. Steinbach, and C. Wieman, Am. J. Phys. **60**, 1098 (1992).
3. C. E. Wieman and L. Hollberg, Rev. Sci. Instrum. **62**, 1 (1991).
4. T. Ikegami, S. Sudo, and Y. Sakai, Frequency stabilization of semiconductor laser diodes, Artech House, Boston, (1995).
5. C. Ye, Tunable external cavity diode lasers, World Scientific Publishing Co. Pte. Ltd., Singapore, (2004).
6. S. Singh, V. B. Tiwari and H. S. Rawat, Abstract book of DAE-BRNS National Laser Symposium, RRCAT, Indore, Dec. 1-4, 5.28(2010).
7. C. S. Fletcher, J. E. Lye, N. P. Robins and J. D. Close, Opt. Commun. **212**, 85 (2002).
8. P. Douglas, C. Maher-McWilliams and P. F. Barker, Rev. Sci. Instrum. **83**, 063107 (2012).
9. Ying Li, Zhuo chen, Yi-Kang Pu, Plasma Process. Polym. **2**, 581(2005).
10. S. R. Mishra, S. P. Ram, S. K.Tiwari and S. C. Mehendale, Phys. Rev. A **77**, 065402 (2008).
11. V. B. Tiwari, S. Singh, H. S. Rawat and S. C. Mehendale, Phys. Rev. A **78**, 063421(2008).
12. V. B. Tiwari, S. Singh, S. R. Mishra, H. S. Rawat and S. C. Mehendale, Appl. Phys. B **83**, 93(2006).
13. S. Singh, V. B. Tiwari, S. R. Mishra and H. S. Rawat, Laser physics **240**, 25501(2014).
14. S. Singh, V. B. Tiwari, S. R. Mishra and H. S. Rawat, Abstract book of DAE-BRNS

National Laser Symposium (NLS- 22), Manipal university, Jan. 8-11, (2014).

15. Xinye Xu, Thomas H. Loftus, John L. Hall, Allen Gallagher and Jun Ye, J. Opt. Soc. Am. B **20**, 968 (2003).

16. R. R. Silva, K. M. F. Magalhaes, E. A. L. Henn, L. G. Marcassa, V. S. Bagneto, Opt. Commun. **265**, 526(2006).

17. H. J. Metcalf and P. van der Straten, Laser Cooling and Trapping (New York: Springer) (1999).

18. S. Singh, V. B. Tiwari, Y. B. Kale, S. R. Mishra and H. S. Rawat, Abstract book of DAE-BRNS National Laser Symposium (NLS- 23), Sri Venkateswara University Dec. 3-6, (2014).

Chapter 4

Krypton MOT loading studies using two hollow Zeeman slower laser beams

4.1 Introduction

As discussed earlier, the laser cooling of Kr gas atoms is possible only in the metastable state. The excitation of the Kr atoms to the metastable state is achieved by a radio frequency (RF) excitation due to its simplicity [1-2]. In the magneto-optical trap (MOT) setup, the metastable Kr (Kr*) atoms were generated in the discharge section of the setup and finally transported to the MOT chamber for cooling and trapping. One of the important requirement for efficient loading (cooling and trapping) of the atoms in the MOT is to reduce the longitudinal velocity of the atoms in the atomic beam below the capture velocity of the MOT. Another requirement is that the atomic beam should have high flux of the slowed metastable atoms for significant loading of the atoms in the MOT. The slowing of the Kr* atomic beam is conveniently achieved by using a Zeeman slower [3] which is used to decelerate the neutral Kr* atoms in the atomic beam before its entry into the MOT chamber. The Zeeman slower decelerates the atoms through Doppler laser cooling of atoms in the presence of a spatially varying magnetic field. The deceleration results from the scattering force on an atom due to a laser beam propagating opposite to the atomic beam direction. The variation of the magnetic field in the Zeeman slower was so adjusted that the Zeeman shift in the atomic transition frequency compensates for the Doppler shift in the laser frequency seen by a moving atom. Thus, the slowing laser beam interacts resonantly to the atoms throughout the length of the Zeeman slower, and leads to the effect slowing of the atomic beam for loading of the MOT.

In a Zeeman slower based atomic beam loaded MOT, a known difficulty is the destruction of the MOT atomic cloud by the Zeeman slower laser beam, as the MOT cloud is formed on the atomic beam axis to which the Zeeman slower laser beam is aligned from the opposite direction. The detuning of the Zeeman slower beam is governed by the velocity group of atoms to be slowed down for cooling and trapping. A far detuned Zeeman slower beam of low intensity may not destroy the MOT cloud. However, Zeeman slower beam of higher intensity is required to increase the number of trapped atoms which may also disturb the cold atomic cloud. This laser beam thus knocks out the trapped atoms from the MOT at its higher power. This perturbation to the MOT cloud can be reduced by the off-axis alignment of the Zeeman slower laser beam, so that the MOT cloud does not come in the way of the Zeeman slower laser beam. This, however, also results in decrease in the number of atoms in the MOT due to poor loading of the MOT caused by the less effective cooling in the Zeeman slower. This problem was tackled by using a hollow Zeeman slower laser beam aligned axially opposite to the atomic beam [4], in such a way that the MOT cloud was formed in the dark central region of the hollow beam. The hollow beam was generated by using a dark spot in the central region of the transverse cross section of a Gaussian beam. This resulted in an enhancement in the number of atoms accumulated in the MOT. In an another work [5], the decelerating Zeeman slower laser beam was tightly focused at a position slightly away (in transverse direction) from the MOT cloud, so that its perturbation to the MOT cloud was as small as possible. But, in this geometry, the number of atoms is expected to be very sensitive to the position of the focus of the Zeeman slower beam.

In the work discussed here, two hollow laser beams of different dark diameter and ring width were used in the Zeeman slower of an atomic beam loaded Krypton MOT. The first hollow beam was generated using a dark spot in the path of a Gaussian laser beam. Using this hollow laser beam as a Zeeman slower beam, the observed enhancement in the number of atoms in the MOT was ~ 30% with respect to the number observed with a Gaussian Zeeman slower beam of the same power. With the use of an additional second hollow laser beam of a larger dark diameter than the first beam, a further enhancement by ~ 30% was observed in the number of cold atoms in the MOT. This enhancement in the number of atoms in the MOT is attributed to more efficient cooling of the off-axis atoms in the atomic beam due to specific intensity profile of the second hollow laser beam. Thus, the use of two hollow laser beams combination in the Zeeman slower resulted in the higher number of atoms in the MOT cloud due to more efficient cooling of the atomic beam with lesser destruction of the MOT cloud, than that was obtained using a regular Gaussian beam in the Zeeman slower. The loading behaviour of the Krypton magneto optical trap with variation in the Zeeman slower parameters was also investigated. The observations show that the Zeeman slower beam can modulate the background atom collisions whereas cold collisions within the trap were nearly unaffected. Therefore, the optimization of the Zeeman slower parameters for enhanced loading of the MOT is an important issue which is also discussed in this chapter.

4.2 Experimental setup

The schematic of our experimental setup for the generation of two hollow laser beams for the Zeeman slower is shown in Fig. 4.1. The first hollow beam was a fixed diameter hollow beam (HB1) which was generated by keeping a transparent glass slide with dark spot in the path of a Gaussian laser beam from an extended cavity diode laser (ECDL) system having maximum power of ~ 50 mW. The optimum size of the dark spot to generate HB1 was found by varying the size of the dark spot for a given ~ 30 mW power in the laser beam (before dark spot) and measuring the number of atoms in the MOT with HB1 beam used in the Zeeman slower. The optimum size of the dark spot was ~1 mm, hence HB1 with this dark spot size was used in further experiments. The second hollow beam was a variable diameter hollow beam (HB2) which was generated by taking a part of the laser beam and passing it through a pair of axicon lenses (with cone angle of 176^0) mounted on a calibrated translation stage (Fig. 4.1). These lenses were facing each other in the path of slowing laser beam [6]. The dark diameter of the hollow beam (d) was varied by varying the separation between the axicon lenses, similar to an earlier work which used a pair of axicon mirrors to generate variable diameter collimated hollow beam [7].

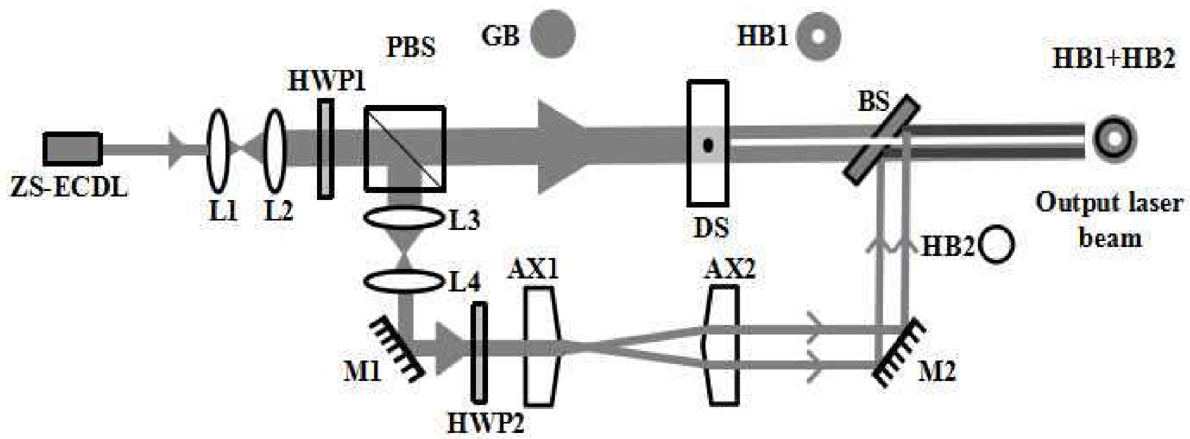

Fig. 4.1: Schematic of the experimental setup for the generation of hollow laser beams. ZS-ECDL: Zeeman slower-extended cavity diode laser, L1, L2, L3 & L4: Lenses of appropriate focal lengths, HWP1 & HWP2: Half wave plates, PBS: Polarizing beam splitter cube, GB: Gaussian beam, DS: Dark spot on the transparent glass plate, BS: Beam splitter, M1 & M2: Mirrors, AX1 & AX2: Axicon lenses, HB1: Hollow beam generated using the dark spot, HB2: Hollow beam generated using the axicon lenses.

The schematic of the experimental setup for cooling and trapping of $^{84}Kr^*$ atoms is shown in Fig. 3.12. The Zeeman slower laser beam used here was composed of two hollow beams as shown in Fig. 4.1.

As already discussed in the design of the Zeeman slower, the magnetic field variation along the atomic beam direction was designed to provide an effective cooling of the longitudinal velocity of an atomic beam. In the magnetic field of the Zeeman slower, the

Zeeman shifted atomic transition frequency is equal to the Doppler shifted frequency of the counter propagating laser beam. The effective detuning (Δ), of the Zeeman slower laser beam from the atomic resonance transition as discussed in chapter 2 is given by Eq. (2.11).

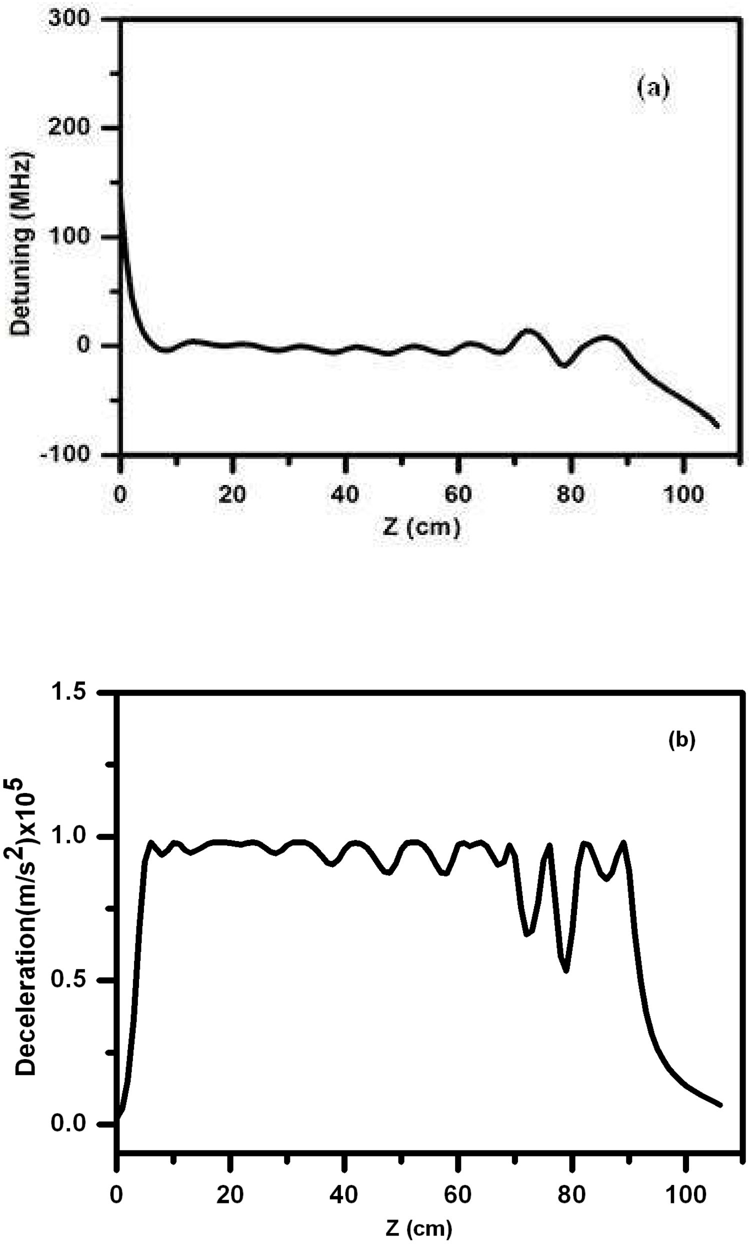

Fig. 4.2: (a) the theoretically calculated variation of the effective detuning observed by the atoms in the Zeeman slower with axial distance, (b) theoretically calculated variation of the effective deceleration observed by the atoms in the Zeeman slower with axial distance for Zeeman slower current = 1.3 A, detuning = - 80 MHz and I/Is = 50.

In order to estimate the longitudinal velocity of an atom at the boundary of the MOT trapping region, initial velocity and deceleration in the Zeeman slower are important parameters. The deceleration *a(z, r)* of the atom in the Zeeman slower at the longitudinal distance z and transverse distance *r* is given by Eq. (2.12). This deceleration governs the variation in the longitudinal velocity with distance z by the equation Eq. (2.13).

Fig. 4.2(a) and (b) shows the theoretically estimated variation of the effective detuning, and the effective deceleration with axial distance as observed by the atoms in the Zeeman slower. The current in the Zeeman slower, detuning and the saturation parameter (I/Is) was kept 1.3 A, - 80 MHz and 50 respectively for the simulation. The oscillatory behavior in the detuning in the Fig. 4.3(a) is because of the segmented design of the Zeeman slower (due to fabrication limitation). The prominent variation at around z = 80 cm in the detuning is because of the additional extraction coil placed at around 80 cm from the edge of the Zeeman slower. Similar trend is also expected in the effective deceleration as seen in Fig. 4.2(b).

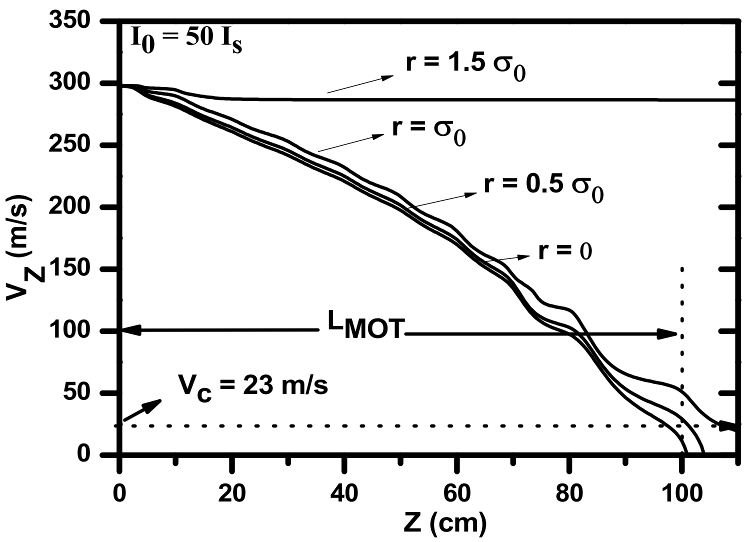

Fig. 4.3: The theoretically calculated variation in the speed of the atoms along the axial distance (z) of the Zeeman slower for a Gaussian slower beam $I_{zs}(r) = I_0 \exp(-2r^2/\rho_0^2)$. Here,

I_0: peak intensity, ρ_0: beam waist radius, I_s: saturation intensity, V_c: capture velocity, L_{MOT}: distance of the boundary of the MOT trapping region from the Zeeman slower entrance.

The overlapping of the MOT beams forms the trapping region. For an atom approaching the trap to be finally cooled and trapped, it is important that its longitudinal velocity at the entry point of the trapping region should be smaller than the capture velocity $V_c = \sqrt{\frac{\hbar \Gamma l}{2m}}$ of the MOT, where m is the mass of the atom and l is the radius of the trap [8]. For a Gaussian Zeeman slower beam, the calculated variation in the longitudinal velocity of the atom with distance z is shown in Fig. 4.3. It is evident from the Fig. 4.3 that, the final longitudinal velocity of the atom depends on its transverse position. For an atom moving with initial longitudinal velocity of ~ 300 m/s (at z = 0) along the atomic beam axis (i.e. r = 0), opposite to a Gaussian Zeeman slower beam with peak intensity $I_0 = 50\ I_s$, the final velocity of the atom at $z = L_{MOT}$ (i.e. at the boundary of MOT trapping region) reduces to lower than the capture velocity of the MOT (V_c = 23 m/s). However, the final longitudinal velocity remains significantly larger than V_c , if atom is positioned at a transverse distance $r = \rho_0$. This clearly shows that atoms moving off-axis are not cooled to a velocity lower than V_c by a Gaussian profile Zeeman slower beam. An increase in power in the Gaussian beam for the effective cooling of the off-axis atoms is expected to lead to the destruction of a MOT. Therefore, the preferential increase in the off-axis intensity in the Zeeman slower beam was considered. This was implemented by using multiple hollow beams of different dark diameter for the Zeeman slower cooling. This helps to keep the high off-axis intensity in the Zeeman slower beam for effective cooling of atomic beam, along with the low on-axis intensity for less destruction of the on-axis MOT cloud.

The longitudinal velocity of atoms in the atomic beam was measured using the method discussed in chapter 2. As discussed Fig. 2.14 (a) shows the schematic of the experimental setup used for the measurement of the velocity of $^{84}Kr^*$ atoms by light induced fluorescence method. Fig. 2.14 (b) shows the longitudinal velocity profile of the slowed atomic beam after the Zeeman slower. The position of the peak in the signal in this figure is used to estimate the longitudinal velocity of the atoms at the exit of the Zeeman slower. This width in the velocity profile is due to several reasons, which include the spatial variation in the slowing laser beam intensity and variation in the magnetic field of the Zeeman slower [9]. In the experiments, the number of atoms accumulated in the MOT was estimated by the fluorescence imaging method after collecting the fluorescence from the MOT cloud on a CCD camera [10-11]. Also, the hollow beam (HB2) diameter was varied by varying the separation between the axicon lenses.

4.3 Results and discussion

The role of the transverse intensity profile of the Zeeman slower laser beam was investigated on the MOT loading by first using HB1 beam as a Zeeman slower beam and observing the number of atoms in the MOT. The number in the MOT was maximized by varying the size of the dark spot in this beam (HB1) at fixed input beam power of 30 mW. As shown in the Fig. 4.4, the maximum number was obtained with dark spot of 1 mm size. This size of the dark spot was used in further experiments with HB1 beam. Fig. 4.5 shows the comparison of performance of a Gaussian and a hollow laser beam (HB1) used in the Zeeman slower. For data shown in Fig. 4.5, the power in the Gaussian beam was measured before the entrance of the chamber. For the exact comparison with the Gaussian beam, the power in HB1 was also measured at the same place (i. e. after the dark spot position). The use of HB1 as the Zeeman slower laser beam always resulted in the higher number of atoms in the MOT than the number obtained with the Gaussian profile slower laser beam (Fig. 4.5, curves (a) and (b)). This observation is qualitatively similar to the one reported by Miranda et al [4]. However, the enhancement factor reported in ref. [4] is much higher than that observed by us. This could be possibly due to much higher flux of atoms used by them for MOT loading with ground state alkali Na atoms. Kr*-MOT was loaded from the metastable Kr atoms with much smaller flux than the flux used for alkali Na atoms.

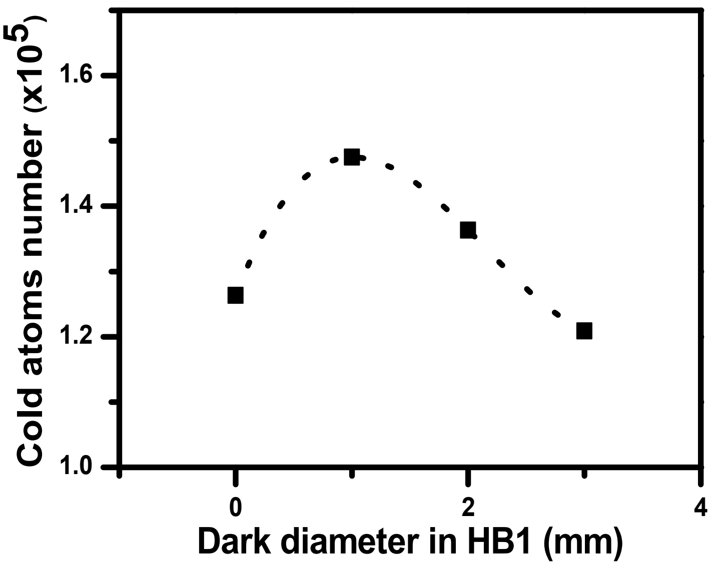

Fig. 4.4: Measured variation in the cold atom number in the MOT with the dark spot diameter of the hollow beam HB1. The dotted line is guide to the eye.

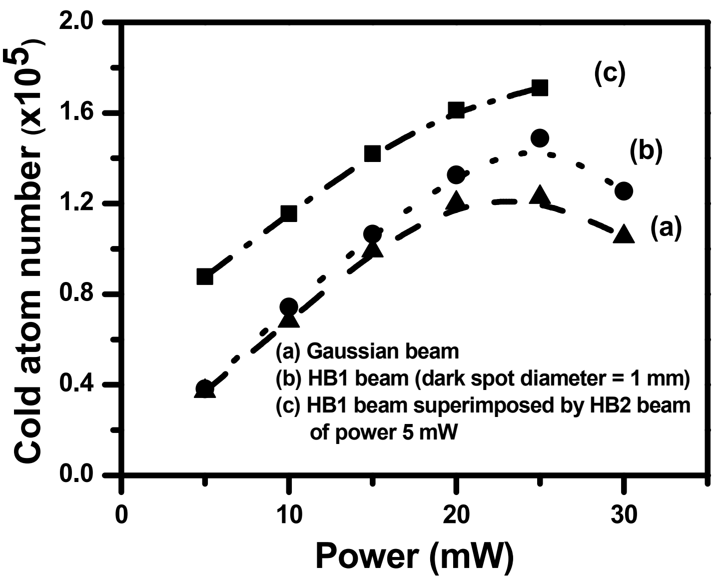

Fig. 4.5 The measured variation in the cold atom number in the MOT with the power of the Zeeman slower laser beam. The curve (a) was for power in the Gaussian beam and the curves

(b) and (c) were for the power of the hollow beam HB1. The curves (c) shows the variation in the number with the power in HB1 beam in presence of the HB2 beam of 5 mW power. The powers in HB1 and HB2 were measured before their entrance into the MOT chamber. The dashed lines are guide to the eye.

The variation in the speed of the atoms along the axial distance (z) of the Zeeman slower for a Gaussian slower beam $I_{zs}(r) = I_0 \exp(-2r^2/\rho_0^2)$ was theoretically calculated as shown in Fig. 4.3. Motivated with the theoretical calculation shown in Fig. 4.3, an additional larger dark diameter hollow beam (HB2, as indicated in Fig. 4.1) was used in presence of HB1 Zeeman slower beam and measured the number of metastable Kr atoms in the MOT. Fig. 4.5 (curve (c)) shows that with this additional beam, i.e. HB2 superimposed on HB1 beam (of 1 mm dark diameter), the observed number of atoms in the MOT was higher than the number obtained with the single Zeeman slower beam HB1. This observed enhancement in the number of atoms in the MOT (curve (b) and curve (c) in Fig. 4.5) is attributed to more efficient cooling of the off-axis atoms in the atomic beam due to the superposition of the HB2 beam. The enhancement can be further improved by increasing the power in the HB2, which was limited to 5 mW in the present experiments due to sharing of total power in HB1 and HB2 beams. The power and the diameter of the second hollow beam (HB2) was kept constant (power: 5 mW, inner diameter: 7 mm, outer diameter: 10 mm) for the measurements shown in Fig. 4.5. This size of HB2 was chosen after optimization of the number of atoms in the MOT with diameter of HB2 at 5 mW power (as shown in Fig. 4.6). It can be noted from Fig. 4.6 that by increasing the ring width of the HB2 beam around the optimum value of the HB2 dark diameter, the number of trapped atoms can be further increased. The improvement in the number of atoms in the MOT due to modification in the Zeeman slower beam intensity profile can be due to both effects, i.e. less destruction of MOT cloud as well as increased flux of slowed atoms for the MOT loading.

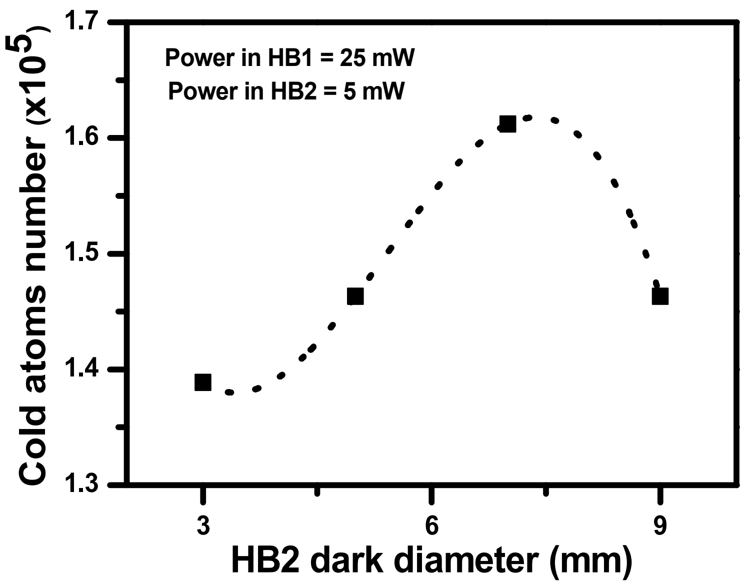

Fig. 4.6 The measured variation in cold atoms in the MOT with the HB2 dark diameter in the final Zeeman slower beam (HB1+HB2) for 25 mW & 5 mW powers in HB1 and HB2 beams respectively. The dotted line is guide to the eye.

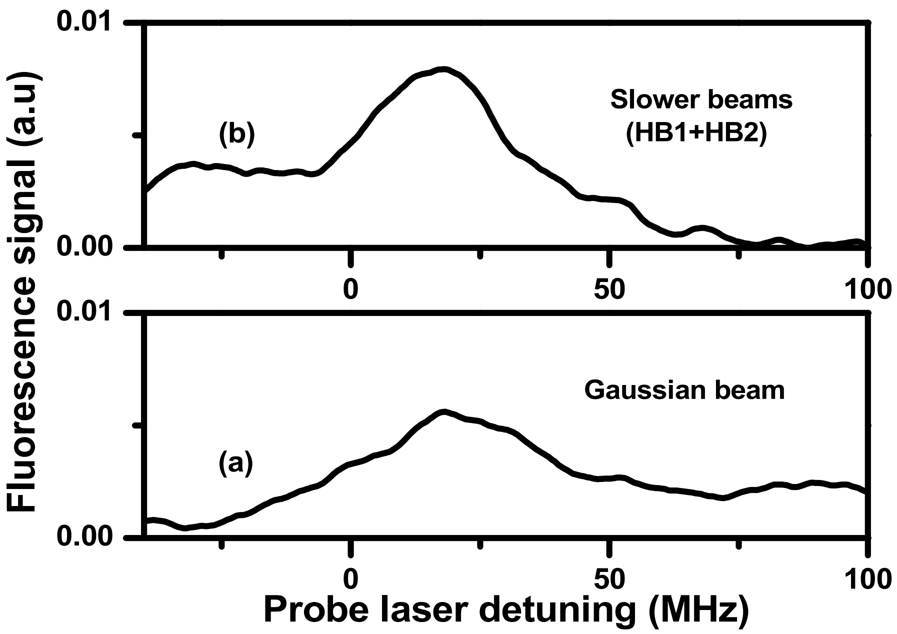

Fig. 4.7 The fluorescence signals due to the 45^0 probe beam (i.e. probe 2) alone as a function of the probe laser beam detuning; curve (a) is for a Gaussian profile of the slower laser beam

of 30 mW power, and curve (b) is for a combination of hollow slower beams (HB1+HB2) with 25 mW and 5 mW power in HB1 and HB2 respectively.

To confirm the effect of the Zeeman slower laser beam profile on the flux of the slowed atomic beam, the flux with hollow Zeeman slower beams was examined by measuring the fluorescence signal from the atomic beam. For this, the fluorescence signals due to probe laser beam at 45^0 (probe 2) were recorded for the Gaussian laser beam as well as for the hollow laser beams (HB1+HB2) used in the Zeeman slower. The results were compared and shown in Fig. 4.7. The curve (a) in Fig. 4.7 shows the fluorescence signals for the Gaussian Zeeman slower beam having power 30 mW, and curve (b) shows the fluorescence signal with the hollow slower beams (HB1+HB2) with powers 25 mW and 5 mW respectively in HB1 and HB2. The results evidently show that a higher flux is obtained with the hollow beams used in the Zeeman slower than that obtained with a Gaussian beam of same total power.

The investigation of the loading behaviour of the Kr-MOT with the Zeeman slower beam power is important to optimize the Zeeman slower parameters for enhanced loading of MOT. The loading characteristics of a MOT depends upon various parameters including cold collisions. The collisional losses in the MOT arise due to the collision between trapped atoms as well as collisions of trapped atoms with the background atoms. These losses were measured by studying the transient loading of the atoms in the MOT. This study was performed using the above mentioned hollow Zeeman slower laser beams. The experimental results presented here show that the Zeeman slower beam was able to modulate the collisional losses due to background atoms and the trapped atom collisions, while losses due to cold atoms collisions in the MOT were unaffected. In order to investigate the role of Zeeman slower laser beam intensity on the background and cold collision rate coefficients, the loading curves of the MOT for different values of Zeeman slower beam power were investigated. Loading curves for different values of the Zeeman slower beam power were recorded on a sensitive photodiode.

The values of γ and β for the MOT were estimated by fitting Eq. (1.21) to the experimentally observed MOT loading curve of the atoms in the MOT.

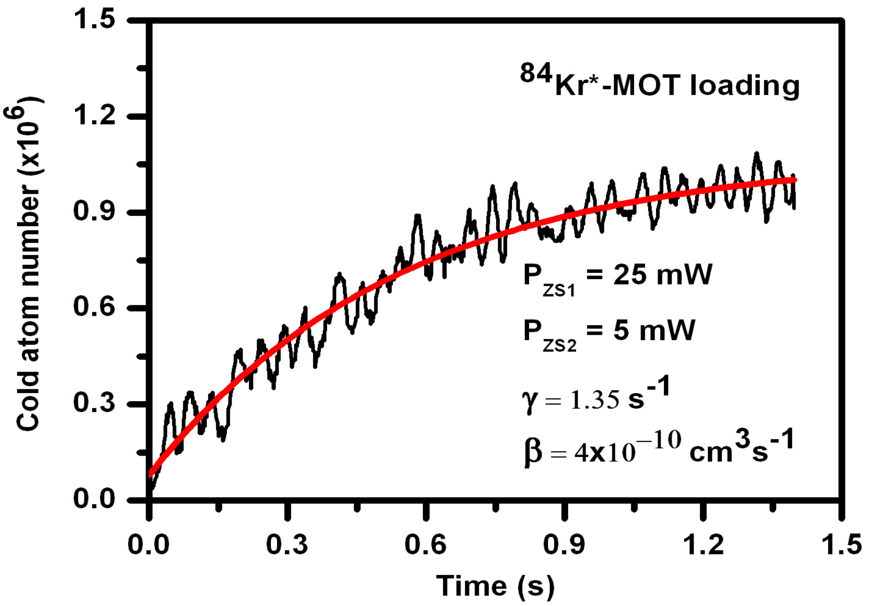

Fig. 4.8: Loading curve of ^{84}Kr*-MOT for Zeeman slower beam powers in the first hollow beam $P_{ZS1} = 25$ mW and second hollow beam $P_{ZS2} = 5$ mW. Solid lines show the fitted curves.

Fig. 4.8 shows the experimentally measured loading curve for ^{84}Kr*-MOT. The values of γ and β for ^{84}Kr*-MOT were estimated by fitting Eq. (1.21) to the experimentally observed MOT loading curve for different values of slower beam power keeping all other trap parameters constant [14-15]. Fig. 4.8 shows the representative MOT loading curve for Zeeman slower beam power ~ 25 mW along with the estimated values of γ and β.

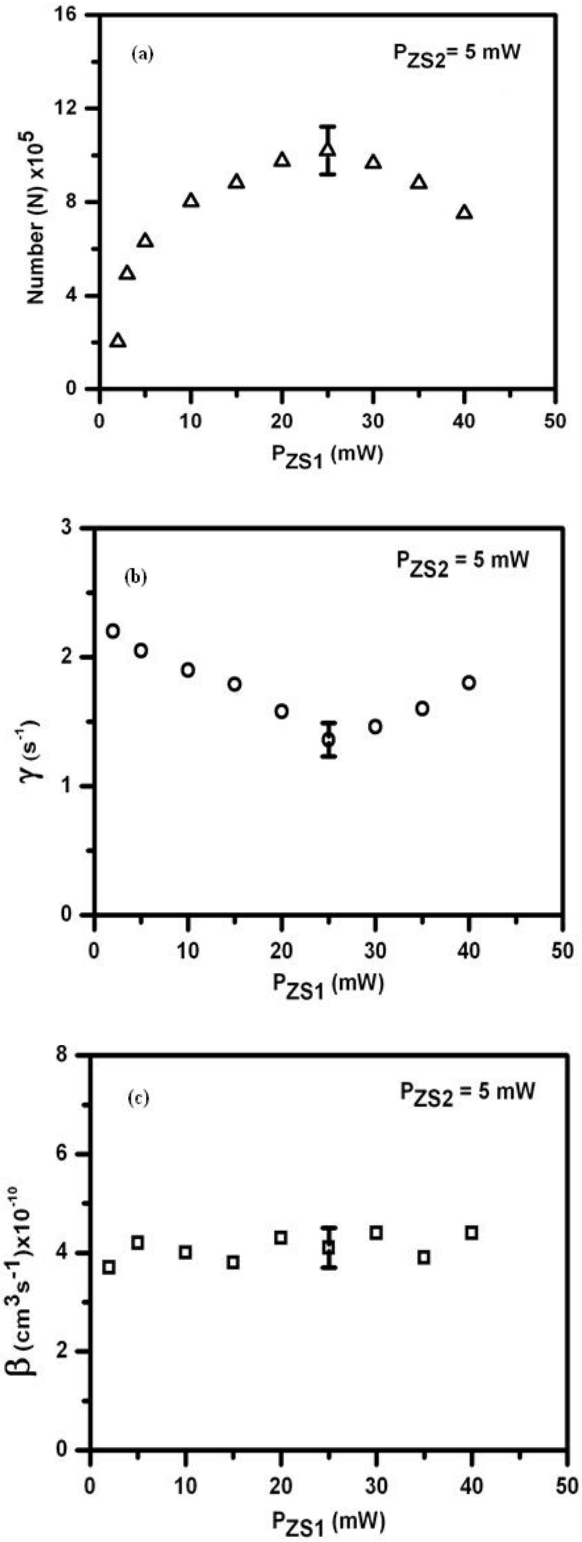

Fig. 4.9 Measured variation in the (a) cold atom number (N), (b) background collision loss rate coefficient γ, (c) cold collision loss rate coefficient β of ^{84}Kr*-MOT with the Zeeman slower beam power (P_{ZS1}). The error bar shown is determined from scatter in the values obtained in the repeated measurements.

Fig. 4.9 (a) shows the Measured variation in the cold atom number (N) of $^{84}Kr^*$ in the MOT with the Zeeman slower beam power (P_{ZS1}). It shows that the number of cold atoms maximizes at certain Zeeman slower beam power. On investigation of loading curve, it was observed that the background collision rate coefficient was minimum (~ 1.35 s-1) at PZS1 = 25 mW as shown in Fig. 4.9 (b). The Zeeman slower beam interacts with the atoms arriving in form of atomic beam around the centre of the trap. This results in reducing the velocity of the background atoms causing lower collisional losses and improvement in number of trapped atoms. The cold collision rate coefficient as shown in Fig. 4.9 (c) remains nearly unchanged to value $4x10^{-10}$ cm^3 s^{-1} as power in the Zeeman slower beam is varied. The lowest value of γ at optimum power of the Zeeman slower beam (~ 25 mW) suggest that the atoms in the Kr* beam attain the lowest speed at this power of the Zeeman slower beam. The Zeeman slower beam slow down these atoms within the capture range of the trap. This results into lower collisional losses and improvement in number of trapped atoms.

4.4 Conclusion

In summary, a significant enhancement in the number of cold atoms in an atomic-beam-loaded magneto-optical trap (MOT) for metastable Krypton atoms was observed, when hollow laser beams were used in the Zeeman slower instead of a Gaussian laser beam. In the Zeeman slower setup, a combination of two hollow laser beams, i.e. a variable diameter hollow beam generated using a pair of axicon lenses superimposed on a fixed diameter hollow beam, was used to reduce the longitudinal velocity of the atoms in the atomic beam below the capture speed of the MOT. The observed enhancement in the number of atoms in the MOT is attributed to reduced destruction of atomic cloud in the MOT and increased cooling of the off-axis atoms in the atomic beam, resulting from the use of hollow beams in the Zeeman slower. The loading behaviour of Krypton magneto optical trap with variation in the Zeeman slower beam was also investigated. Results show that the Zeeman slower beam was able to modulate background collisions whereas cold collisions within the trap were nearly unaffected. This study can be useful to optimize Zeeman slower parameters for enhanced loading of the MOT.

References:

1. C. Y. Chen, K. Bailey, Y. M. Li, T. P. O'Connor, Z. -T Lu, X. Du, L. Young and G. Winker, Rev. Sci. Instrum. **72,** 271 (2001).
2. J. Welte, F. Ritterbusch, I. Steinke, M. Henrich, W. Aeschbach-Hetig and M. K. Oberthaler, New J. Phys. **12,** 065031 (2010).
3. W. D. Phillips and H. Metcalf, Phys. Rev. Lett. **48**, 596 (1982).
4. S. G. Miranda, S. R. Muniz, G. D. Telles, L. G. Marcassa, K. Helmerson and V. S. Bagneto, Phys. Rev. A **59**, 882 (1999).
5. R. L. Cavasso filho, D. A. Manoel, D. R. Ortega, A. Scalabrin, D. Pereira, F. C. Cruz, Appl. Phys. B **78**, 49 (2014)
6. I. Golub and R. Tremblay, J. Opt. Soc. Am. B **7,** 1264 (1990).
7. S. K. Tiwari, S. R. Mishra, S. P. Ram, and H. S. Rawat, Appl. Opt. **51**, 3718 (2012)
8. A. M. Steane, M. Chowdhury and C. J. Foot, J. Opt. Soc. Am. B **9**, 2142 (1992).
9. P. N. Melentiev, P. A. Borisov and P. A. Balykin, J. Exp. Theo. Phys. **98**, 667 (2004).
10. V. B. Tiwari, S. Singh**,** H. S. Rawat and S. C. Mehendale, Phys. Rev. A **78**, 063421 (2008).
11. S. R. Mishra, S. P. Ram, S. K.Tiwari and S. C. Mehendale, Phys. Rev. A **77**, 065402 (2008).
12. S. G. Miranda, S. R. Muniz, G. D. Telles, L. G. Marcassa, K. Helmerson and V. S. Bagneto, Phys. Rev. A **59**, 882 (1999).
13. S. Singh, V. B. Tiwari, S. R. Mishra and H. S. Rawat, J. Exp. Theo. Phys. **119**(3), 406(2014).
14. H. C. Busch , M. K. Shaffer, E. M. Ahmed, and C. I. Sukenik, Phys. Rev. A **73** 023406 (2006).

15 S. Singh, V. B. Tiwari, Y. B. Kale, S. R. Mishra and H. S. Rawat, J. Phys. B: At. Mol. Opt. Phys.**48,** 175302(2015).

Chapter 5

Cold collision studies in two isotope MOT for ^{84}Kr*- ^{86}Kr* atoms

5.1 Introduction

In this chapter, the collision study on cold mixture of metastable ^{84}Kr (^{84}Kr*) and metastable ^{86}Kr (^{86}Kr*) atoms is presented. The cold mixture of atoms was produced in the two isotopes magneto-optical trap (TIMOT) for ^{84}Kr* and ^{86}Kr* atoms. In this TIMOT two cooling laser beams with appropriate wavelengths for these different isotopes were overlapped in the same region of the magneto-optical trap (MOT). The heteronuclear cold collision loss rates have been experimentally measured for each isotope due to the presence of cold atoms of other isotope using the TIMOT loading curves. The dependence of the heteronuclear cold collision loss rate on cooling laser beams intensity has also been studied and compared with homonuclear cold collision loss rate. These studies are useful for the production of short range heteronuclear cold Krypton molecules, using photoassociation spectroscopy

The inter-atomic interactions occurring in a MOT, either in the absence or in presence of near resonant light, manifest in the form of cold atom collisions [1]. The cold atom collisions generally refer to the case when colliding atoms have de Broglie wavelength comparable or larger than the range of the inter-atomic potential [2]. As a result, only few partial waves contribute to the collision cross section. Further, the cold collisions (either elastic or inelastic) may involve two similar (homonuclear) or dissimilar (heteronuclear) atoms. The collision dynamics is different in the case of homonuclear and heteronuclear cold collisions. The homonuclear cold collisions are characterized by a long range ($\sim 1/R^3$) resonant dipole-dipole interaction potential whereas heteronuclear cold collisions are characterized by a short range ($\sim 1/R^6$) van der Waals type potential, with R being the inter-atomic separation [2]. The homonuclear cold collisions have been extensively studied and used to generate a reliable source of cold molecules [3]. Using a near resonant light in noble gas atoms, optical shielding effect [2] and photo-associative effect [4] have been studied. Recently, the study of heteronuclear cold collisions has shown promise in the production of polar molecules with applications in chemistry, metrology and quantum physics [5-7]. The experimental studies performed on heteronuclear cold collisions so far has involved isotopic mixtures of same species of alkali metals, such as ^{85}Rb-^{87}Rb [8] or ^{84}Rb-^{87}Rb [9], as well as inter-species mixtures of alkali metals such as K-Rb [10], Na-Rb [11] and Rb-Cs [12]. Another interesting inter-species cold atomic mixture is produced by simultaneously cooling and trapping of the alkali metal and metastable state noble gas atoms, such as Rb-Ar* mixture [13-14] or Rb-He* mixture [15]. The large amount of internal energy of the metastable noble gas atoms (several eV) as compared to the low kinetic energy of the laser cooled atoms (~ 10^{-8} eV) makes it interesting to study inter-species ionizing collisions and excited state reaction products [16-18]. The high value of internal energy associated with metastable noble gas (Ng*) atoms in the MOT, leads to two-body loss process known as penning ionization ($Ng^* + Ng^* \rightarrow Ng^+ + Ng + e^-$) and associative ionization ($Ng^* + Ng^* \rightarrow Ng_2^+ + e^-$) which can strongly affect the trap densities and lifetimes. Penning ionization due to optically assisted heteronuclear collisions in a MOT is expected to be less important as compared to the homonuclear case [3]. This is due to the reason that in case of the heteronuclear collisions, the interactions are short range van der Waals type as compared to the long range resonant dipole-dipole interaction in case of homonuclear collisions. The experiment was performed to measure loss rates due to cold collisions between two isotopes of Krypton in metastable state (^{84}Kr* and ^{86}Kr*) using a (TIMOT). Similar TIMOT setup has been used earlier to study cold collision in isotopes of He [19] and Ne [20]. This TIMOT setup was utilized to measure heteronuclear trap loss rate coefficients for each isotope due to the presence of the other as a function of cooling laser beam intensity.

5.2 Trap loss in Krypton two isotope MOT

The light assisted collision in presence of near resonant light in a MOT contributes significantly to the trap loss process [2]. However, the increase in the trap depth with the increase in the intensity of the laser prohibits the process. These two competitive processes make the trap loss rate intensity dependent. The losses in the MOT arise due to collisions between the cold trapped atoms and collisions between the trapped and background atoms. These losses were measured by studying the transient loading or decay of the atoms in the MOT. The cold collision loss rate coefficient β for single isotope Kr*-MOT has been estimated by Katori et al [21]. However, here, the aim of the experiment was to estimate heteronuclear collision loss rate coefficient $\beta_{^{84}Kr^*-^{86}Kr^*}$ in the ^{84}Kr*-^{86}Kr* TIMOT.

The temporal evolution of the number of cold atoms for the first isotope (N_1) in presence of second isotope in a TIMOT is given by [14]

$$\frac{dN_1(t)}{dt} = L_1 - \gamma_1 N_1(t) - \beta_1 \int_V n_1^2(r,t) d^3r - \beta_{12} \int_V n_1(r,t) n_2(r,t) d^3r, \tag{5.1}$$

where L_1 is the MOT loading rate, γ_1 is the background collision loss rate coefficient for the first isotope (i. e ^{84}Kr*), $n_1(r,t)$ is the cold atoms number density of first isotope, $n_2(r,t)$ is the cold atoms number density of second isotope (^{86}Kr*), β_1 (i.e $\beta_{^{84}Kr^*}$) is the cold collision loss rate coefficient due to collision between two cold ^{84}Kr* atoms in the trap and β_{12} ($\beta_{^{84}Kr^*-^{86}Kr^*}$) is the cold collision loss rate coefficient for cold ^{84}Kr* in presence of trapped cold ^{86}Kr* atoms. Three body collisions are insignificant in this low density ($\sim 10^8$ cm^{-3}) Kr*-MOT and hence not considered in the loading Eq. (5.1).

The number density (n_i) distribution of the cold atoms for any isotope in constant volume regime is approximated to a Gaussian distribution as

$$n_i(r,t) = n_{0i}(t)e^{-r^2/2\rho_i^{\,2}} \text{ for } (i = 1 \text{ for } ^{84}\text{Kr* and 2 for } ^{86}\text{Kr*}), \tag{5.2}$$

where ρ_i is the rms radius of the atomic cloud for a given isotope. The loading behaviour for the single isotope can be estimated from the general Eq. (5.1) by substituting n_2 = 0. The solution of Eq. (5.1) for this case is given as,

$$N_1(t) = N_{1s}\left[1 - \frac{(1+\xi_1)\exp(-t/t_{L1})}{1+\xi_1\exp(-t/t_{L1})}\right], \tag{5.3}$$

where $$t_{L1} = \left[\frac{(1-\xi_1)}{(1+\xi_1)}\frac{1}{\gamma_1}\right],\ \xi_1 = \left[1+\sqrt{8}\frac{\gamma_1}{\beta_1 n_{01s}}\right]^{-1}.$$

Here, N_{1s} and n_{01s} are the steady state cold atom number and the steady state peak number density of first isotope MOT cloud respectively. The values of γ_1 and β_1 for the first isotope MOT can be estimated by fitting Eq. (5.3) to the experimentally observed MOT loading curve of that isotope in absence of the MOT cloud of other isotope. Once, γ_1 and β_1 were estimated for MOT of first isotope, the heteronuclear trap loss rate coefficient β_{12} were evaluated from the loading curve of the first isotope MOT in presence of MOT for the second isotope. For this purpose Eq. (5.1) was integrated over the trap volumes by using number density distribution given by Eq. (5.2) to obtain the following equation for MOT loading.

$$\frac{dN_1(t)}{dt} = L_1 - \gamma_1 N_1(t) - \frac{\beta_1 N_1^2(t)}{\rho_1^3\pi^{3/2}} - \beta_{12}N_1(t)N_2(t)\left[\frac{2}{\pi\left(\rho_1^2+\rho_2^2\right)}\right]^{3/2}, \tag{5.4}$$

where, ρ_1 and ρ_2 are the rms width of each isotope MOT cloud. Here, $N_1(t)$ and $N_2(t)$ are the time dependent number of atoms for first and second isotopes in the TIMOT.

The coefficient β_{12} was determined by observing the steady-state number of atoms in the MOT for first isotope in absence and in presence of MOT cloud for second isotope. The steady-state number of cold atoms in the TIMOT was usually smaller than the steady-state number observed in the single isotope MOT cloud. In steady state condition, Eq. (5.4) leads to

$$\beta_{12}=\left[\pi\left(\frac{\rho_1'^2+\rho_2'^2}{2}\right)\right]^{3/2}\frac{1}{N_{1s}'N_{2s}'}\times\left\{\gamma\left(N_{1s}-N_{1s}'\right)+\beta_1\left[N_{1s}^2\left(\frac{1}{\pi\rho_1^2}\right)^{3/2}-N_{1s}'^2\left(\frac{1}{\pi\rho_1'^2}\right)^{3/2}\right]\right\}, \tag{5.5}$$

where N_{1s}' and ρ_1' are the steady state number and the rms width of the first isotope MOT cloud in presence of the second isotope MOT cloud. N_{2s}' and ρ_2' are the steady state number and the rms width of the second isotope MOT cloud in presence of the first isotope MOT cloud. Using similar methodology for the second isotope (i.e ^{86}Kr*), background collision loss rate coefficient γ_2 , and cold collision loss rate coefficients β_2 (i.e $\beta_{^{86}Kr*}$) and β_{21} (i.e $\beta_{^{86}Kr*\_^{84}Kr*}$) was evaluated.

5.3 Experimental setup:

The experimental setup for the TIMOT for Krypton isotopes ^{84}Kr and ^{86}Kr has been developed in-house whose schematic diagram is shown in Fig. 5.1. The vacuum setup for the TIMOT is similar to that used in the earlier reported work [22, 23] and is also discussed in detail in chapter 3.

The TIMOT is loaded from a slow atomic beam of metastable state Kr (^{84}Kr* & ^{86}Kr*) atoms. This atomic beam is formed when the Kr gas flows through a RF discharge tube, a collimator tube and a Zeeman slower to the MOT chamber, which is all maintained at different pressure values. The optimal loading rate and the number of atoms in the TIMOT for ^{84}Kr* and ^{86}Kr* are achieved when the cooling lasers are appropriately detuned with respect to the cooling transitions of the corresponding isotopes.

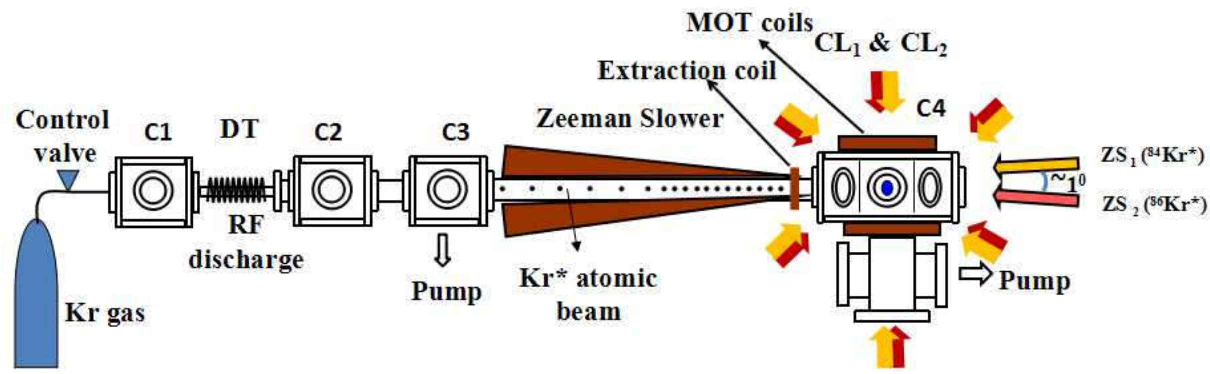

Fig. 5.1: Schematic of the experimental setup of two isotope magneto-optical trap (TIMOT) for cooling and trapping of ^{84}Kr* and ^{86}Kr* atoms. C1, C2, C3 and C4 are different vacuum chambers known as gas inlet chamber, analysis chamber, pumping chamber and MOT chamber respectively. DT is the discharge tube. CL_1 and CL_2 are the cooling beams corresponding to ^{84}Kr* and ^{86}Kr* isotopes respectively. ZS_1 and ZS_2 are Zeeman slower beams for ^{84}Kr* and ^{86}Kr* cooling respectively.

As shown in Fig. 5.1, the intense laser beams at two different frequencies are required for the pre-cooling of atomic beam in the Zeeman slower for both the isotopes ^{84}Kr* and ^{86}Kr*. Since these beams can disturb the on-axis MOT clouds of ^{84}Kr* and ^{86}Kr* atoms, the Zeeman slower beams (ZS_1 and ZS_2) for both the isotopes were kept at an angle with respect to the Zeeman slower axis. The angle between the two Zeeman slower beams was ~ 1^0 as shown in Fig. 5.1. All the laser beams used in our experiment were obtained from two extended cavity diode laser (ECDL) systems (Models: DL-110 and TA-Pro, TOPTICA, Germany) with an output power of ~100 mW and ~1W respectively. The lasers were frequency locked for ^{84}Kr* and ^{86}Kr* cooling transitions using the saturated absorption spectroscopy (SAS) in Krypton cells applying RF discharge. Relevant energy levels for the laser cooling of ^{84}Kr* and ^{86}Kr* and saturated absorption spectra are shown in Fig. 5.2 (a) and (b) respectively. It is evident from the Fig. 5.2 (b) that the cooling transition of the ^{86}Kr* is blue shifted by ~ 65 MHz with respect to cooling transition of the ^{84}Kr*.

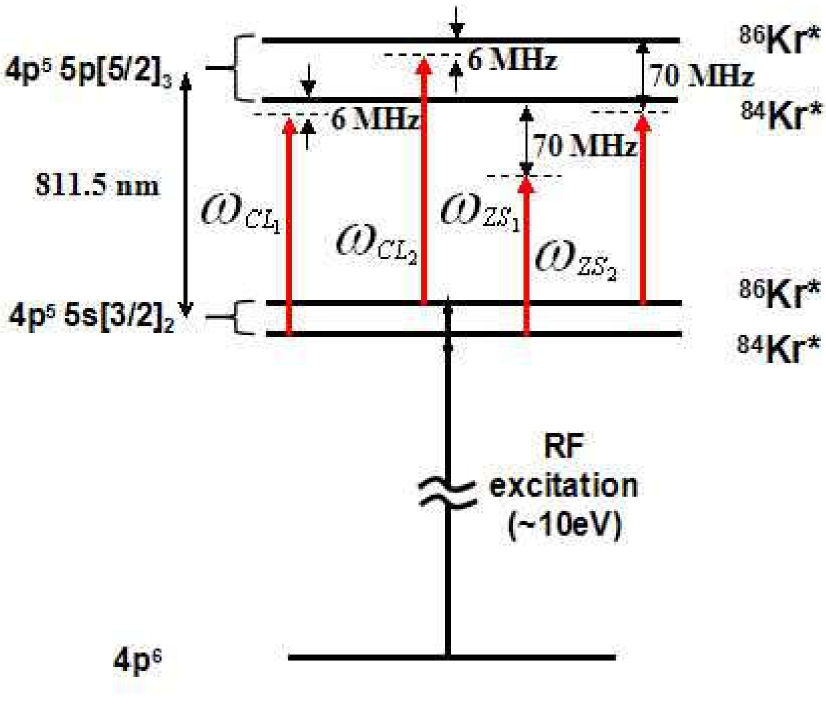

(a)

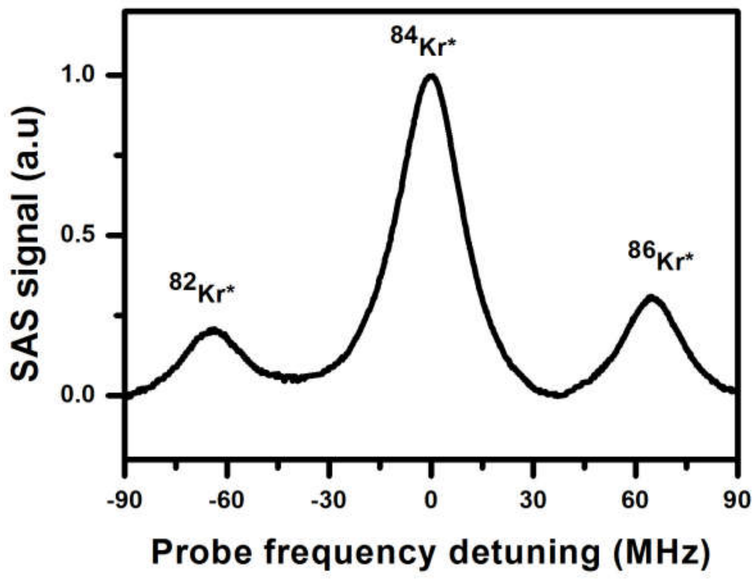

(b)

Fig. 5.2: (a) Relevant energy levels for laser cooling of ^{84}Kr* and ^{86}Kr* in TIMOT. Here ω_{CL_1}, ω_{CL_2}, ω_{ZS_1} and ω_{ZS_2} denote the frequencies of cooling and Zeeman slower lasers for ^{84}Kr* and ^{86}Kr* isotopes. (b) A typical saturated absorption spectroscopy (SAS) signal obtained for frequency locking of cooling and Zeeman slower lasers.

The cooling laser beams CL_1 and CL_2 for two isotopes ^{84}Kr* and ^{86}Kr* was generated from the 100 mW ECDL-1 after using zeroth order (for ^{84}Kr*) and first order (+65 MHz, for ^{86}Kr*) diffracted beams from an accousto-optic modulator (AOM) denoted as AOM 1 in Fig. 5.3 (a). These beams were kept ~ 6 MHz red-detuned from the cooling transitions of ^{84}Kr* and ^{86}Kr* respectively by locking the ECDL-1 at ~ 6 MHz red-detuned side of ^{84}Kr* transition peak using the SAS setup. Each of the cooling beams was split into three beams which enter the MOT chamber. Before entry into the MOT chamber (C4), each of the three laser beams for ^{84}Kr* cooling had a power of ~ 0.6 mW whereas each of three beams for ^{86}Kr* cooling had power of ~ 1.8 mW. The second MOT (^{86}Kr*-MOT) was operated with higher laser power to equalize the trapped numbers of ^{86}Kr* and ^{84}Kr* isotopes. The retro-reflection of these beams resulted in desired six MOT beams for the each isotope. Two σ^+ polarized Zeeman slowing laser beams ZS_1 and ZS_2 with ~ 70 MHz red-detuned respectively from the cooling transition of ^{84}Kr* and ^{86}Kr* were generated using two AOMs (AOM 2 and AOM 3) as shown in Fig. 5.3(b). This was achieved by locking the ECDL-2 at ~10 MHz blue-detuned side of ^{84}Kr* transition peak using the SAS setup (Fig. 5.3(b)) and operating AOM 2 and AOM 3 at -80 MHz and +65 MHz respectively. The $1/e^2$ radius of the cooling as well as Zeeman slower beams was kept ~3 mm. The quadrupole magnetic field for the MOT had an axial field gradient of ~ 10 G/cm. A photodiode and a CCD camera were used to monitor the number of atoms and the size of the MOT cloud. The number in the MOT was estimated by collecting fluorescence from the MOT cloud onto a calibrated photodiode. The transient probe absorption technique [24, 25] was used here to measure the temperature of the atomic cloud for each isotope in the TIMOT setup.

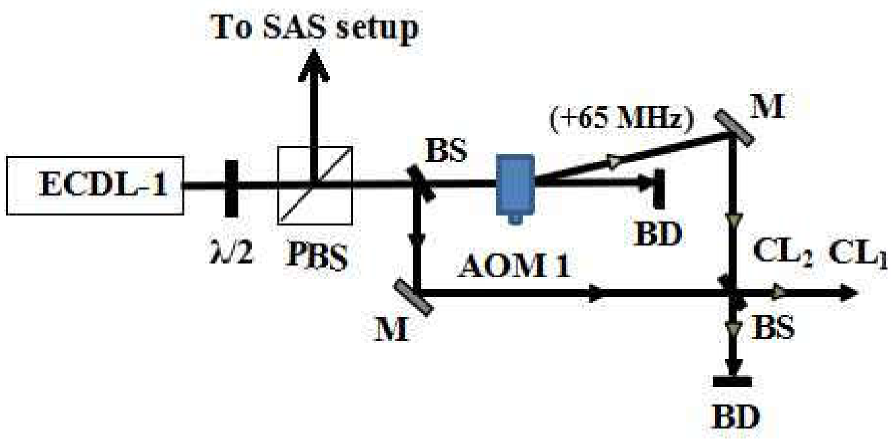

(a)

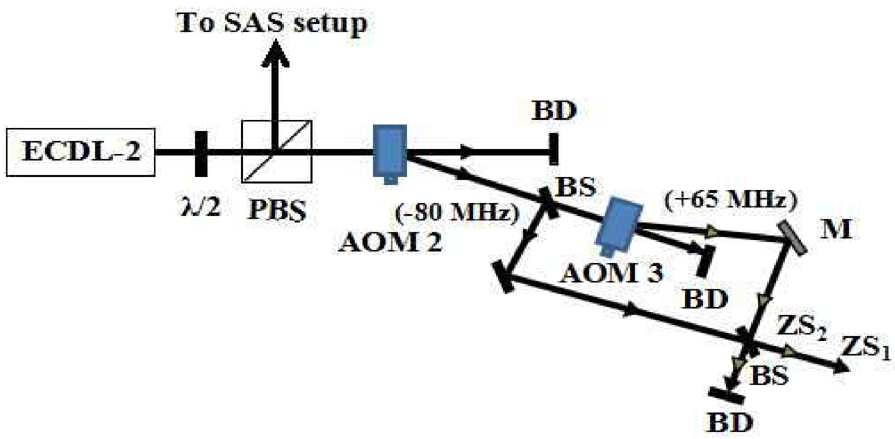

(b)

Fig. 5.3: (a) Schematic of optical layout for generation of cooling beams for ^{84}Kr*and ^{86}Kr* isotopes. (b) Schematic of optical layout for generation of Zeeman slower beams for ^{84}Kr* and ^{86}Kr*. ECDL-1 and ECDL-2: Extended cavity semiconductor diode lasers for cooling and Zeeman slower purpose, SAS setup: saturated absorption spectroscopy setup, PBS: polarizing beam splitter cube, AOM: Acousto-optic modulator, M: reflecting mirror, BS: 50% beam splitter, BD: beam dump.

5.4 Results and discussion

The TIMOT was loaded with two isotopes of Krypton in metastable state (i.e. ^{84}Kr* and ^{86}Kr*) trapped simultaneously in space. The clouds for the two isotopes were spatially separated by slightly misaligning the Zeeman slower beams. Figure 5.4(a) shows the CCD images of these clouds. Figure 5.4(b) shows the probe absorption spectrum of the TIMOT when clouds of the both isotopes ^{84}Kr* and ^{86}Kr* were overlapped. Spatial overlap of both the clouds was confirmed by observing the images from three mutually perpendicular directions.

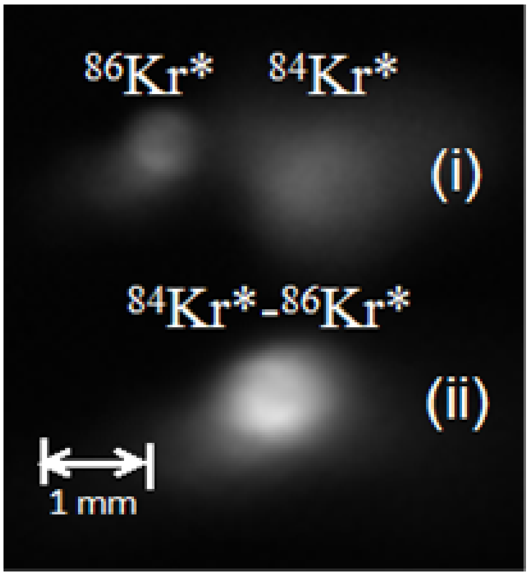

(a)

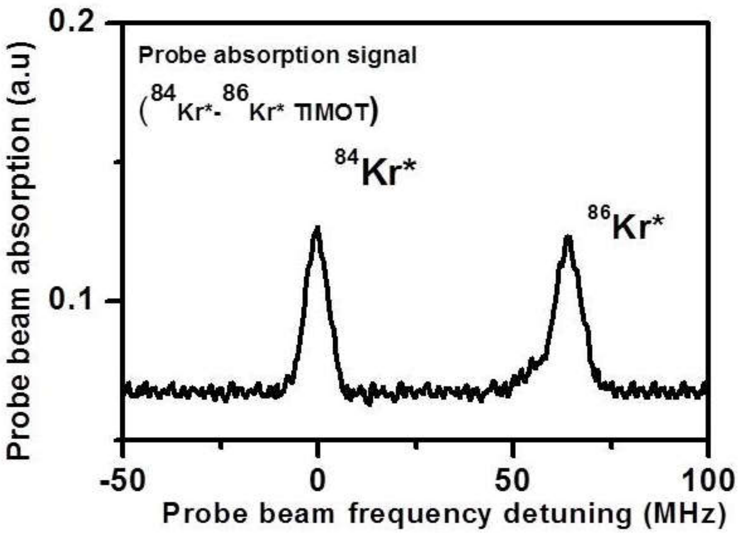

(b)

Fig. 5.4: (a) CCD images of the separated [(i)] and overlapped [(ii)] TIMOT for ^{84}Kr*and ^{86}Kr* atoms. (b) Probe absorption signal from TIMOT with probe frequency detuning.

The temperature of the cold atomic cloud was measured using the transient probe absorption technique. In this temperature measurement technique, a weak resonant probe beam passes through the freely expanding cold atomic cloud and its absorption is measured using the photodiode detector. The probe laser beam having power ~ 25 μW with $1/e^2$ radius of around 200 μm was used for temperature measurement. The change in the probe beam absorption was observed mainly due to the escape of atoms in the transverse direction with respect to the propagation direction of the probe beam. The probe beams push on atoms in the longitudinal direction maintains the atoms in the light field which is expected to have a negligible effect on the change in the absorption signal. The estimated temperature was (360±30) μK for ^{84}Kr* atoms MOT cloud and was (400±30) μK for ^{86}Kr* atoms MOT cloud in the TIMOT setup. The number of atoms for both the isotopes were estimated from the loading curves detected on the photodiode. The MOT parameters were set such that nearly equal number of atoms were trapped for both the isotopes (^{84}Kr* and ^{86}Kr*) in the TIMOT. The measured number of atoms in the MOT cloud with single isotope (in absence of other isotope) was ~ 2.6×10^5 after full loading of the MOT. The steady state number for both the isotopes gets slightly reduced due to increase in the collision loss rate when both the isotopes are trapped simultaneously (Fig. 5.5).

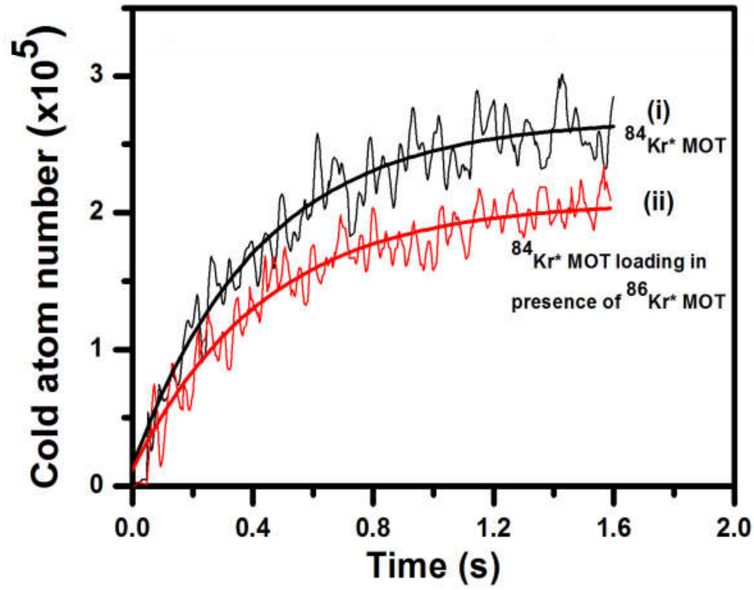

(a)

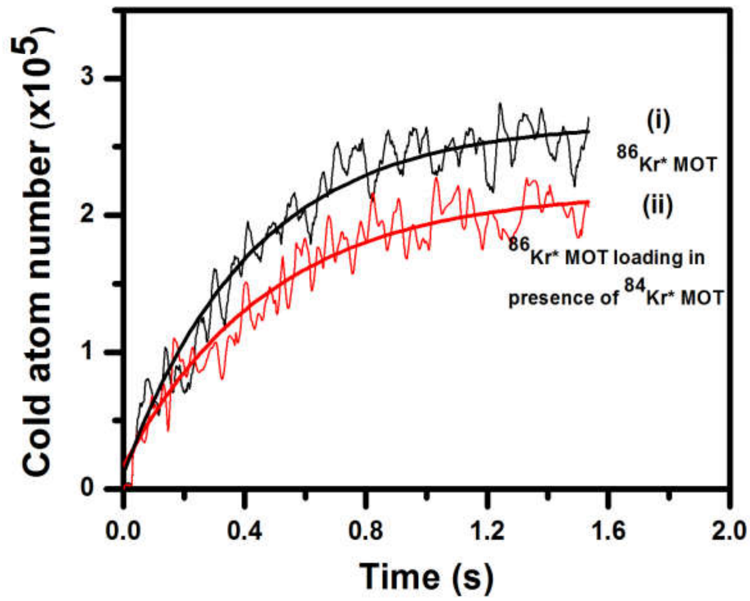

(b)

Fig. 5.5: (a) Loading curves of ^{84}Kr* MOT in absence [(i)] and in presence [(ii)] of ^{86}Kr* MOT. (b) Loading curves of ^{86}Kr* MOT in absence [(i)] and in presence [(ii)] of ^{84}Kr* MOT. Solid lines show the fitted curves.

The curves (i) in Fig. 5.5(a) and 5.5(b) show the MOT loading of each isotope in absence of the other isotope atomic cloud, whereas curves (ii) in these figures show the loading of each isotope in presence of fully loaded MOT of the other isotope. It is evident from these figures (curves (ii)) that there is nearly 25% decrease in the final (steady-state) number of atoms in the MOT of a given isotope due to the presence of atomic cloud of other isotope. From these loading curves, various loss rate parameters were estimated. The curve (i) in Fig. 5.5(a) when fitted with Eq. (5.3) provided the background loss rate coefficient γ_1 ~ (2.1±0.2) s^{-1}, and cold collision loss rate coefficient β_1 = (4.2±0.4) x 10^{-10} cm^3/s for the first isotope. By using Eq. (5.7) and putting the above values of γ_1 and β_1 alongwith the steady state numbers of both the isotope (N_{1s}' and N_{2s}') in presence of each other (derived from curve (ii) in Fig. 5.5(a) and (b)), the heteronuclear collision loss rate coefficient β_{12} was estimated to be (8.7±0.8) x 10^{-10} cm^3/s. Similarly, for the second isotope, the loss parameters were estimated as background loss rate coefficient γ_2 ~ (2.1±0.2) s^{-1}, cold collision loss rate coefficient β_2 = (4.0±0.4) x 10^{-10} cm^3/s and heteronuclear collision loss rate coefficient β_{21} = (8.8±0.8) x 10^{-10} cm^3/s. It is also clear from the experimental results that the heteronuclear collision loss rate coefficient β_{12} is approximately two times compared to the value of homonuclear collision loss rate coefficient β_1.

Fig. 5.6 (a) and 5.6 (b) show the measured variation in $\beta_{^{84}Kr*}$ (β_1) and $\beta_{^{86}Kr*}$ (β_2) with total intensity in MOT beams. As expected, the number of cold atoms is observed to increase with MOT beams intensity. The decrease in cold collision loss rate with increase in the MOT beam intensity appears to be due to increase in the trap depth with the MOT beams intensity.

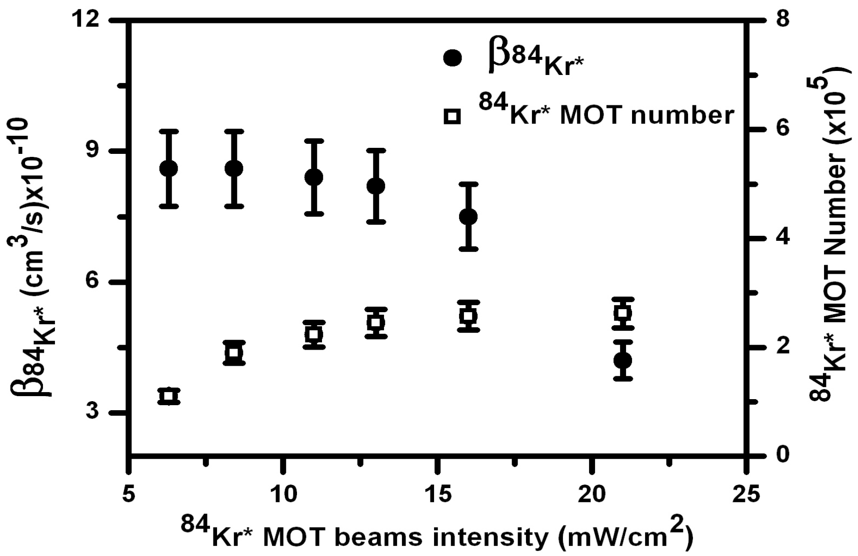

(a)

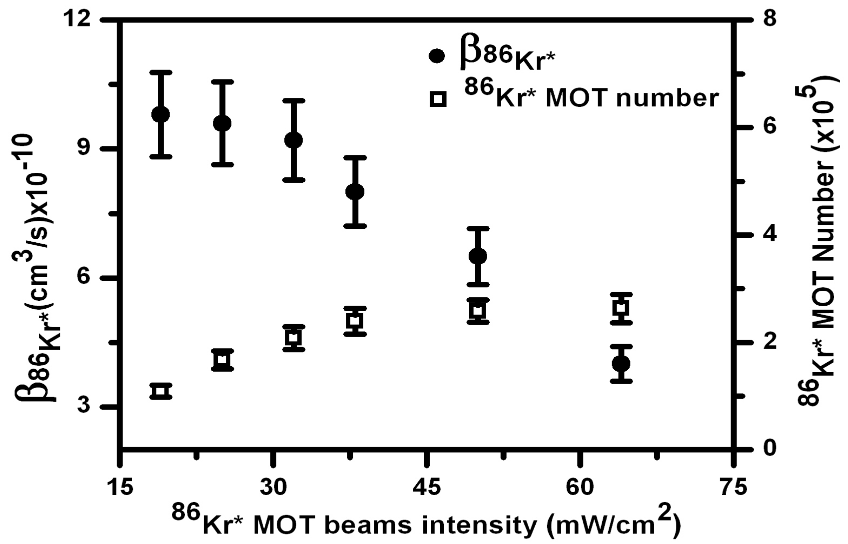

(b)

Fig. 5.6: (a) Measured variation in the number of atoms in ^{84}Kr*-MOT cloud and cold collision loss rate coefficient $\beta_{^{84}Kr^*}$ (i.e β_1) with total intensity used in cooling beams of ^{84}Kr*-MOT. (b) Measured variation in the number of atoms in ^{86}Kr*-MOT cloud and cold collision loss rate coefficient $\beta_{^{86}Kr^*}$ (i.e β_2) with total intensity used in cooling beams of ^{86}Kr*-MOT. The error bars shown are determined from scatter in the values obtained in the repeated measurements.

The dependence of cold collision loss rate coefficients β_{12} and β_{21} on the MOT beams intensity was also studied while keeping the other trap parameters fixed. First, the ^{86}Kr*-MOT laser beams intensity was varied (from 0 to 64 mW/cm^2), while keeping the ^{84}Kr*-MOT laser beams intensity constant (21 mW/cm^2) and β_{12} was.estimated. For different values of intensity of ^{86}Kr*-MOT beams, this value of β_{12} was nearly remain unchanged over the given intensity range as shown in Fig. 5.7 (a). Similarly, the ^{84}Kr*-MOT laser beams intensity from 0 to 21 mW/cm^2 was varied while keeping the ^{86}Kr*-MOT intensity constant (64 mW/cm^2), and β_{21} was estimated. For different values of the intensity of ^{84}Kr*-MOT beams, this value of β_{21} remained nearly unchanged over the given intensity range as shown in Fig. 5.7(b).

The measured values of heteronuclear collision loss rate coefficient β_{12} and its reciprocal value β_{21} in the TIMOT of ^{84}Kr* and ^{86}Kr* atoms were found to be nearly equal. These results show a trend similar to that reported earlier in case of dual species MOT system of alkali metal and metastable state noble gas atoms [14]. However, these results were in contrast to that obtained from the dual species MOT systems involving only alkali-metal atoms where reciprocal values of heteronuclear collision loss rate coefficient were found to be different [7].

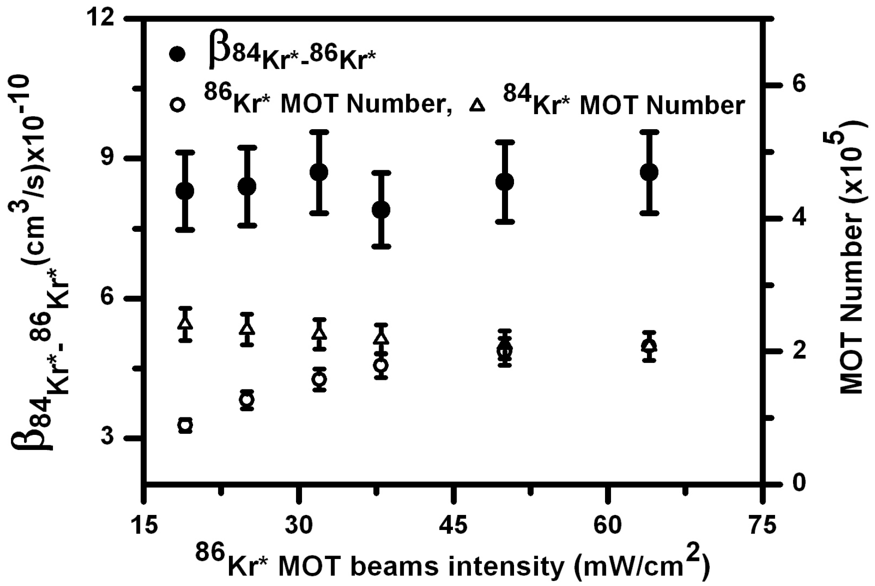

(a)

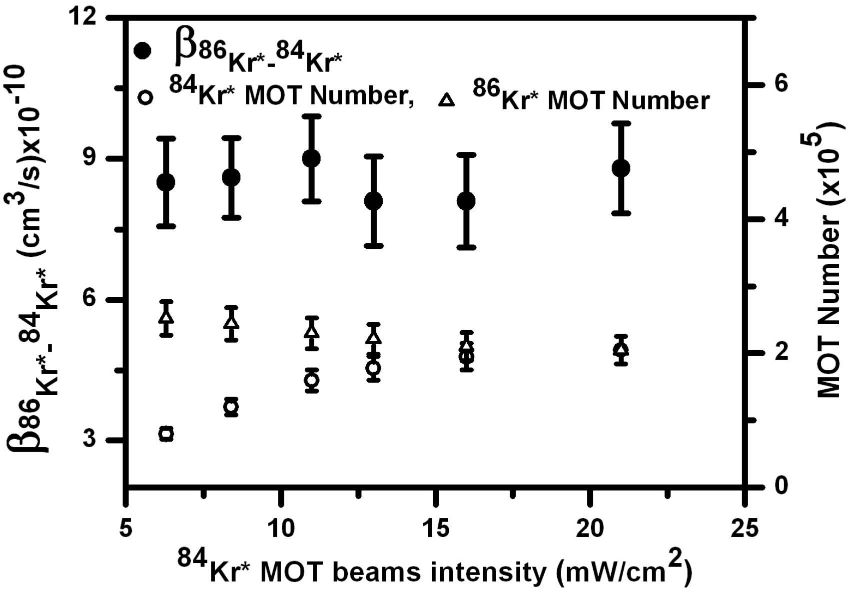

(b)

Fig. 5.7: (a) Measured variation in $\beta_{^{84}Kr^*\_^{86}Kr^*}$ (β_{12}), number of atoms in ^{84}Kr*-MOT and number of atoms in ^{86}Kr*-MOT with total intensity of ^{86}Kr*-MOT beams. (b) Measured variation in $\beta_{^{86}Kr^*\_^{84}Kr^*}$ (β_{21}), number of atoms in ^{86}Kr*-MOT and number of atoms in ^{84}Kr*-MOT with total intensity of ^{84}Kr*-MOT beams. The error bars shown are determined from the scatter in the values obtained in the repeated measurements.

In metastable noble gas atom MOT, the two-body loss rate β is usually dominated by photo-assisted loss processes which include penning ionization, associative ionization and radiative escape processes [3, 14, 26]. The cold collision loss due to penning ionization process is relatively larger than the associative ionization [21] and radiative escape process [26].

In case of heteronuclear collision data (Fig. 5.7), the collisional loss rates are higher than those of homonuclear collision case (Fig. 5.6). This may be due to increase in the photo-associated loss rates in heteronuclear collision case because of more intensity due to presence of both the MOTs (^{84}Kr* and ^{86}Kr*) and the corresponding Zeeman slower beams. Due to this, the loss rates in heteronuclear case may become so strong that the variation in the trap depths due to MOT intensity variation (Fig. 5.7) has no observable effect on $\beta_{12}(or\beta_{21})$ [27].

5.5 Conclusion:

A two isotope magneto-optical trap (TIMOT) was developed for simultaneous cooling and trapping of metastable state ^{84}Kr and ^{86}Kr atoms. The loading characteristics were studied and measured the heteronuclear collision loss rate coefficients for ^{84}Kr* and ^{86}Kr* isotopes. These coefficients have been compared with the homonuclear loss rate coefficients for these isotopes. The heteronuclear collision loss rate coefficient $\beta_{^{84}Kr*\_^{86}Kr*}$ in the presence of MOT light was measured to be approximately two times the value of homonuclear collision loss rate coefficient $\beta_{^{84}Kr*}$. The studies on the homonuclear cold collisions in metastable ^{84}Kr* atoms have been shown to be important and useful in the production of purely-long-range (PLR) Krypton molecules. In view of this, the investigations are expected to be useful for the production of short range heteronuclear cold Krypton molecules.

References:

1. H. J. Metcalf and P. van der Straten, Laser Cooling and Trapping, New York: Springer 1999.

2. J. Weiner , V. S. Bagnato, S. Zilio and P. S. Julienne, Rev. Mod. Phys. **71,** 1(1999).

3. W. Vassen, C. Cohen-Tannoudji, M. Leduc, D. Boiron, C. I. Westbrook, A. Truscott, K. Baldwin, G. Birkl, P. Cancio, and M. Trippenbach, Rev. Mod. Phys. **84,** 175 (2012).

4. K. Shaffer, G. Ranjit and C. I. Sukenik , Phys. Rev. A **83,** 052516 (2011).

5. D. DeMille Phys. Rev. Lett. **88,** 067901 (2002).

6. S. Ospelkaus, K. K. Ni, D. Wang, M. H. Gde Miranda, B. Neyenhuis, G. Quemener, P. S. Julienne, J. L. Bohn, D. S. Jin and J. Ye, Science **327,** 853 (2010).

7. M. W. Mancini, A. R. L.Caires , G. D. Telles, V. S. Bagneto and L. G. Marcassa, Eur. Phys. J. D **30,** 105 (2004).

8. W. Suptitz, G. Wokurka, F. Strauch, P Kohns, and W. Ertmer, Opt. Lett. **19,** 1571 (1994).

9. S. G. Crane, X. Zhao, W. Taylor and D. J. Vieira, Phys. Rev. A **62,** 011402(R) (2000).

10. L. G. Marcassa, G. D. Telles, S. R. Muniz, and V. S. Bagnato, Phys. Rev. A **63**, 013413 (2000).

11. G. D. Telles, L G Marcassa, S. R. Muniz, S. G. Miranda, A. Antunes, Phys. Rev. A **59**, R23 (1999).

12. Zhong-Hua Ji, Ji-Zhou Wu, Hong-Shan Zhang, Teng-Fei Meng, Jie Ma, Li-Rong Wang, Yan-Ting Zhao, Lian-Tuan Xiao and Suo-Tang Jia, J. Phys. B: At. Mol. Opt. Phys. **44,** 025202 (2011).

13. C. I. Sukenik and H. C. Busch, Phys. Rev. A **66,** 051402(R) (2002).

14. H. C. Busch, M. K. Shaffer, E. M. Ahmed, and C. I. Sukenik, Phys. Rev. A **73,** 023406 (2006).

15. L. J. Byron, R. G. Dall and A. G. Truscott, Phys. Rev. A **81,** 013405 (2010).

16. G. Nowak and J. Fricke, J. Phys. B: At. Mol. Opt. Phys. **18,** 1355 (1985).

17. C. R. Menegatti, B. S. Marangoni and L. G. Marcassa, Laser Phys. **18,** 1305 (2008).

18. G. D. Telles, M. W. Mancini, A. R. L. Caires, V. S. Bagnato and L. G. Marcassa, Laser Phys. **13,** 168 (2003).

19. J. M. McNamara, R. J. W. Stas, W. Hogervorst, and W. Vassen, Phys. Rev. A **75**, 062715 (2007).

20. J. Schutz, T. Feldker, H. John, and G. Birkl, Phys. Rev. A. **86**, 022713 (2012).

21. Hidetoshi Katori and Fujio Shimiju, Phys. Rev. Lett. **73**, 2555 (1994).

22. S. Singh, V. B. Tiwari, S. R. Mishra and H. S. Rawat, Laser Phys. **24**, 25501 (2014).

23. S. Singh, V. B. Tiwari, S. R. Mishra and H. S. Rawat, J. Exp. Theo. Phys. **119**, 406 (2014).

24. Xinye Xu, Thomas H Loftus, John L Hall, Allen Gallagher and Jun Y*e,* J. Opt. Soc. Am. B **20**, 968 (2003).

25. R. R. Silva, K. M. F. Magalhaes, E. A. L. Henn, L. G. Marcassa, V. S. Bagneto, Opt. Commun. **265**, 526 (2006).

26. J. J. Tol Paul, Norbert Herschbach, Eric A Hessels , Wim Hogervorst and Wim Vassen, Phys. Rev. A **60**, R761 (1999).

27. S. Singh, V. B. Tiwari, Y. B. Kale, S. R. Mishra and H. S. Rawat, J. Phys. B: At. Mol. Opt. Phys. **48**, 175302 (2015)

Chapter 6

Summary and the future work

Laser cooling and trapping of noble gas (Kr*) atoms in the excited state provides a unique opportunity to study cold atom collisions, ionization physics, nanolithography and atom trap trace analysis (ATTA) [1-5]. The work presented in this thesis, involves the development of a magneto-optical trap (MOT) setup for metastable Krypton (Kr*) atoms to perform experiments on loading and atomic collisions [6]. The setup consists of various vacuum chambers maintained at different pressure values to allow the flow of atoms from the gas inlet chamber to the MOT chamber. The Kr* atoms in the setup are produced in a glass tube using RF-driven discharge at frequency ~ 30 MHz. The Kr atoms are cooled and trapped in the metastable excited state. The generation of metastable Kr (Kr*) atoms is the foremost requirement for the development of the MOT. Once the atoms are excited in the metastable state, they are transported to the MOT chamber to produce a cold atomic cloud. The laser cooling of metastable state Kr atoms requires a wavelength of ~ 811.5 nm to drive the cooling transition between two excited states $5s[3/2]_2$ and $5p[5/2]_3$. In case of even isotopes such as $^{82}Kr^*$, $^{84}Kr^*$ and $^{86}Kr^*$, no repumping laser is required for cooling of these isotopes as they do not have hyperfine structures. Typically 10^5-10^6 atoms are trapped in the MOT to a temperature of few hundreds of micro-Kelvin for the experimental parameters used in the setup.

The in-house development of the Kr-MOT setup involves demonstration of several new ideas and methodologies. A new technique for laser frequency stabilization was demonstrated by generating a Doppler-free signal using atomic beam fluorescence (ABF) [7]. This technique was useful to increase the tuning range of the cooling laser and simplification of the setup. In another significant development, the Kr* atom flux transferred to MOT chamber was optimized by applying a moderate external magnetic field (~ 1G) in the path of Kr* atomic beam [8]. In this optimization, the RF power and the pressure in the chambers were found to play an important role. The Kr* atoms generated in the RF discharge tube in the setup were slowed down using the Zeeman slower before being cooled and trapped in the MOT. The Zeeman slower setup significantly improved by using two hollow laser beams for the Zeeman slower beam instead of using a conventional Gaussian laser beam. This resulted in the enhancement of loading of cold atoms in the MOT [9]. The observed enhancement in the number of atoms in the MOT was attributed to reduced destruction of the atomic cloud in the MOT with simultaneous increase in the cooling of the off axis atoms in the atomic beam. The cold atom number in the MOT was estimated by collecting the fluorescence from the MOT cloud on a CCD camera. The temperature of the atomic cloud was estimated using a transient absorption technique where absorption of a probe beam passing through the cloud is measured as the atomic cloud expands after switching off the trap. The number of cold atoms loaded in the MOT was ~10^6 at a temperature of ~ 300 μK. The loading time of the MOT was ~ 250 ms.

Further, two different isotopes of Kr atom (^{84}Kr* and ^{86}Kr*) in the excited state were simultaneously cooled and trapped for the first time in the MOT [10]. The overlapped cold atomic clouds of these different isotopes of Kr atoms were used to study the heteronuclear cold collisions. Two body heteronuclear loss rate coefficient due to collisions between ^{84}Kr* and ^{86}Kr* was estimated to be $\beta_{^{84}Kr^*-^{86}Kr^*}$ = (8.7±0.8)x10^{-10} cm^3/s. The heteronuclear cold collision loss rate was also found to be nearly two times the homonuclear cold collision loss rate.

The studies performed so far using Kr-MOT setup has potential to be extended in the future. The possible future study can include investigations on mixture MOT consisting of fermionic and bosonic atoms [11]. Further effort can be in the direction of increasing the cold atoms number in the MOT by modifying the setup to include an efficient transverse cooling stage, liquid nitrogen cooled discharge stage [12] etc. The incorporation of ion detection system such as micro-channel plate detectors can help further in collision studies [13]. The improvement in the cold atom fluorescence detection can also be helpful for future applications such as atom trap trace analysis (ATTA) [5].

References:

1. Claude Cohen-Tannoudji and David Guery-Odelin, “Advances in Atomic Physics: An Overview”, World Scientific, Hackensack, NJ, (2011).

2. J. Weiner , V. S. Bagnato, S. Zilio and P. S. Julienne, Rev. Mod. Phys. **71** 1 (1999).

3. W. Vassen, C. Cohen-Tannoudji, M. Leduc, D. Boiron, C. I. Westbrook, A. Truscott, K. Baldwin, G. Birkl, P. Cancio, and M. Trippenbach, Rev. Mod. Phys. **84** 175 (2012).

4. C. Y. Chen, Y. M. Li , K Bailey, T. P. O’Connor, L. Young and ZT. Lu, Science **286** 1139 (1999).

5. Xu Du, “Realization of Radio-Krypton Dating With an Atom Trap”, Ph.D. thesis, Northwestern University, Evanston Illinois, (2003).

6. F. Shimizu, K. Shimizu and H. Takuma, Jap. J. Appl. Phys. **26** L1847(1987).

7. S. Singh, V. B. Tiwari, S. R. Mishra and H. S. Rawat, Laser physics **24**, 25501(2014).

8. S. Singh, Vivek Singh, V. B. Tiwari, S. R. Mishra and H. S. Rawat, Indian Journal of Pure and Applied Physics **51**, 230 (2013).

9. S. Singh, V. B. Tiwari, S. R. Mishra and H. S. Rawat, J. Exp. Theo. Phys. **119**, 406 (2014).

10. S. Singh, V. B. Tiwari, Y. B. Kale, S. R. Mishra and H. S. Rawat, J. Phys. B: At. Mol. Opt. Phys. **48**, 175302(2015).

11. R. J. W. Stas, J. M. McNamara, W. Hogervorst and W. Vassen, Phys. Rev. A **73** 032713 (2006).

12. C. -F. Cheng, W. Jiang, G. -M. Yang, Y. -R. Sun, H. Pan, Y. Gao, A. -W. Liu and S. -M. Hu, Rev. Sci. Instrum. **81**, 123106 (2010).

13. C. I. Sukenik and H. C. Busch, Phys. Rev. A **66** 051402(R) (2002).